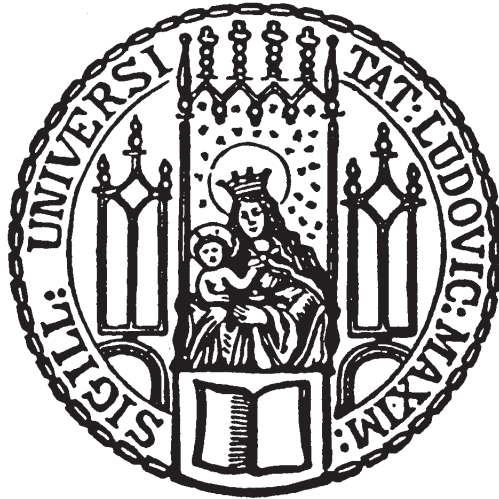


# Contribution from Stellar Binaries to the X-ray Emission of Simulated Galaxies



Master thesis at the Faculty of Physics  
Ludwig-Maximilians-Universität München

Submitted by

**Stephan Vladutescu-Zopp**

Supervised by

PD Dr. Klaus Dolag  
Dr. Veronica Biffi

Munich, 15<sup>th</sup> of April 2021



# Beitrag von Röntgendoppelsternsystemen zur Emission von simulierten Galaxien



Masterarbeit an der Fakultät für Physik  
Ludwig-Maximilians-Universität München

Eingereicht von  
**Stephan Vladutescu-Zopp**

Betreut von  
PD Dr. Klaus Dolag  
Dr. Veronica Biffi

München, den 15.04.2021



# Contents

<b>1</b>	<b>X-ray Binaries: Formation &amp; Evolution</b>	<b>3</b>
1.1	Types & Distinction . . . . .	3
1.2	Lifetime and Occurrence . . . . .	5
1.2.1	Evolution of HMXBs . . . . .	8
1.2.2	Evolution of LMXBs . . . . .	9
1.2.3	Luminosity functions & Scaling relations . . . . .	10
1.3	Spectral Properties . . . . .	13
1.3.1	Accretion processes . . . . .	14
1.3.2	Variability . . . . .	16
<b>2</b>	<b>Numerical Simulations</b>	<b>19</b>
2.1	Context regarding cosmological simulations . . . . .	19
2.2	Magneticum Pathfinder Simulations . . . . .	20
2.3	The photon simulator PHOX . . . . .	24
2.3.1	General code structure . . . . .	24
2.3.2	Emission model for hot gas . . . . .	26
2.3.3	Emission model for AGN . . . . .	26
<b>3</b>	<b>Emission modelling of synthetic XRB populations</b>	<b>31</b>
3.1	MC sampling of empirical model . . . . .	31
3.2	Determining the population size from particle quantities . . . . .	33
3.2.1	Mass proportionality of the LMXB population . . . . .	34
3.2.2	Formation efficiency of HMXBs as a SFR proxy . . . . .	35
3.2.3	Assigning spectral parameters . . . . .	36
<b>4</b>	<b>Analyzing spectra of simulated galaxies</b>	<b>39</b>
4.1	The data . . . . .	39
4.2	Recovering empirical Relations . . . . .	40
4.2.1	Luminosity Functions . . . . .	40
4.2.2	Mass & SFR relation . . . . .	41
4.2.3	Spatial distribution of XRB emission . . . . .	43
4.3	Ratio of XRB, AGN and gas emission . . . . .	44
4.3.1	LXB vs HXB . . . . .	44
4.3.2	Gas vs. XRB . . . . .	45
4.3.3	AGN vs. XRB . . . . .	46
4.4	Average galaxy spectra . . . . .	49

4.4.1	Hubble-type Correlation . . . . .	49
4.4.2	Stellar Mass and Star-formation Binning . . . . .	51
4.5	Estimates of the Cosmic X-ray background . . . . .	53
4.5.1	Background & Source removal . . . . .	56
4.5.2	Redshift dependence of relative XRB contribution . . . . .	57
<b>5</b>	<b>Discussion</b>	<b>61</b>
5.1	Conclusions . . . . .	61
5.2	Future Investigations . . . . .	63
	<b>References</b>	<b>65</b>
	<b>List of Figures</b>	<b>75</b>
	<b>List of Tables</b>	<b>81</b>
	<b>Abbreviations</b>	<b>83</b>
<b>A</b>	<b>Additional Figures</b>	<b>85</b>
<b>B</b>	<b>Acknowledgement</b>	<b>89</b>

# Abstract

In this work we present a new module implemented into the virtual photon simulator PHOX (Biffi, Dolag, Böhringer, et al. (2012)) to construct synthetic X-ray spectra of XRB populations from cosmological simulations. In particular, we used universal scaling relations of XRB luminosity functions (i.e. Mineo et al. (2012a) and Zhang, Gilfanov, and Bogdán (2012)) to estimate the emission of single stellar populations (SSPs) represented by stellar resolution elements in cosmological simulations, and test the validity of the model on the *Magneticum Pathfinder* set of simulations. Taking the evolutionary timescales of massive stars and stellar binary interactions into account, we were able to reliably produce representations of XRB populations with respect to the SFR and stellar mass of the host galaxy as well as the expected spatial correlation of XRB emission with galaxy properties like stellar age distribution and gas surface density. We find that XRBs are on average responsible for up to  $\sim 50\%$  of a local galaxy's X-ray emission in the soft X-ray band ( $0.5 - 2$  keV) and up to 100% in the hard X-ray band ( $2 - 10$  keV) if AGN emission is omitted. Furthermore, we find no significant difference in the averaged SEDs of ETGs and LTGs, due to suppression of SFR and  $M_*$  variations in the average. Missing parts of the galactic halo due to inadequate selection of projection radii in PHOX have not been investigated. The shapes of our average SEDs are consistent with observations of average spectra of star forming galaxies [Lehmer, Basu-Zych, et al. (2016)]. Our estimates of XRB contribution to the galactic X-ray emission are in line with observations [Wik et al. (2014)]. We find non-monotonic behaviour of XRB emission with increasing SFR which is connected to low number statistics in recovered scaling relations of LMXBs and HMXBs and the contribution of massive halos in the data. Additionally, we were able to reproduce measurements of the diffuse cosmic X-ray background (Cappelluti et al. (2017)) using constructed lightcones within Box2 of Magneticum ranging from  $z \sim 0.1$  to  $z \sim 2$ , thereby quantifying the redshift dependence of the relative XRB contribution. We find a decrease in relative XRB contribution in the observational frame with increasing redshift and a overall contribution of less than 3% to the lightcone emission.



# Introduction

The first X-ray surveys of the sky revealed a plethora of unique and interesting phenomena: from young newly formed stars in the cold clouds of our galaxy [Appenzeller and Mundt (1989)] over supernova remnants [Reynolds (2008)] to X-ray halos surrounding distant galaxies [Fabbiano (1989)]. Among the brightest sources of X-ray radiation are galaxy clusters, the largest gravitationally bound objects in the universe, and active galactic nuclei (AGN) powered by accretion onto super-massive black holes (SMBH). Clusters of galaxies form via hierarchical structure formation [White, Briel, et al. (1993)], where the gravitating mass can be inferred from temperature and density measurements of the intra-cluster medium (ICM), assuming hydro-static equilibrium. High plasma temperatures of the gas residing in the large potential wells of galaxy clusters cause the emission of thermal Bremsstrahlung in the X-ray spectrum and prompted the need for an additional dark matter component dominating the total mass of the cluster. This X-ray brightness makes galaxy clusters useful probes for cosmological studies. The difficulty in observing galaxy clusters lies in accurately capturing their outskirts as they are extended sources and show less intense radiation at their margins [see Kravtsov and Borgani (2012) on galaxy cluster formation]. In contrast to galaxy clusters, AGN are highly luminous in almost the whole range of the electromagnetic spectrum and appear as point sources in the X-ray sky. This large bolometric brightness could be explained by the presence of a supermassive black hole (SMBH) actively accreting matter from its surrounding. It is commonly accepted today that every galaxy hosts a SMBH at its center though not all of them are considered AGN [see e.g. Beckmann and Shrader (2012)].

Another type of X-ray point source, typically appearing in the galactic foreground and nearby galaxies, are a certain type of stellar binary systems. We know that more than 50% of sun like main sequence (MS) stars have a companion with a mass ratio  $q = M_2/M_1$  of more than 0.1, with  $M_1$  being the mass of the more massive primary and  $M_2$  being the mass of the lighter companion. In fact, more massive MS primaries are expected to have up to 2.1 companions with  $q > 0.1$  on average [Moe and Di Stefano (2017)]. Recent studies not only focus on the direct gravitational interaction of binaries but also on the hydrodynamical interactions of their environments like circum-binary disks [see D’Orazio and Duffell (2021) and Duffell et al. (2020)]. Systems harbouring massive primaries ( $M_1 > 8M_\odot$ ) are particularly volatile, as the more rapidly evolving massive star eventually leaves behind its core as a black hole (BH) or neutron star (NS) after its explosion as a supernova (SN). Significant mass loss of the primary due to the supernova may disrupt the binary if  $q < 1$  [Lewin and van der Klis (2006) and Lewin, van Paradijs, and van den Heuvel (1995)]. In the cases where a binary survives the SN, the system may develop into an accretion powered, compact X-ray source called X-ray binary (XRB). XRBs are of particular interest since they function as small scale analogues for AGN: they provide insight in accretion processes, changes in accretion geometry during state transitions (hard-state and soft-state analogues to quiescent and quasar regimes in AGN) and the subsequent formation of radio jets [Körding et al. (2006)]. Recent studies on that topic have been made on the recently discovered galactic LMXB *Maxi J1820+070* [see e.g. Zdziarski, Dzielak, et al. (2021) and references therein, and Kawamuro et al. (2018)]

for initial alert]. Moreover, their spectra may also yield insights into the equation of state of degenerate matter in neutron stars [Lewin, van Paradijs, and Taam (1993) and Steiner et al. (2010)]. The nature of the compact object at the center of a X-ray bright point source from mass measurements alone can be challenging, especially in the not well understood dividing boundary regime of  $\sim 2 - 3M_{\odot}$  where the heaviest NSs and lightest stellar BHs reside. Therefore other spectral features like bursts, pulsations and quasi periodic oscillations (QPOs) have been used trying to correlate those behaviours with the nature of the central object [see e.g. Lewin and van der Klis (2006) and Lewin, van Paradijs, and van den Heuvel (1995) for a review]. It was also shown recently, that the Compton  $y$ -parameter - the average change in the energy of a single photon due to multiple Compton scattering events - and amplification factor  $A$  - average energy transfer per single scatter event - may provide clear distinction between NS and BH XRBs in their hard-state from the argument that BHs lack a physical surface [see Banerjee et al. (2020) and references therein]. X-ray binaries are still an active area of research as they provide constraints on mass-loss rates of massive stars [Neijssel et al. (2021)] and they may also have played a significant role in the re-ionization of the universe at  $z \gtrsim 7$  [Madau and Fragos (2017), Lehmer, Basu-Zych, et al. (2016), and Fragos, Lehmer, Naoz, et al. (2013)] as the not yet metal enriched ISM allowed for more XRBs of higher luminosity [see Lehmer, Eufrasio, Basu-Zych, et al. (2021) and Garofali et al. (2020)]. With the launch of high-resolution telescopes such as *Chandra* [see Weisskopf et al. (2000)], *XMM-Newton* and the now operating all sky X-ray survey of *eROSITA* [Predehl et al. (2021)], the detailed study of such compact objects has been (and will be in the case of *eROSITA*) made even more accessible. This allows for detailed studies of the composition and scaling of the X-ray emitting components in nearby galaxies [see e.g. Lehmer, Ferrell, et al. (2020), Zhang, Gilfanov, and Bogdán (2012), Mineo et al. (2012b), and Mineo et al. (2012a)] which we want to follow up with theoretical predictions from cosmological simulations in this work.

The aim of this work will be to study scaling relations and global properties of synthetic XRB emission using data from the *Magneticum Pathfinder* cosmological simulations and give soft predictions on the relative X-ray composition of nearby galaxies. This is achieved by implementing a XRB emission model into the virtual photon simulator *PHOX* [Biffi, Dolag, Böhringer, et al. (2012) and Biffi, Dolag, and Merloni (2018)]. The model statistically samples global luminosity functions of XRBs from nearby galaxies [Grimm et al. (2003), Gilfanov et al. (2004), Zhang, Gilfanov, Voss, et al. (2011), and Mineo et al. (2012a)] and computes corresponding spectra for single stellar particles of the simulation using *XSPEC* [Arnaud (1996)].

# Chapter 1

## X-ray Binaries: Formation & Evolution

In this chapter largely references an excellent summary on X-ray binaries from Lewin, van Paradijs, and van den Heuvel (1995) if not otherwise indicated. It is aimed at giving a brief introduction to the main characteristics defining XRB systems, focused on the properties needed in subsequent chapters. Those properties include XRB types and their evolution as well as spectral properties. In the end we will evaluate the emergence of those properties in the scope of cosmological simulations.

### 1.1 Types & Distinction

The heuristic distinction of XRBs starts with the requirement of an evolved stellar remnant - usually a NS or BH - which is in orbit with either a massive donor star ( $M \gtrsim 8M_{\odot}$ ) which we then call HMXB. Or, if the donor star is rather light ( $M \lesssim M_{\odot}$ ) we call it a LMXB. The mass transfer usually sets in by atmospheric or wind Roche-Lobe overflow (RLO) in the HMXB case, or regular RLO by close interaction in the LMXB case. Note, that the main driving factor in the evolution of these systems are the different timescales the donor is subjected to which are largely determined by the donor's mass. We will go into more detail in section 1.2. A more sophisticated analysis of the intrinsic properties of these systems extends the aforementioned mass cuts with the following:

- The optical counterparts of LMXBs are faint ( $M_v > 0$ ) compared to HMXBs which typically are more than two orders of magnitude brighter, where  $M_v$  is the absolute magnitude in the V-band. Due to interstellar absorption, most LMXBs have no optical counterpart.
- Optical spectra of LMXBs lack normal stellar absorption features, excluding quiescent transient sources (see section 1.3.2) with late-type giant stars.
- The ratio of X-ray to optical luminosities in LMXBs is in the range of  $\sim 10^2 - 10^4$ , while for HMXBs it is significantly lower with a range of  $\sim 10^{-3} - 10^1$ .
- The X-ray spectra of LMXBs are softer than those of HMXBs with  $kT_e \lesssim 10$  keV for LMXBs and  $kT_e > 15$  keV for HMXBs.
- Known LMXBs have significantly shorter orbital periods ( $1 \text{ hr} \lesssim P \lesssim 1 \text{ d}$ ) than HMXBs ( $1 \text{ d} < P \lesssim 500 \text{ d}$ )

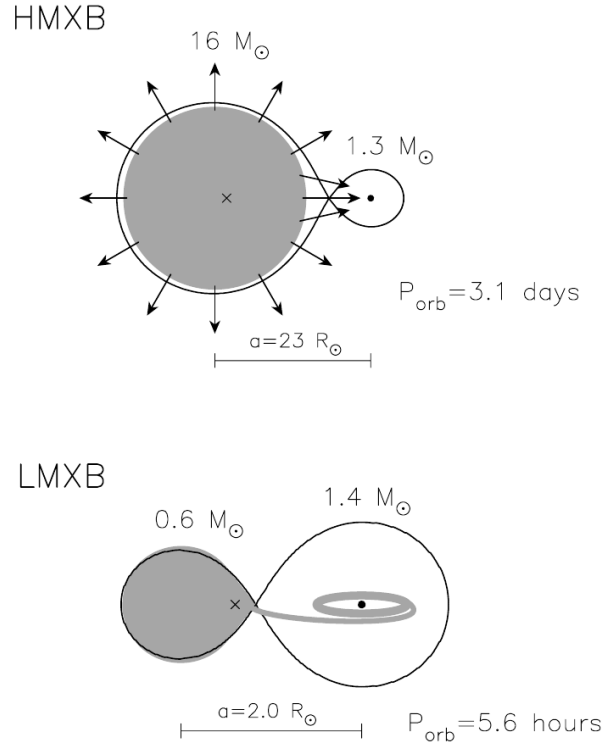


**Figure 1.1:** Schematic illustration of typical HMXB and LMXB orbital configurations. The HMXB case depicts the more spherically symmetric accretion of wind material of the donor. The LMXB case shows the RLO of an evolved MS low mass star. Graphic directly taken from Lewin and van der Klis (2006).

- Only LMXB show X-ray bursts (see section 1.3.2) whereas HMXB do only show regular X-ray pulsations
- Estimated magnetic field strengths are larger in HMXBs ( $B > 10^{12}\text{G}$ ) compared to LMXBs ( $B > 10^9\text{G}$ )

The X-ray luminosity of these systems can reach up to  $L \lesssim 10^{38} \text{ erg s}^{-1}$ , though ultra luminous X-ray sources (ULXs) have been observed, which require super Eddington accretion rates in order to explain luminosities of  $L > 10^{39} \text{ erg s}^{-1}$ . Schematic visualizations of LMXB and HMXB systems can be seen in Figure 1.1 respectively. Other types of compact X-ray sources include cataclysmic variables (CVs), where the accreting object is a white dwarf, and intermediate-mass X-ray binaries (IMXB) with a donor mass of  $2M_{\odot} \lesssim M \lesssim 5M_{\odot}$ . While IMXBs are thought to be more abundant than LMXBs it is by now accepted that most IMXB systems are progenitor systems of LMXBs. Their low observed abundance is caused by two factors. For one, the intermediate mass companion is not massive enough to launch substantial winds in order to power a X-ray source. Second, if the eventual RLO initiates, the large mass ratio between donor and compact object (CO) will keep the accretion phase on sub-thermal timescales or they evolve via a common envelope [Tauris et al. (2000)]. Additionally, the ensuing high mass-transfer rates ( $\dot{M} > 10^4 M_{\odot} \text{ yr}^{-1} \gg \dot{M}_{\text{edd}}$ ) possibly causes produced X-rays to be absorbed by dense gas surrounding the accretor [Lewin and van der Klis (2006)]. Such systems may last only for a few 1000 yr. We will thus limit our description of XRB evolution to HMXBs and LMXBs types. The detailed description of CVs is beyond the scope of this thesis which is why we direct the interested reader to Lewin, van Paradijs, and van den Heuvel (1995) and Lewin and van der Klis (2006) which also include reviews and references regarding physical processes in CVs.

## 1.2 Lifetime and Occurrence

From basic assumptions about the structure evolution of isolated stars, we can gain insight on the possible formation pathways and timescales on which massive binary systems evolve. They are largely determined by the stellar evolution of the massive primary and, more specifically, dependent on the mass of the primary. We start by considering the typical time a star will stay on the main sequence (MS) of the HR-diagram. It is defined by the duration of hydrogen burning in the stellar core. If we assume a core mass to be 10% of the stellar mass  $M_*$ , an energy conversion efficiency of  $\epsilon_{pp}$  and radiated energy in terms of luminosity  $L$ , we get

$$\tau_n \simeq \frac{0.1 M \epsilon_{pp}}{L} \simeq 10^{10} \left( \frac{M}{M_\odot} \right)^{-2.8} \text{ yr}, \quad (1.1)$$

if we assume typical MLRs as in table 1.1, where empirical mass-radius relations (MRR) as well as mass-luminosity relations (MLR) for hydrogen burning main sequence stars in binary systems are displayed. The different slope in the MRR for massive stars is caused by additional radiative pressure in its outer layers. These empirical relations for the MRR are actually reversed from what is expected from stellar structure theory, where more massive stars are expected to show linear relation in MRR (i.e more 'puffy' envelopes) and low mass stars should scale with  $\sim M^{0.5}$ . Baraffe et al. (1998) showed that the standard stellar structure approach is incomplete as detailed atmospheric modelling for low mass stars is required to match observations. The luminosity scaling, however, is well in line with standard derivations of stellar structure.

	$M \gtrsim M_\odot$	$M \lesssim M_\odot$
Mass-radius relation <sup>1</sup>	$R/R_\odot \simeq (M/M_\odot)^{0.75}$	$R/R_\odot \simeq (M/M_\odot)$
Mass-luminosity relation <sup>1</sup>	$L/L_\odot \simeq (M/M_\odot)^{3.8}$	$L/L_\odot \simeq (M/M_\odot)^3$
Mass-radius relation <sup>2</sup>	$R/R_\odot \simeq (M/M_\odot)^{0.59 \pm 0.03}$	$R/R_\odot \simeq (M/M_\odot)^{1.00 \pm 0.05}$
Mass-luminosity relation <sup>2</sup>	$L/L_\odot \simeq (M/M_\odot)^{3.78 \pm 0.04}$	$L/L_\odot \simeq (M/M_\odot)^{3.80 \pm 0.22}$
Mass-radius relation <sup>3</sup>	$R/R_\odot \simeq (M/M_\odot)^{0.56 \pm 0.02}$	$R/R_\odot \simeq (M/M_\odot)^{0.93 \pm 0.05}$
Mass-luminosity relation <sup>3</sup>	$L/L_\odot \simeq (M/M_\odot)^{3.76 \pm 0.04}$	$L/L_\odot \simeq (M/M_\odot)^{3.78 \pm 0.22}$

**Table 1.1:** Empirical mass-radius and mass-luminosity relations from stars in binary systems. <sup>1</sup>: Values adopted from table 11.3 in Lewin, van Paradijs, and van den Heuvel (1995) which uses data from Andersen (1991). No uncertainties given. <sup>2</sup>: Best-fit power law slope derived from data in table 2 of Torres et al. (2010). <sup>3</sup>: Best-fit power law slope derived from data in table 2 of Eker et al. (2015)

After the core of a star exhausts its hydrogen fuel, the thermal equilibrium of the star is disturbed which leads to a readjustment of its state via the Kelvin-Helmholtz or thermal timescale

$$\tau_{th} \simeq \frac{GM^2}{RL} \simeq 3 \times 10^7 \left( \frac{M}{M_\odot} \right)^{-2.4} \text{ yr}, \quad (1.2)$$

with  $M$  the stellar mass and  $R$  the stellar radius for a MRR of  $R \propto M^{0.6}$  and a MLR of  $L \propto M^{3.8}$ . If the hydro-static equilibrium of a star is disturbed, e.g. by sudden mass loss, it will adjust to a new equilibrium on dynamic timescale

$$\tau_d \simeq \frac{R}{c_s} \simeq 0.04 \left( \frac{M_\odot}{M} \right)^{0.5} \left( \frac{R_\odot}{R} \right)^{1.5} \text{ days}, \quad (1.3)$$

where  $R$ ,  $M$  are the radius and mass of the star and  $c_s$  is the average sound speed. Moreover, the response of a mass-losing star is dependant on the entropy and temperature gradient of its envelope (see e.g. Ge et al. (2020)). We distinguish by radiation and convection dominated envelopes.

Assuming a radiative envelope, a mass-losing star will shrink on dynamical timescales, trying to adjust its hydro-static equilibrium. Consequently, the star also has to adjust to a new thermal equilibrium. The mass loss causes the core to envelope mass ratio to increase which is similar to the state of a more evolved star. So, the more massive star is expanding on thermal timescales. Simultaneously, the Roche-Lobe of the more massive star shrinks, making the mass transfer unstable. Combining these processes leads to the conclusion that if mass transfer between stars is started, it will continue on a thermal timescale until the mass ratio  $q$  of the binary is reversed and the Roche-Lobe of the donor increases again. The mass transfer can then stabilize again, if the Roche-Lobe grows faster than the expanding star [Verbunt (2015)]. In practice, the more massive donor would be stripped almost completely of its hydrogen-rich envelope, and is stopped by ignition of helium fusion in its core causing significant shrinking. The conservative assumption is an incomplete description for massive stars, however, as a substantial fraction of mass is lost through stellar wind which will take angular momentum with it. Though, it is applicable to most LMXB systems with a donor mass of  $M \lesssim 1.8M_\odot$  and short orbital periods [Lewin and van der Klis (2006)].

Convective envelopes react to mass-loss with a rapid expansion (e.g. red giant stars) due to a super-adiabatic temperature gradient in its envelope, which leads to unstable mass transfer if the Roche-Lobe does not adjust accordingly. The Roche-Lobe is described by the equipotential surfaces passing through the inner Lagrange point, L1, arising from the effective gravitational potential in a co-rotating frame

$$\Phi = -\frac{GM_1}{r_1} - \frac{GM_2}{r_2} - \frac{\Omega^2 r_3^2}{2}, \quad (1.4)$$

where  $r_1$  and  $r_2$  are the distances to the centers of two stars with mass  $M_1$  and  $M_2$ ,  $r_3$  is the distance to the rotational axis and where we assume circular orbits with

$$\Omega = \sqrt{\frac{G(M_1 + M_2)}{a^3}}. \quad (1.5)$$

See Figure 1.2 for a illustration of the effective potential. If the stellar surface of an expanding star reaches the Roche-Lobe, mass transfer to the companion will start through the inner Lagrange point. This mass transfer is considered to be stable, as long as the Roche-Lobe radius adjusts to the mass loss faster than the star is expanding. Convective envelopes may increase their radius through this mass loss fast enough, such that the stellar radius reaches the outer Lagrange points. This leads to mass being completely lost from the system. Note, that the latter may not be applicable to reality as mass ejected from the stellar surface will stop co-rotating with the system requiring different prescriptions than the effective potential. It may also happen that the expanding star reaches its companion before mass-transfer can stabilize. Together with efficient orbital shrinking, given by the angular momentum balance equation with mass loss in equation (1.7), leads to the companion plunging into the envelope of the expanding star. This phenomenon is then further described by the common envelope (CE) evolution.

As the companion star moves through the envelope of the evolved star, it experiences drag, which causes a decrease in orbital angular momentum. The kinetic energy of the orbit will be transferred to the envelope. This leads to a rapid reduction in orbital separation between the binary components and in most cases, the envelope will be ejected [Lewin and van der Klis (2006)]. A simple estimate for the decrease in orbital separation can be found by equating the binding energy of the envelope to the difference in orbital energy  $E_{env} \equiv \eta_{CE} \Delta E_{orb}$  which

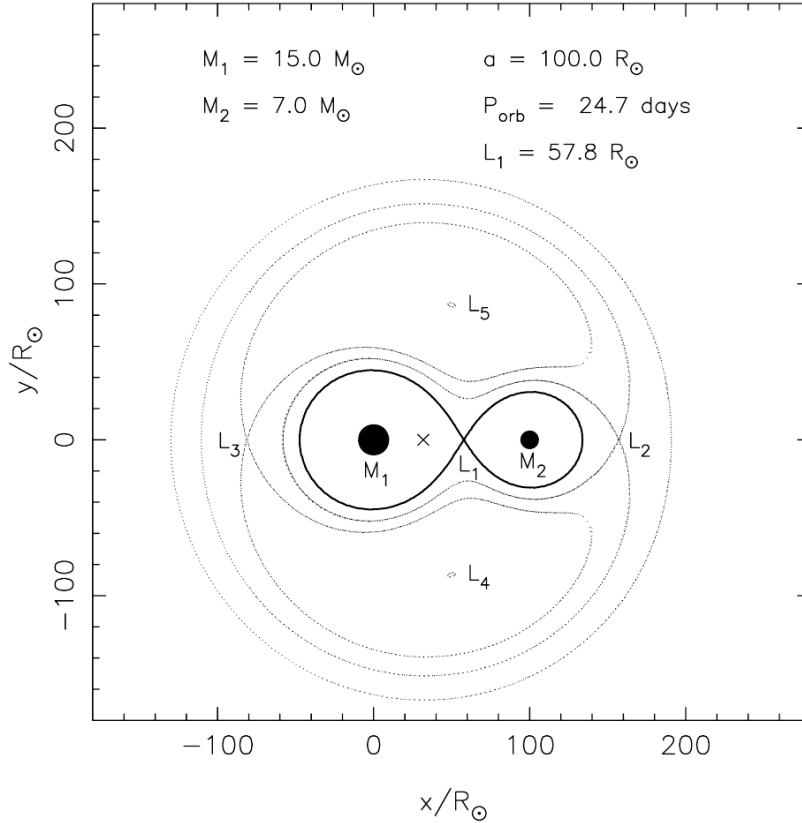


**Figure 1.2:** Cross section of equatorial plane of equipotential surfaces in binaries. The thick curve enclosing the binaries through L1 represents the Roche-Lobe. Graphic directly taken from Lewin and van der Klis (2006).

then yields

$$\frac{GM_{donor}M_{env}}{\lambda a_i r_L} \equiv \eta_{CE} \left[ \frac{GM_{core}M}{2a_f} - \frac{GM_{donor}M}{2a_i} \right], \quad (1.6)$$

where  $a_i, a_f$  are the orbital separations before and after the CE-phase,  $M_{core} = M_{donor} - M_{env}$ ,  $\eta_{CE}$  is the conversion efficiency of orbital energy to kinetic energy,  $r_L = R_L/a_i$  is the dimensionless Roche-Lobe radius of the donor and  $\lambda$  is a parameter depending on the evolutionary state of the star.

While the effects of CE have drastic consequences on short timescales, the orbital separation of the binary can be further influenced by other mechanisms which carry away angular momentum from the system during or before mass transfer phases (the latter in the case for LMXB, where the two companions have to approach at later stages). Generally, we distinguish between conservative and non-conservative mass transfer, where the former assumes an ideal system of total mass conservation and the latter considers mass being lost from the system. Realistically, the conservative case never truly occurs, it is however a reasonable approximation for stable mass transfer via RLO within a binary system. More realistic is the non-conservative case, in which only a fraction  $\beta$  of the mass lost by the donor is transferred to the receiving star. This will result in a change in the orbital separation  $a$  with

$$\frac{\dot{a}}{a} = 2\frac{\dot{J}}{J} - 2\frac{\dot{M}_2}{M_2} \left( 1 - \frac{\beta M_2}{M_1} - \frac{(1-\beta)M_2}{2(M_1 + M_2)} - \alpha(1-\beta)\frac{M_1}{M_1 + M_2} \right), \quad (1.7)$$

where dots denote time derivatives,  $M_1$  is the mass of the donor,  $M_2$  is the mass of the receiver,  $\alpha$  describes the fraction of the mass-loss, carrying away angular momentum from the

system, in units of angular momentum lost by the donor star and  $J$  is the combination of all other mechanisms capable to extract angular momentum. This includes spin-orbit coupling, gravitational wave radiation and magnetic braking. Magnetic braking occurs in magnetic stellar winds, slowing down the rotation of a low mass companion star with magnetic surface (F,G stars, WD). In tidally locked systems this exchange then comes from the orbital angular momentum. If  $\beta = 1$ , we get the conservative case. If we assume that angular momentum change is only due to mass loss  $\dot{J} = 0$  and almost all mass is lost from the system ( $\beta \simeq 0$ ) we would expect the orbit to widen if  $\alpha < 1 + M_2/(2M_1)$ .

### 1.2.1 Evolution of HMXBs

For the exemplary description of a full life cycle of a massive binary system, we will describe each step depicted in Figure 1.3 separately. In doing so, we will also point out some intricacies regarding specific steps, which are not mentioned in the figure. The timestamps provided here were calculated from a MLR with slope 3.5 instead of the value 3.8 as assumed in this thesis. This leads to significant differences in  $\tau_n$ , where the step after the first SN and the HMXB step only lasts  $\sim 3$  Myr instead of 9 and thus presents a major contribution of uncertainty. The description here for HMXBs and the equivalent section 1.2.2 for LMXBs is based on Lewin, van Paradijs, and van den Heuvel (1995), Lewin and van der Klis (2006), and Postnov and Yungelson (2014).

We start with a pair of massive main sequence stars with masses of  $14.4M_\odot$  and  $8M_\odot$  respectively. From equation (1.1) we know that the more massive star will develop first. Through expansion at the end of hydrogen burning, it starts filling its Roche-Lobe. Due to the high mass ratio, the mass transfer will be unstable and happens on thermal timescales  $\tau_t$  which in our case is of the order  $\sim 10^4$  yr for a  $14M_\odot$  star. It will continue transferring mass onto its companion until the mass ratio has inverted and the now helium burning core is exposed. It is assumed that the He-core will continue its evolution as it would have without losing its envelope and explode in a SN leaving behind a NS. From that, the system receives kick velocities and orbital eccentricities which may result in the disruption of the binary. However, this scenario is debated, since, dependent on the core's spin and mass, it may not evolve into a SN at all, but just cool down into a heavy WD after RLO. The orbit widens due to angular momentum transfer from the orbital motion into the spin of the now more massive companion. Some angular momentum is lost in the form of mass being ejected from the system. If the binary survives the He-star's SN, its further development is determined by  $\tau_n$  of the companion. During this time, the system may be seen as a transient HMXB, where the NS starts accreting material from the stellar wind of its companion during its orbital perigee. When the massive companion reaches the end of hydrogen burning, the extreme mass ratio, shrinking of the Roche-lobe due to mass loss of the massive star and shrinking of the orbital separation, lead to a runaway process where the NS plunges into the rapidly evolving envelope of the massive star creating a CE.

The three last steps describe the emergence of a NS binary which is not important for the scope of this thesis. Note, that for extremely massive O-stars, the wind velocities may be too fast to allow significant mass capture via the CO. The ensuing more spherical accretion may result in dense clouds around the CO occluding possible X-ray emission. Of course, this description is only exemplary and heavily depends on the actual orbital configuration, mass losses and inner structure of the stellar components. This leaves room for more exotic candidates like *Cygnus X1* which harbours a massive star of  $\sim 41M_\odot$  together with a  $\sim 21M_\odot$  BH with an orbital period of  $\sim 5.6$  days. See Neijssel et al. (2021) for a recent study revising the binary masses and mass loss rates and providing a possible formation channel.

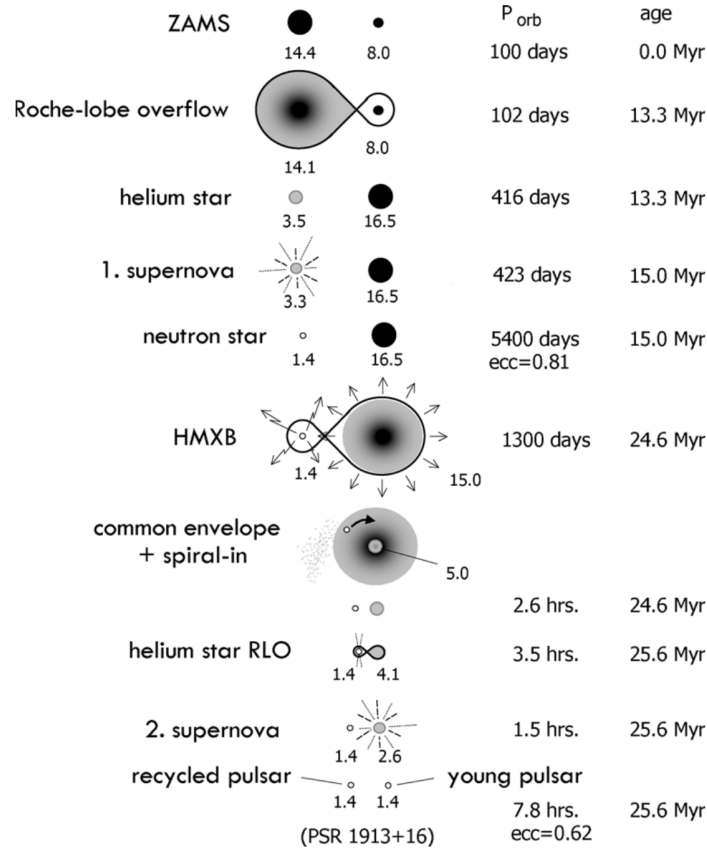


**Figure 1.3:** Evolutionary steps of a typical Be binary system developing into a HMXB source. Individual steps will be outlined in the text. Note, that the timestamps presented here are assumed from a MLR of  $L \propto M^{3.5}$ . Graphic directly taken from Lewin and van der Klis (2006).

### 1.2.2 Evolution of LMXBs

Similar to Section 1.2.1 we will use Figure 1.4 to describe the typical life cycle of an eventual LMXB. The provided time stamps again refer to a MLR with slope 3.5.

We start with a massive binary with extreme mass ratio in order to produce the compact object for a LMXB. Because almost all known LMXBs have extremely low orbital periods, the binary needs a way to quickly lose angular momentum. Common envelope evolution provides a solution, but requires wide initial orbits ( $\simeq 200R_{\odot}$ ) in order to prevent merging of the two stellar cores. The evolving massive star loses mass through stellar winds which further increases the orbital separation of the binary. After nuclear time  $\tau_n$ , the massive companion starts filling its Roche-Lobe and quickly overshooting it, reaching the low-mass star in the process. This results in a CE with spiral in of the companion which completely evaporates the envelope, leaving a close binary pair of a massive helium star and the unscathed low-mass companion. The helium star further evolves into a SN, where the kick velocities of an asymmetric SN and the mass loss from the SN being of the order of the system will most likely dissolve the binary. This is why the SN needs to happen either at a specific point in orbit or gains a favorable kick in the 'right' direction such that the NS stays in orbit. A LMXB then develops either by the companion filling its Roche-Lobe after nuclear time  $\tau_n$ , or, in the cases of even less massive stars, by it further losing angular momentum. The final step depicts the formation of a millisecond pulsar, as the accreted material spun up the NS considerably. With the ignition of pulsar radiation, its companion will be evaporated by intense winds caused by irradiation of the accretion disk (AD) from the pulsar which

may explain the relatively low abundance of low luminosity LMXBs. Zhang, Gilfanov, and Bogdán (2013-2011) show that globular cluster (GC) seeding is a significant contributor to the LMXB population, emphasizing the importance of tidal captures and three-body interactions in dense stellar neighbourhoods as an additional formation channel to LMXB.

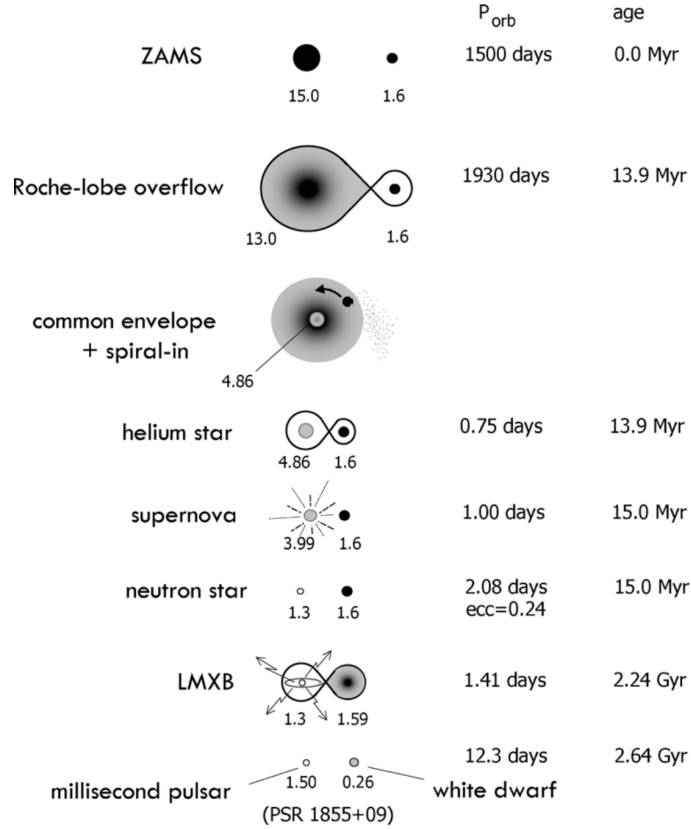


**Figure 1.4:** Evolutionary steps of a typical low mass binary system developing into a LMXB source. Note, that the timestamps presented here are assumed from a MLR of  $L \propto M^{3.5}$ . Individual steps will be outlined in the text. Graphic directly taken from Lewin and van der Klis (2006).

### 1.2.3 Luminosity functions & Scaling relations

Having now knowledge about the basic formation channels of XRBs, we will investigate the population size of each type of binary w.r.t. properties of their host galaxies. If not indicated otherwise, we will be referencing the review of Fabbiano (2006).

From timescale considerations alone, we can infer that HMXBs trace the galactic regions of recent star formation. Since HMXBs require massive stellar components to still be relatively unevolved their time shift w.r.t. the star-formation event that created those massive components can not exceed the nuclear burning time  $\tau_n$ . Which means that HMXBs can not be older than a few Myr. Indeed, Mineo et al. (2012a) and Grimm et al. (2003) find a linear relation between SFR and number of HMXBs in their host galaxy. They propose a distribution in the differential number of HMXBs above a certain X-ray luminosity in the 0.5 – 8 keV band whose normalization scales with SFR linearly. It is given by a single power-law with slope  $\gamma$  and a cut-off luminosity at  $L_{c,H}$

$$\frac{dN_{\text{HXB}}(> L_X)}{dL_{38}} = \begin{cases} A L_{38}^{-\gamma}, & L_{38} \leq L_{c,H} \\ 0, & L_{38} > L_{c,H} \end{cases}, \quad (1.8)$$

where  $A = \xi \times \text{SFR}$  is the normalization of the HMXB XLF based on star formation. Some SFR normalized XLFs of late-type galaxies together with the model XLF for HMXB can be seen in figure 1.5a. The linear relation between SFR and XLF normalization  $\xi$  can be seen in figure 1.5b.

The long evolutionary timescale of LMXBs prevents any connection to the star-formation

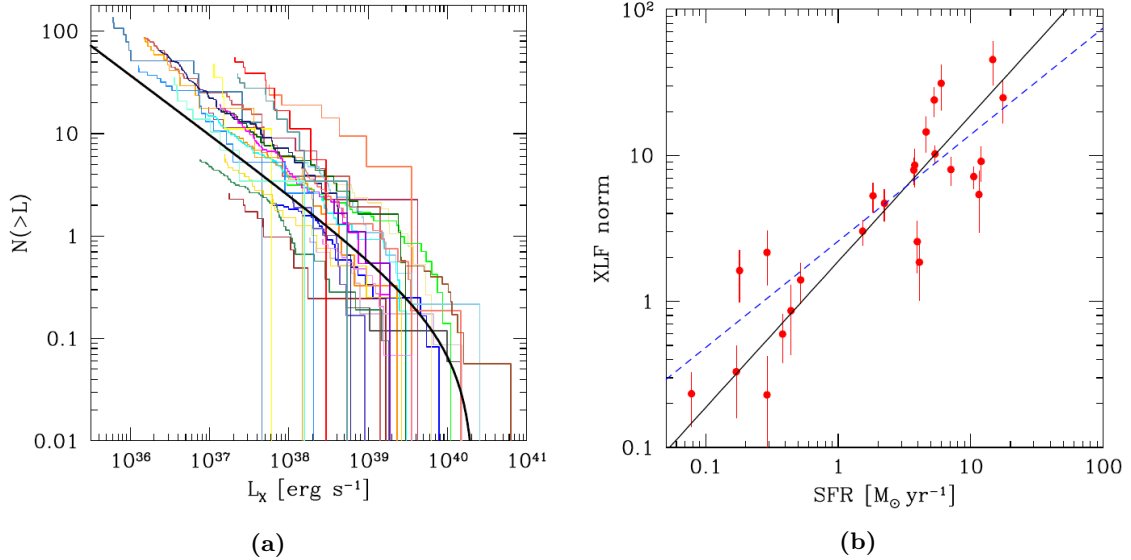


**Figure 1.5:** Graphics directly taken from Mineo et al. (2012a). **(a):** Observed XLFs of HMXB in nearby spiral galaxies normalized w.r.t. SFR in different colors. In black, the cumulative version of the XLF model from equation (1.8) is shown. The y-axis gives the number of HMXBs which have a luminosity  $L$  above  $L_X$ . **(b):** Shown here is the XLF normalization  $A$  for HMXBs w.r.t. the SFR in a given galaxy. Red dots are different galaxies with error bars, the solid line is the best fit linear relation, the dashed line is the best fit relation of the form  $A = \xi \times \text{SFR}^\beta$ , where  $\beta = 0.73 \pm 0.05$ . We assume a linear relation for the XLF normalization in this thesis.

event of the massive progenitor of the CO. We would expect, however, that the number of LMXB increases with time due to the comparatively long X-ray phase of these systems together with more low mass stars evolving with  $\tau_n \gtrsim 1$  Gyr and tidal interaction probability increasing with time in GCs. Note, that a GC may eventually dissipate through gravitational interactions seeding LMXBs to the galactic field [Lehmer, Ferrell, et al. (2020) and Zhang, Gilfanov, Voss, et al. (2011)]. Indeed, Zhang, Gilfanov, and Bogdán (2012) find that the specific normalization of LMXB XLFs increases with time (see figure 1.6a), though the uncertainty regarding the relation is large. They also report that for older galaxies the XLF is steeper than for young galaxies in line with findings by Kim and Fabbiano (2010). Moreover, Gilfanov (2004) see a linear relation between total stellar mass and number of LMXBs in the host galaxy (see figure 1.6b). Note, that in the LMXB studies referenced here, only elliptical galaxies have been used as data. The differential number of LMXB can be described by a double broken power-law

$$\frac{dN_{\text{LXB}}(> L_X)}{dL_{36}} = \begin{cases} K_1(L_{36}/L_{b,1})^{-\alpha_1}, & L_{36} \leq L_{b,1} \\ K_2(L_{36}/L_{b,2})^{-\alpha_2}, & L_{b,1} < L_{36} \leq L_{b,2} \\ K_3(L_{36}/L_{c,L})^{-\alpha_3}, & L_{b,2} < L_{36} \leq L_{c,L} \\ 0, & L_{36} > L_{c,L} \end{cases}, \quad (1.9)$$

where  $K_1$  is the normalization constant in units of  $10^{11} M_\odot$ .  $L_{b,1}$ ,  $L_{b,2}$  are break luminosities and  $L_{c,L}$  is the cut-off luminosity. The exponents  $\alpha$  are the respective power-law

slope in the given interval. The other normalization constants can be derived from  $K_1$  by requiring monotonic continuity at the power-law breaks, s.t.  $K_2 = K_1 (L_{b,1}/L_{b,2})^{\alpha_1}$  and  $K_3 = K_2 (L_{b,2}/L_{c,L})^{\alpha_2}$ . The luminosity subscript 36 or 38 refers to the arbitrarily chosen normalisation of the luminosities  $L_{36} = L/10^{36} \text{ erg s}^{-1}$  and  $L_{38} = L/10^{38} \text{ erg s}^{-1}$ , respectively. X-ray emission from XRBs in galaxies is then dominated by the high-luminosity end of the XLFs Mineo et al. (2012a). The parameter values of the XLFs can be found in table 1.2.

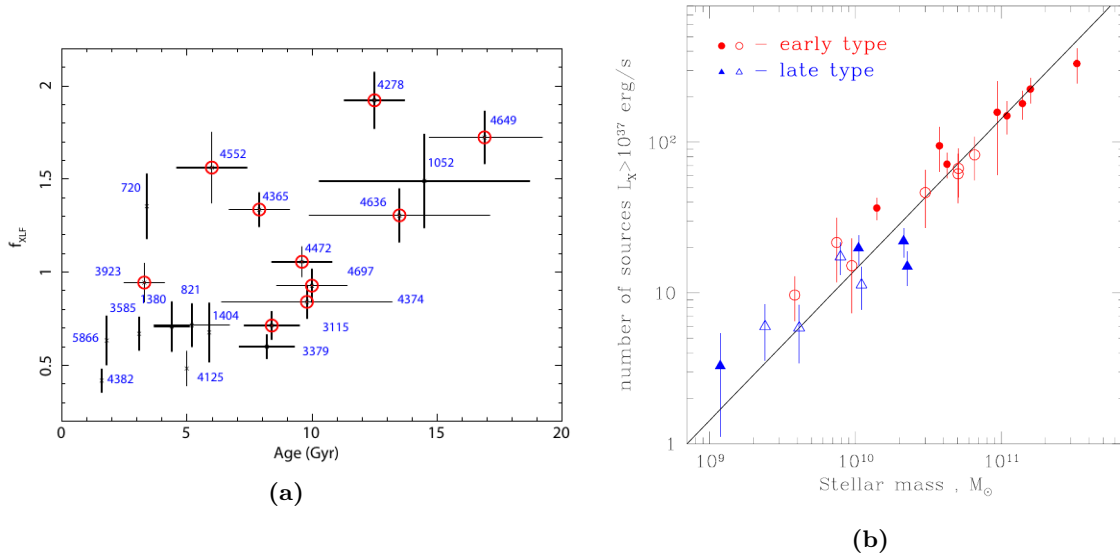


**Figure 1.6:** Graphic (a) directly taken from Zhang, Gilfanov, and Bogdán (2012) and (b) from Gilfanov (2004). (a): Correlation between LMXB XLF normalization  $f_{XLF}$  and age of the elliptical host galaxy. Stellar ages were determined from previous works. Numbers refer to the name of the galaxy in question. Red circles indicate galaxies with globular cluster specific frequency  $S_N > 2.0$ . (b): Shows relation between number of LMXBs and stellar mass of a host galaxy. Red circles are elliptical, blue triangles are spiral galaxies. Empty symbols indicate galaxies observed with smaller annuli.

The extension of the XLFs into regimes of  $L_X > 10^{39} \text{ erg s}^{-1}$  is by now the most likely origin of a class of objects called ultra-luminous X-ray sources (ULX). While some ULXs are suspected to be background AGN based on their bolometric luminosity and some few may be accreting IMBHs, a lot of sources show pulsations which are expected from NS LMXBs [see also Fabbiano (2006) and Swartz et al. (2004)]. Previously, ULXs were thought of COs accreting matter at super-Eddington rates (see section 1.3). Assuming geometrical beaming and non-conservative mass transfer, Misra et al. (2020) find that luminosities of up to  $L_X = 10^{41} \text{ erg s}^{-1}$  can be achieved in IMXB/LMXB systems containing a NS companion if mass transfer happens at super-Eddington rates. Locally, the mass transfer is still Eddington-limited in the accretion disc (unstable). Furthermore, Lehmer, Eufrazio, Basu-Zych, et al. (2021) show that the high-luminosity end of HMXB XLFs is enhanced by a low metallicity environment in the host galaxy further supporting a XRB origin for ULXs. For a recent study on ULX sources and their scaling relations, see Kowlakas et al. (2020). We will use equations (1.8) and (1.9) throughout the remainder of the thesis when referring to XLFs.

$\xi$	$L_{c,H}$	$\gamma$	$K_1$	$L_{b,1}$	$L_{b,2}$	$L_{c,L}$	$\alpha_1$	$\alpha_2$	$\alpha_3$
1.88	$10^5$	$1.59 \pm 0.25$	$1.01 \pm 0.28$	$54.6^{+4.3}_{-3.7}$	$599^{+95}_{-67}$	$5 \times 10^4$	$1.02^{+0.07}_{-0.08}$	$2.06^{+0.06}_{-0.07}$	$3.63^{+0.67}_{-0.49}$

**Table 1.2:** Parameter values for XLFs of equations (1.8) and (1.9) given by the work of Mineo et al. (2012a) for HMXBs (*right*) and Zhang, Gilfanov, and Bogdán (2012) for LMXBs (*left*). The uncertainty of  $\xi$  is given as 0.28 dex. Luminosities are given in units of  $10^{36}$  erg s $^{-1}$ .  $K_1$  has the unit  $10^{-11} M_{\odot}^{-1}$ .  $\gamma$  and  $\alpha$  are dimensionless power-law slopes of the respective XLFs.

### 1.3 Spectral Properties

In this section we will describe governing physical processes which build up the spectrum of X-ray binaries. Vast studies about almost every observed aspect of XRB emission have been performed, of which we will only scratch the surface here. Where appropriate, we will give some interesting follow up reads, and focus only on the fundamental building blocks. In figure 1.7 we present a typical X-ray spectrum of XRBs at the example of the HMXB *Cyg X1*. The different coloured curves are observations at different times and different missions between 1991 and 1998 [see Zdziarski, Poutanen, et al. (2002)]. The solid curves are best-fit Comptonization models. Similar to AGN, the temperatures of the Comptonizing agent in XRBs has  $k_B T \approx 100$  keV. From figure 1.7 it is also apparent that the Comptonization models are well represented by single sloped power-laws for certain photon energies which can be directly related to accretion disk theory. The example SED is complemented by providing a geometrical view of the standard picture of XRB accretion dynamics in figure 1.8 where the observationally derived geometrical structure of the accretion region, i.e the relative position of the Comptonizing regions with respect to the central CO, of the BH LMXB *Maxi J1820+070* are depicted [Zdziarski, Dzielak, et al. (2021)].

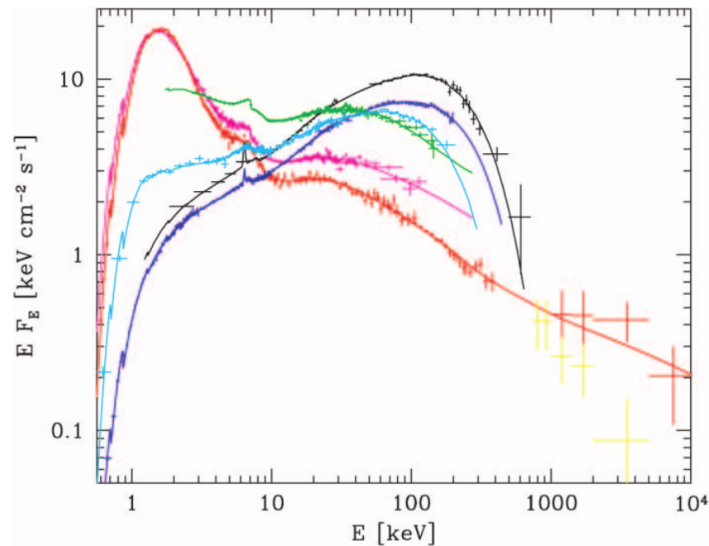


**Figure 1.7:** Broadband spectrum of *Cyg X1* for different pointed observations. Hard-state: *Ginga*/OSSE June 6 1991 (*black*); *BeppoSAX* May 3-4 1998 (*blue*) and Sep 12 1996 (*cyan*). Soft and intermediate states: *BeppoSAX* June 22 1996 together with *CGRO*/OSSE and COMPTEL June 14-22 1996 (*red*); *ASCA*/*RXTE* May 30-21 1996 (*magenta*); *RTXE* May 23 1996 (*green*). Solid curves are best-fit Comptonization models. *Yellow*: Average hard state at 0.75-5 MeV from *CGRO*/COMPTEL. Graphic directly taken from Zdziarski, Poutanen, et al. (2002).

### 1.3.1 Accretion processes

If not otherwise noted, we will reference Lewin and van der Klis (2006). For a more thorough description of accretion processes in astrophysics, see Done et al. (2007), Frank et al. (2002), and White, Stella, et al. (1988). For other XRB spectra see e.g. Tanaka (1997). If matter is accreted by a mass  $M$ , a ring will form, if its specific angular momentum  $J$  is large, such that matter will not impact directly with the accretor. In practice, this means that a mass transfer stream through the inner Lagrange point of a binary will collide with itself after a orbiting the accretor once. The specific angular momentum is then comparable to that of the binary orbital momentum. Energy and angular momentum losses are due to viscosity. Balbus and Hawley (1991) proposed a natural cause for disc viscosity in the form of magneto-rotational instability (MRI), where a disc permeating, weak magnetic field is wound up by orbital shear and transports angular momentum outwards. This leads to dissipation and the initial ring spreads into a disc. This accretion disc is also subjected to self gravity which leads to a hydro-static equilibrium in the vertical disc structure. The vertical structure is then dependant on irradiation, temperature gradient and magnetic field strength for instance and usually settles as a so called thin disk, where the scale height  $H$  of the disc is much smaller than its radial extension  $R$

$$H \simeq \frac{c_s}{v_k} R \ll R. \quad (1.10)$$

The Kepler velocity  $v_k$  is found by multiplying equation (1.5) with  $R$  and  $c_s$  is the local sound speed. We can approximate viscous effects in the accretion disc with the Shakura and Sunyaev (1973)  $\alpha$ -viscosity prescription with an dimensionless number  $\alpha$

$$\nu = \alpha c_s H, \quad (1.11)$$

and assuming a steady state accretion disc

$$\nu \Sigma = \frac{\dot{M}}{3\pi} \left[ 1 - \beta \left( \frac{R_{\text{in}}}{R} \right)^{\frac{1}{2}} \right], \quad (1.12)$$

we get the radial disc temperature profile as

$$T(R) = \left\{ \frac{3GM\dot{M}}{8\pi R^3 \sigma} \left[ 1 - \beta \left( \frac{R_{\text{in}}}{R} \right)^{\frac{1}{2}} \right] \right\}^{\frac{1}{4}}, \quad (1.13)$$

where  $G$  is Newton's constant,  $\dot{M}$  is the intrinsic mass transport of the disc due to viscous dissipation,  $\sigma$  is the Stefan-Boltzmann constant and  $R_{\text{in}}$  is the inner disc edge. Note, that the assumption of black-body radiation is implied in equation (1.13). Accounting for the two-sided geometry of the disc, radial integration yields the total radiated power as

$$L = \left( \frac{3}{2} - \beta \right) \frac{GM\dot{M}}{R_{\text{in}}}, \quad (1.14)$$

where loss of gravitational binding energy contributes  $GM\dot{M}/2R_{\text{in}}$  and the remaining  $(1 - \beta)GM\dot{M}/2R_{\text{in}}$  are provided from the rotational energy of the accretor. We emphasize that the thin disc approximation requires efficient cooling. In the case a low accretion and consequently low gas density, the cooling times are long. In the case of a large accretion rate, radiation may get trapped in the optically thick accretion flow and deposited onto the accretor. For these cases, the thin disc approximation does not hold and advection-dominated accretion flows (ADAFs) need to be employed [e.g. see Done et al. (2007) and Abramowicz et al. (1995)]. The standard picture for XRB accretion disks are, in fact, truncated accretion

disc models, where the cold thin accretion disc breaks down into a diffuse and hot inner accretion flow which is briefly touched on in section 1.3.2. The disc transitions with corresponding spectral changes can be seen in figure 1.9. In either case, the tremendous energy released by the accretion disk produces regions of hot coronal plasma with  $k_B T \approx 100$  keV of Maxwellian distributed non-relativistic electrons above and below the disk. Soft seed photons emitted by the AD with energy  $E < 4k_B T$  will be Compton-scattered to higher harder energies, with each scattering event providing an increase in energy equivalent to the Compton amplification factor  $A$

$$A = \frac{4k_B T - E}{m_e c^2}, \quad (1.15)$$

which is the energy transfer per scattering event, with  $k_B$  the Boltzmann constant,  $T$  the coronal plasma temperature,  $E$  the photon energy and  $m_e c^2 = 511$  keV is the rest mass of the electron. The total energy The number of scattering events  $N$  is determined by the opacity  $\tau$  which for an optically thin medium is  $\propto \tau$  and for an optically thick medium is  $\propto \tau^2$ . The total energy difference of a photon undergoing  $N$  scattering events is measured by the Compton  $y$ -parameter

$$y = A \times N = \frac{4k_B T}{m_e c^2} \max(\tau, \tau^2), \quad (1.16)$$

with variables as defined in equation (1.15). Ultimately, scattering of the soft seed photons leads to a power-law distribution in photon energies. The slope of the power-law, represented by the photon index  $\Gamma$ , can be estimated using a solution to the Kompaneets equation presented in Wilkins and Gallo (2015) and Zdziarski, Johnson, et al. (1996)

$$\Gamma = \sqrt{\frac{9}{4} + \frac{3 m_e c^2}{k_B T \left[ \left( \tau + \frac{3}{2} \right)^2 - \frac{9}{4} \right]}} - \frac{1}{2}, \quad (1.17)$$

where variables are the same as in equation (1.15) and (1.16). Note, that figure 1.7 and 1.9 report their fluxes without normalizing to the bin width which yields for the power-law slope the spectral index  $\alpha = \Gamma - 1$ . This results in a positive slope for the reported hard states when additionally multiplying by the central bin energy for  $E \times F_E$  with  $F_E$  as the flux per energy bin. We emphasize that the estimate for the photon index  $\Gamma$  were initially derived for AGN emission, so they are specifically suited for BH XRB only. If the system consists of a NS binary instead, its physical surface may provide an additional source of soft seed photons for the comptonization process coming from decelerating the accretion flow to match the rotational velocity of the neutron stars surface. This may result in differences in  $A, y$  and  $\Gamma$  with respect to BH systems lacking a physical surface [see e.g. Banerjee et al. (2020) and references therein]. Note, that the energy increase of the photons causes cooling of the coronal plasma, fueling the creation of cold clumps.

In cases where material is accreted spherically from a surrounding medium, like it is in the case for AGN with ISM accretion and HMXBs with wind accretion, we can approximate using the Bondi-Hoyle-Lyttleton prescription for the accretion rate onto the accretor [Bondi (1952), Bondi and Hoyle (1944), and Hoyle and Lyttleton (1939)] with

$$\dot{M}_{\text{acc}} = \frac{4\pi G^2 M_{\text{acc}}^2 \rho(a)}{(c_s^2 + v^2)^{3/2}}, \quad (1.18)$$

where  $M_{\text{acc}}$  is the accretor mass,  $\rho$  and  $c_s$  are the density and sound speed of the surrounding medium and  $v$  is the relative velocity of the accretor w.r.t. to the medium [see e.g. Teklu 2018, chapter 1]. Focusing on the stellar wind spherical accretion in the HMXB case, we consider

that stellar wind velocities  $v_{\text{wind}}$  of massive stars are of the order of  $\gtrsim 1000 \text{ km s}^{-1}$  [Kudritzki and Puls (2000) and references therein], which is large compared to typical orbital velocities  $v_K = \sqrt{G(M_{\text{acc}} + M_{\text{donor}})/a}$  and isothermal sound speed  $c_s = \sqrt{k_B T / \mu m}$  of the order of  $\sim 50 \text{ km s}^{-1}$ . Using mass conservation, we can get the wind density at orbital separation  $a$

$$\rho(a) = \frac{\dot{M}_{\text{wind}}}{4\pi a^2 v_{\text{wind}}}, \quad (1.19)$$

where  $\dot{M}_{\text{wind}}$  is the wind mass loss from the donor. Replacing  $a$  with  $v_K$  and plugging equation (1.19) into (1.18) we get an estimate of mass accreted from the stellar wind by the accretor

$$\frac{\dot{M}_{\text{acc}}}{\dot{M}_{\text{wind}}} = \left( \frac{v_K}{v_{\text{wind}}} \right)^4 \left( \frac{M_{\text{acc}}}{M_{\text{acc}} + M_{\text{donor}}} \right)^2 \ll 1. \quad (1.20)$$

Note, that in the inner accretion flow of spherical accretion, a disc might still be forming albeit it not being thin and the dense surrounding medium might be occluding the X-ray emitting region through heavy absorption.

Furthermore, all accretion processes are limited by Eddington rate which is the balance of inward direct gravitational force and outward directed radiation pressure. It can be expressed as

$$L_{\text{edd}} = \frac{4\pi GMc}{\kappa}, \quad (1.21)$$

$$\dot{M}_{\text{edd}} = \frac{4\pi cR}{\kappa}, \quad (1.22)$$

where  $M$  and  $R$  are the mass and radius of the accreting object,  $c$  is the speed of light and  $\kappa$  is a measure for opacity (e.g. Thomson scattering).

### 1.3.2 Variability

In this section we will briefly glance over some mechanisms responsible for variability in XRB emission on short timescales. The exact reasoning for not going into more detail is then presented in section 2.1. So called X-ray bursts only occur in NS XRBs. They are thermonuclear explosions of material deposited on the surface of the NS. They last for some seconds to minutes. Many XRBs switch between high and low luminosity states in a span of years, months and even days. Such transients can be either caused by orbital features, for example in the case of HMXBs with wide eccentric orbits only accreting sufficient amounts of stellar wind material in their perigee or by periodic occlusion of the X-ray emitting region through the companion. HMXBs may also experience pulsations due to wind instabilities of Be/Oe stars when they are fast rotators, i.e. Wolf-Rayet stars. Alternatively, transients also occur when properties of the the accretion flow change. An important aspect in this, is the change in disc viscosity due to the ionized hydrogen fraction and opacity in the accretion disc as well as transitions between the high soft state, with soft X-ray photons dominating the spectra, and low hard states, with hard X-ray photons dominating. Usually the hard state is accompanied by radio emission from a jet. In order to achieve this transition behaviour, a two component accretion flow is needed where a thin disc is embedded inside a hot inner accretion flow. The mass transfer rate then fuels perturbation growth leading to break downs of the thin disc in the inner flow which is shown in figure 1.9 [see Done et al. (2007)].

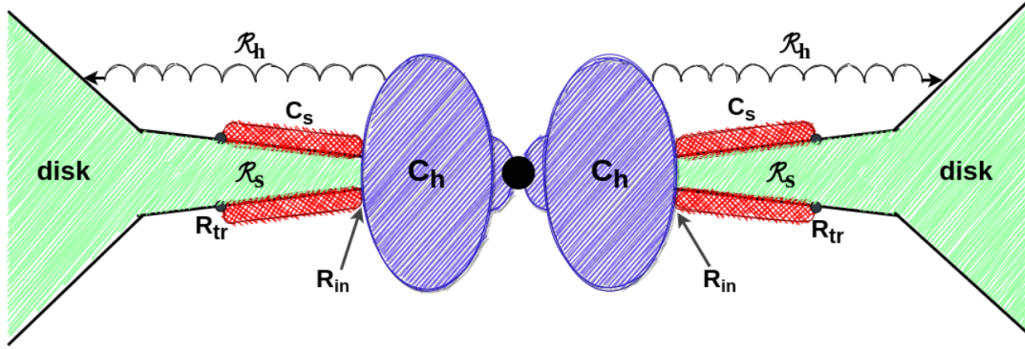


**Figure 1.8:** Accretion geometry around *Maxi J1820+070* derived from X-ray observations. The disk is truncated at  $R_{\text{in}}$ , and covered by a Comptonizing coronal plasma,  $C_s$ , from  $R_{\text{in}}$  to  $R_{\text{tr}}$ . Interior to  $R_{\text{in}}$ , there is a hot accretion flow with a relatively large scale height,  $C_h$ . Comptonization in  $C_s$  and  $C_h$  gives rise to the observed softer and harder, respectively, incident spectral components. The emission of  $C_h$  is reflected from the flared disk beyond  $R_{\text{tr}}$ , marked as  $R_h$ . The emission of the coronal plasma,  $C_s$ , is reflected from the disk beneath it, marked as  $R_s$ . Graphic and description directly taken from Zdziarski, Dzielak, et al. (2021).

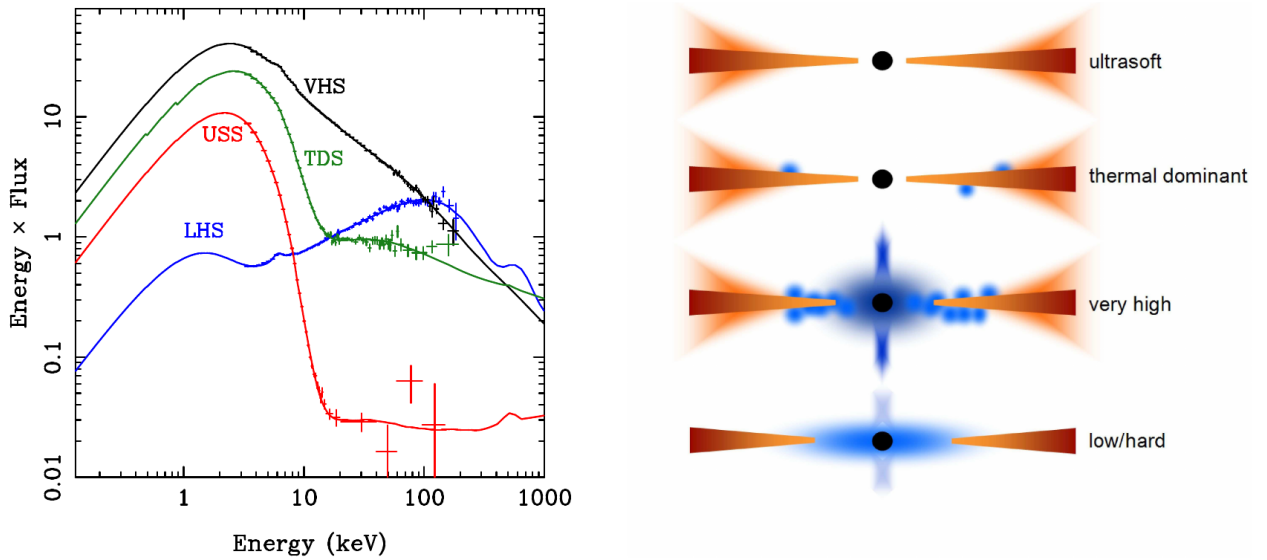


**Figure 1.9:** Transitions of the accretion flow in XRB systems causing different spectral states. The ultra-soft state coincides with a stable thin disk configuration. The thermally dominant state shows the black body spectrum of the increasing temperature of the AD caused by high mass accretion. The very high state shows signs in both soft and very hard X-rays and is associated with the state shortly before the breakdown of the inner accretion flow leading to large comptonizing regions. When the inner accretion flow breaks down we reach the low/hard state dominated by hard X-ray emission from the diffuse comptonizing region in the central flow. The hard state is usually accompanied by radio emission from a developing jet outflow.



## Chapter 2

# Numerical Simulations

Aim of this thesis is to include a model for X-ray emission from X-ray binaries into the virtual photon observatory PHOX. PHOX was developed by Biffi, Dolag, Böhringer, et al. (2012) as a post processing tool for modelling X-ray emission from numerical input of cosmological simulations. We therefore provide a quick introduction to the cosmological simulation used throughout the thesis and which PHOX was tailored to process, namely the *Magneticum Pathfinder* simulations.

### 2.1 Context regarding cosmological simulations

At their core, numerical simulations in astrophysics solve a set of differential equations related to the description of gravitational interaction in or between massive objects. They represent time-resolvable toy models of otherwise inaccessible astrophysical processes, like stellar evolution, planet formation and structure formation, and help in understanding the fundamental physics connected to them. Their goal is to be able to reliably reproduce observational results and with that make predictions of the past and future development of an astrophysical system. Often additional physics beside gravity, e.g. heat transfer and cooling through radiative processes, magnetic fields or hydrodynamics, need to be simulated, in order to match observations. The general aim of large scale cosmological simulations is to study structure formation, i.e. the hierarchical assembly of galaxies and galaxy clusters, in an idealized physical environment. Such simulations mainly follow the non-linear gravitational collapse of a dark and a baryonic matter component, i.e. gas and/or stars, from initial conditions derived from the cosmic matter power spectrum. While shooting for an accurate representations within the simulation framework, hardware limitations require a compromise between the scale of the simulated region and the particle number needed to get converging quantities [for this paragraph, see e.g. Dolag, Borgani, Schindler, et al. (2008)].

As an effect, stars can not be resolved individually but represent an entire population of stars distributed according to an assumed IMF which makes direct tracking of binary evolution, in the context of X-ray binaries and accretion dynamics, impossible. Numerical simulations in general also impose limitations in temporal resolution. A simple approach to time stepping for solving gravitational particle interaction in N-body codes would be to account for the magnitude of their acceleration vector

$$\Delta t = \alpha \sqrt{\epsilon/|\mathbf{a}|}, \quad (2.1)$$

with  $|\mathbf{a}|$  being the gravitationally induced acceleration from the previous time step,  $\epsilon$  being a length scale typically connected to softening and  $\alpha$  is a tolerance parameter [Dolag, Borgani,

Schindler, et al. (2008)]. Softening refers in this context to a dampening of close two body interactions on a given length scale  $\epsilon$  given by a gravitational potential  $\Phi$  as

$$\Phi = -\frac{GM}{\sqrt{r^2 + \epsilon^2}}, \quad (2.2)$$

with  $M$  the total mass and  $r$  the distance. For cosmological simulations this amounts to time steps of  $\Delta t \gtrsim 1$  Myr or, more generally, some fraction of the instantaneous Hubble time [Springel (2005)]. Obviously, this makes fast variable processes of XRBs, as described in section 1.3, impossible to resolve. For this reason, we have to approximate the spectra by assuming time averages of the spectrum. Typical models employed in the literature for point sources with poor photon count statistics or unknown SED are absorbed single power law models with photon index  $\Gamma_L = 1.7$  for LMXBs [see Lehmer, Ferrell, et al. (2020) and Zhang, Gilfanov, and Bogdán (2012)] and  $\Gamma_H \approx 2.0$  for HMXBs [see Sazonov and Khabibullin (2017) and Mineo et al. (2012a)], though Sazonov and Khabibullin (2017) derive their power-law slope from the collective HMXB emission. We obtain similar values by directly computing  $\Gamma$  from equation (1.17) using typical parameters of coronal temperature  $k_B T \approx 100$  keV and optical depth  $\tau \approx 1$ . In chapter 3 we will present a statistical approach to work around the constraints imposed by the simulation framework.

## 2.2 Magneticum Pathfinder Simulations

*Magneticum Pathfinder* simulations are a series of state-of-the-art hydrodynamical cosmological simulations exploring varying ranges in particle number, volume and resolution. They are based on an improved version of the N-body code GADGET 3, which is an updated version of the code GADGET 2 [Springel (2005)] including a Lagrangian method for solving smoothed particle hydrodynamics (SPH). Detailed descriptions regarding the improvements w.r.t. GADGET 3 can be found in the first chapter 1 of Teklu (2018) or see description of the simulation in Dolag, Komatsu, et al. (2016). In summary, the simulations account for treatments of artificial viscosity [Beck et al. (2016) and Dolag, Vazza, et al. (2005)], metal-dependent radiative cooling rates [after Wiersma et al. (2009)] together with UV/X-ray and CMB background [after Haardt and Madau (2001)], a sub-resolution multi-phase model for star formation [Springel and Hernquist (2003)] including stellar feedback in the form of thermal and kinetic energy injection from SN feedback tweaked to also launch galactic winds, a detailed model for chemical enrichment from stellar evolution [Tornatore, Borgani, Dolag, et al. (2007), 2004] SMBH growth through merger and accretion as well as AGN feedback [based on Springel, Di Matteo, et al. (2005), Di Matteo et al. (2005), and Fabjan et al. (2010), improved in Steinborn, Dolag, Hirschmann, et al. (2015) and Hirschmann et al. (2014)], and thermal conduction [Arth et al. (2014) and Dolag, Jubelgas, et al. (2004)]. An overview of the different volumes and resolutions can be found in table 2.1 which was recreated from table 1.1 in Teklu (2018). Initial conditions for the simulations are generated using standard  $\Lambda$ CDM cosmology using results from the *Wilkinson Microwave Anisotropy Probe (WMAP7)* [Komatsu et al. (2011)] to set the parameters. With Hubble parameter  $h = 0.704$ , matter density  $\Omega_M = 0.272$ , dark energy density  $\Omega_\Lambda = 0.728$ , baryon density  $\Omega_b = 0.0451$  and normalization of the fluctuation amplitude at 8 Mpc  $\sigma_8 = 0.809$ . A illustration of the currently available cosmological volumes for *Magneticum* can be seen in figure 2.1 with a detailed description of the resolution in table 2.1.

The *Magneticum* set of cosmological simulations has been successfully used in a multitude of numerical studies which also showed good agreement with observational results of which we will name a few. It was shown in Hirschmann et al. (2014) and Steinborn, Dolag, Hirschmann, et al. (2015), 2016, that properties of the AGN population are consistent with observations.

Box	Size [Mpc/h]	Resolution	$N_{\text{part}}$	$m_{\text{DM}}$ [ $M_{\odot}/h$ ]	$m_{\text{gas}}$ [ $M_{\odot}/h$ ]	$\epsilon_{\text{DM/gas}}$ [kpc/h]	$\epsilon_{\text{star}}$ [kpc/h]
Box0	2688	mr	$2 \times 4536^3$	$1.3 \times 10^{10}$	$2.6 \times 10^9$	10	5
Box1	896	mr	$2 \times 1526^3$	$1.3 \times 10^{10}$	$2.6 \times 10^9$	10	5
Box2b	640	hr	$2 \times 2880^3$	$6.9 \times 10^8$	$1.4 \times 10^8$	3.75	2
Box2	352	mr	$2 \times 594^3$	$1.3 \times 10^{10}$	$2.6 \times 10^9$	10	5
		hr	$2 \times 1584^3$	$6.9 \times 10^8$	$1.4 \times 10^8$	3.75	2
Box3	128	mr	$2 \times 216^3$	$1.3 \times 10^{10}$	$2.6 \times 10^9$	10	5
		hr	$2 \times 576^3$	$6.9 \times 10^8$	$1.4 \times 10^8$	3.75	2
		uhr	$2 \times 1536^3$	$3.6 \times 10^7$	$7.3 \times 10^6$	1.4	0.7
Box4	48	mr	$2 \times 81^3$	$1.3 \times 10^{10}$	$2.6 \times 10^9$	10	5
		hr	$2 \times 216^3$	$6.9 \times 10^8$	$1.4 \times 10^8$	3.75	2
		uhr	$2 \times 576^3$	$3.6 \times 10^7$	$7.3 \times 10^6$	1.4	0.7
Box5	18	hr	$2 \times 81^3$	$6.9 \times 10^8$	$1.4 \times 10^8$	3.75	2
		uhr	$2 \times 216^3$	$3.6 \times 10^7$	$7.3 \times 10^6$	1.4	0.7
		xhr	$2 \times 576^3$	$1.9 \times 10^6$	$3.9 \times 10^5$	0.75	0.25

**Table 2.1:** Sizes, resolutions, particle numbers  $N_{\text{part}}$ , particle mass for dark matter  $m_{\text{DM}}$  and gas  $m_{\text{gas}}$  as well as softening lengths  $\epsilon$  for dark matter/gas and stars for each of the *Magneticum Pathfinder* boxes. Table recreated from table 1.1 in Teklu (2018).

Also in Steinborn, Dolag, Hirschmann, et al. (2015), the derived stellar mass function are in good agreement with observations. Remus, Burkert, et al. (2013) studied dynamical properties of massive spheroidal galaxies which were complemented by a study on dynamical properties of early-type galaxies in Schulze, Remus, Dolag, Burkert, et al. (2018). Furthermore, Schulze, Remus, Dolag, Bellstedt, et al. (2020) studied the stellar kinematics of galaxies out to large radii. In Remus, Dolag, et al. (2017), the radial slopes of the dark matter fraction in early type galaxies and the mass-size relations of galaxies with different morphologies were studied. Dolag, Komatsu, et al. (2016) provided predictions of the expected Sunyaev-Seldovich signals and in Dolag, Mevius, et al. (2017) observed relations for metal abundances in different parts of galaxies matched the simulations. Lotz et al. (2019) studied the effects of cluster environments on the quenching of star-formation in galaxies. With many more studies to come...

### Sub-grid Star-Formation model

Here, we will go into more detail about the star-formation model employed in *Magneticum*. It is based on the model of Springel and Hernquist (2003) which distinguishes baryons into an ISM, with a hot and cold phase, and stars. The phases interact through radiative cooling, SN feedback in the form of ISM heating and cloud evaporation, galactic winds, metal-enrichment and star-formation. The equilibrium temperature of the hot phase is regulated by SNe under the assumption that timescale to reach equilibrium is shorter than any other timescale. The free parameter in this model is the star-formation timescale  $t_*$  which is tuned to the observationally constrained Schmidt-Kennicutt relation [Kennicutt (1998) and Schmidt (1959)]. The ISM is then described by using spatially averaged properties and global dynamics, i.e. average density and dispersion within the represented volume, of the medium. A single SPH fluid element then represents a portion of the ISM where it is assumed that cold clouds are in pressure equilibrium with the hot ambient gas, above a given threshold density  $\rho_{th}$ . Note, that the multi-phase structure remains unresolved. Instead, statistical properties emerge

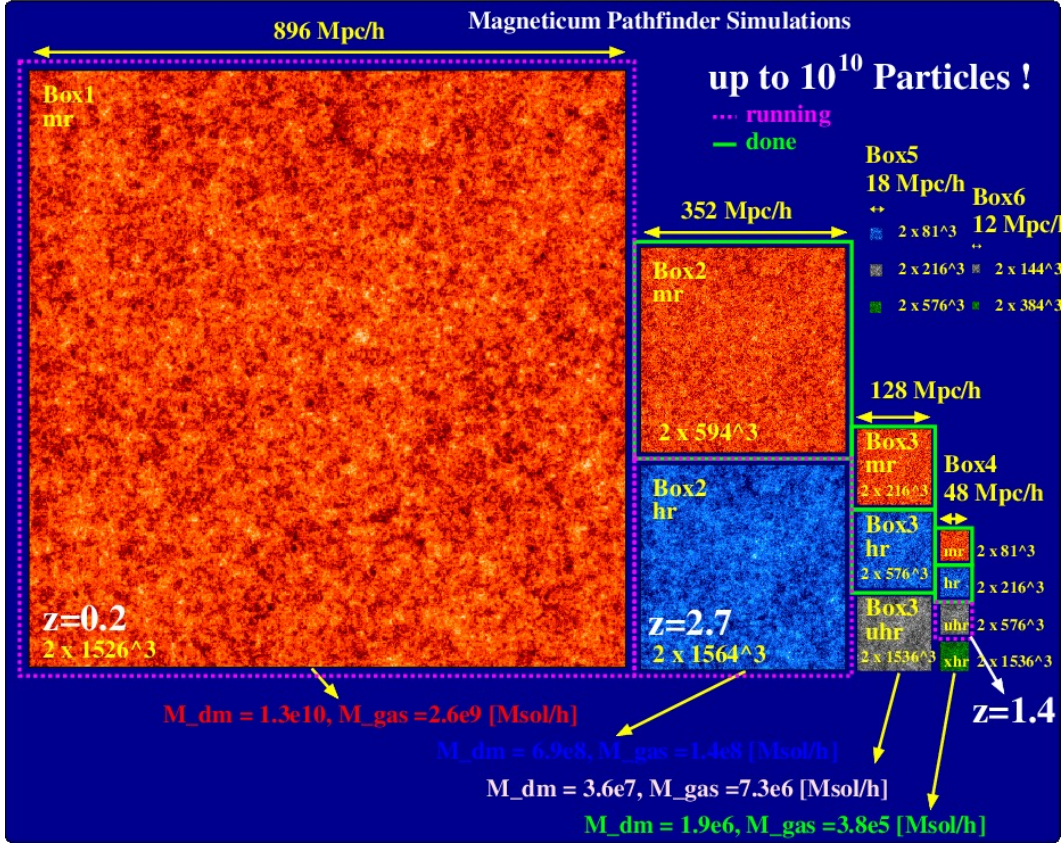


**Figure 2.1:** Illustration of the different cosmological volumes within the *Magneticum* set of simulations. Indicated are box sizes, number of particles (dark matter + gas)

from energy transfer rates which are calculated in the background. Hot gas can be further heated by energy injection from SNe ( $10^{51}$  erg) which sets the cloud evaporation efficiency. The threshold density is then self-consistently computed requiring that the hot-phase temperature at threshold is equal to the thermal instability temperature  $T_{ti}$  and the specific effective energy changes continuously [Tornatore, Borgani, Dolag, et al. (2007)]. If the gas particle exceeds the density threshold, it will be transformed into a stellar particle with a characteristic timescale  $t_*$  resulting in the star-formation rate, following the stochastic approach of Katz et al. (1996), as

$$\dot{M}_* = (1 - \beta) \frac{x \cdot m}{t_*}, \quad (2.3)$$

$$t_* = t_0^* \left( \frac{\rho}{\rho_{th}} \right)^{-\frac{1}{2}}, \quad (2.4)$$

where  $\beta = 0.1$  is the fraction of stars exploding as a type 2 SN, and  $x \cdot m$  is the cold gas mass with  $x = \rho_c / \rho$  being the fraction of gas in cold clouds. From equation (2.3), we get the expected mass of stars formed in a time interval  $\Delta t$  as

$$M_* = m \left\{ 1 - \exp \left( - \frac{(1 - \beta)x\Delta t}{t_*} \right) \right\}. \quad (2.5)$$

A star particle will then be created if a random number  $p \in [0, 1]$  falls below the probability

$$p < \frac{m}{M_*} \left\{ 1 - \exp \left( - \frac{(1 - \beta)x\Delta t}{t_*} \right) \right\}. \quad (2.6)$$

One has to keep in mind, that in this set of simulations, gas particles are allowed to spawn stars more than once ( $M_* = m/N_*$ ). In the case of *Magneticum* up to  $N_* = 4$  generations of stars can be spawned from a single gas particle. The mass of each created stellar particle is then removed from gas particle. Stellar particles are decoupled from the SPH treatment s.t. they only act gravitationally and become effectively collisionless. Note, that while the global SFR is well represented within the simulation volume, there can be local star-formation bursts due to the stochastic way, a gas particle will be chosen by equation (2.6). The now spawned stellar particle represents a single stellar population (SSP) where all stars share the same metallicity and are distributed according to some IMF. In our case, stars in a SSP are initially distributed according to a Chabrier IMF [Chabrier (2003)]. Note, that for the simulations studied here, we sample the Chabrier IMF up to  $100 M_\odot$  but assume that everything down to  $40 M_\odot$  is immediately returned as SN feedback at the moment of creation since their lifetime (see equation (1.1)) is shorter than the temporal resolution of the simulation. Subsequently, the mass of stellar particles reduces continuously since the more massive stars will return most of it back to the hot gas phase through SNe, and simultaneously enrich the hot phase ISM with metals. Details of the implementation can be found in Tornatore, Borgani, Dolag, et al. (2007). Also coupled to the SFR feedback of the sub-grid model are stellar feedback driven galactic winds which reach velocities of the order  $v_{wind} \simeq 350 \text{ km s}^{-1}$  and help enrich the inter galaxy medium (IGM) and intra cluster medium (ICM).

### AGN feedback

Another feedback process, we will describe in more detail, comes from gas accretion onto SMBHs. They are considered to be collisionless "sink particles" that can grow in mass through spherical accretion similar to equation (1.18). Additionally, a boost factor of  $f_{boost} = 100$  is chosen to enhance the accretion. Since the accretion flows are unresolved, BH growth can only be inferred from the large scale gas distribution. After determining the accretion rate, gas particles in the BHs vicinity are fractionally removed which means that a fraction of the gas particle mass will be added to the BH particle. Only using a fraction of the gas instead of the full mass [e.g. Springel, Di Matteo, et al. (2005)] allows for a more continuous description since one gas particle can contribute to accretion more often. The corresponding radiated luminosity can be estimated from the accretion rate using

$$L_r = \epsilon_r \dot{M} c^2, \quad (2.7)$$

with radiative efficiency  $\epsilon_r = 0.1$  according to accretion disc theory for a non-rapidly spinning BH [Shakura and Sunyaev (1973) or see Maio et al. (2013) and references therein], and  $c$  the speed of light. This stems from equation (1.14) by assuming  $\beta = 1$  and using three Schwarzschild radii as the last stable inner orbit for a non-rotating BH  $R_{in} = 3R_S = 6GM/c^2$ . The missing factors are then accounted for by  $\epsilon_r$ . The rate of energy feedback to the surrounding gas can be expressed as

$$\dot{E}_f = \epsilon_f \epsilon_r \dot{M} c^2, \quad (2.8)$$

with  $\epsilon_f$  as a free parameter typically set to 0.1 [Steinborn, Dolag, Hirschmann, et al. (2015)] for the feedback efficiency. By monitoring the Eddington ratio  $f_{edd} = \dot{M}/\dot{M}_{edd}$  as a measure for the accretion activity, we can decide whether the BH is in a quasar ( $f_{edd} > 10^{-2}$ ) or radio state ( $f_{edd} < 10^{-2}$ ). For the latter case, we increase the feedback efficiency in order to account for AGN jets inflating hot bubbles in the ISM. Black hole growth can thus be modelled by

$$\Delta M = (1 - \eta) \dot{M} \Delta t, \quad (2.9)$$

where  $\eta$  is the fraction of mass returned to the ISM.

## 2.3 The photon simulator PHOX

Dealing with emission spectra in any spectral band, from gaseous and stellar components, would require costly on-the-fly modelling of the emitting component. Additionally, the emission from these components would be changing during the course of the simulation. For this reason, spectral modelling is mostly done as a post processing step using intrinsically stored properties of the resolution elements. One such post processing approach was introduced with the virtual X-ray observatory PHOX [Biffi, Dolag, Böhringer, et al. (2012)]. In order to be able to compare results from X-ray observations of galaxy clusters, galaxy halos and AGNs with output from numerical simulations, PHOX converts the self-consistently tracked properties of eligible resolution elements (RE) in the simulation into photon data using appropriate models. In this context, eligible means that the RE in question is able to produce X-ray emission. While there are numerous approaches on how to extract those properties, the novelty introduced in PHOX lies in the separation of the photon generation and the projection. Each step of a virtual observation can thus be carried out individually, requiring the initial photon generation to be executed only once. In the following we will present the exact approach PHOX uses in more detail. Figure 2.3 shows a flow chart illustrating the main units of PHOX.

### 2.3.1 General code structure

This section and the description of PHOX units is mostly based on Biffi, Dolag, Böhringer, et al. (2012). PHOX consists of a C code which makes use of the publicly available X-ray package XSPEC [see Arnaud (1996)] to calculate model emission spectra. It further utilises the external, auxiliary libraries GSL<sup>1</sup> and CFITSIO<sup>2</sup>. It is structured into three units where each unit can be executed independently from the other components. The input for PHOX is required to be the output of a hydrodynamical cosmological simulation. Every snapshot of the simulation contains information about its redshift and embedded cosmology as well as about intrinsic quantities of the tracked particles such as mass, density, position, velocity, etc. Currently, PHOX is mostly tailored towards particle based-codes with SPH, in particular the N-body/SPH code GADGET-2 [see Springel (2005)]. However, the very general approach can be adapted for grid-based simulations performed with Adaptive Mesh Refinement codes like ART [see Kravtsov, Klypin, et al. (2002) and Kravtsov (1999)] or RAMSES(?). Since PHOX will be able to produce model emission for the gaseous component [Biffi, Dolag, Böhringer, et al. (2012)], the AGN component [Biffi, Dolag, and Merloni (2018)] and the XRB component [this work], we will refer to them as "resolution elements" (RE). The treatment of the XRB component will be described in chapter 3.

#### Unit 1

The first crucial step is to convert the simulation data of a box of REs into a corresponding box of photons, before applying any projections or integrating the emission along the line of sight. This guarantees a high spatial and spectral precision taking into account the three-dimensional structure of the REs. Depending on which model spectrum, energy range and the corresponding number of channels for spectral binning is desired, the user can specify those in an input parameter file. The chosen model will not be convolved with an instrumental response at this point but with an identity matrix to allow for fine binning over a wide energy band. Instead of using the redshift and associated angular-diameter distance  $\mathcal{D}_A$  derived

<sup>1</sup>See <http://www.gnu.org/s/gsl>

<sup>2</sup>See <http://heasarc.gsfc.nasa.gov/fitsio/>

from the simulation output, the user can specify a fiducial value  $\mathcal{D}_{A, fid}$  instead, effectively moving the simulation output to a different redshift. The main calculation performed in this framework is to compute the emission associated to each component by successively iterating over every RE, making the code naturally suitable for parallelization. The simulator then populates the spectrum of each RE with a distribution of photons, without storing every spectrum or building of spectral libraries. Specifically, a set number of  $N_{ph}$  photons are randomly drawn in a Monte-Carlo-like simulation according to a previously calculated cumulative spectrum. The number of photons  $N_{ph}$  is determined by the total counts expected from the assumed spectral model (in units of photons/s/cm<sup>2</sup>), the collecting area  $A_{fid}$  and observing time  $\tau_{obs, fid}$ , which can be specified by the user as well, amounting to the relation

$$N_{ph} \propto A_{fid} \times \tau_{obs, fid}. \quad (2.10)$$

The resulting photons are therefore characterised by energy (in the emitting element rest-frame), position and velocity, where the position and velocity are the same as for the RE the photons belong to. This allows for a convenient method of storing the photon data, namely using packages. Since the position and velocity of each RE need only be saved once, a separate file containing all photon energies w.r.t the corresponding RE can be stored. Furthermore, redundant REs, which don't emit photons, are not stored in those package files. Ideally, the fiducial values  $A_{fid}$  and  $\tau_{obs, fid}$  have to be assumed in such a way that the spectra are largely over-sampled in order to permit a dramatic reduction in photon number after applying geometrical selection, projection and instrumental response in the following units. Finally, from the box of resolution elements of the simulation, unit 1 creates a box of photons of the same size.

## Unit 2

This unit takes the output of unit 1 and applies the geometry of the observation to be simulated. Specifically, a user-specified parameter file can be used to select sub-regions of the photon cube, a line of sight (l.o.s.) direction, real collecting area  $A$  and time  $\tau_{obs}$  for the mock observation. The photons which do not geometrically belong to the specified region (usually a cylindrical shape) will be discarded. The remaining ones inside the region of interest will be corrected for the Doppler-Shift caused by the velocity component of the original RE in the l.o.s. direction  $v_{l.o.s.}$ . The correction from the emitted to the observed frame is expressed as

$$E_{ph}^{obs} = E_{ph}^{em} \sqrt{\frac{1 - \beta}{1 + \beta}}, \quad (2.11)$$

where  $\beta = v_{l.o.s.}/c$  and  $c$  the speed of light. Additionally, the sample of obtained photons has to be further filtered according to the specified collecting area  $A$  and exposure time  $\tau_{obs}$ . The appropriate re-scaling factor  $f$  is then calculated with

$$f = \frac{A \tau_{obs}}{A_{fid} \tau_{obs, fid}} \times \frac{\mathcal{D}_{A, fid}^2}{\mathcal{D}_A^2}, \quad (2.12)$$

and by assuming it as a probability for each photon to be actually observed. This also accounts for the possibility to re-scale the number of observable photons, in case the angular diameter distance  $\mathcal{D}_A$  differs from the fiducial value in unit 1, effectively allowing for changes in the observed redshift post-process. All photons coming from a single element will be redistributed according to a radial Gaussian with  $\sigma_r$  of a fraction of the RE's smoothing length. Note, that unit 2 acts independently from unit 1 and does no longer require the

original input used for unit 1. As such, changes in the specifications regarding the mock observation can be included easily which allows the study of the same source from many different line of sights as the original photon cube remains unchanged. Unit 2 then outputs a photon list in a format suitable for convolution with the technical response of a specific instrument, or for an external software dedicated to simulate a specific X-ray satellite.

### Unit 3

In the last unit 3, the mock observation is completed by considering a real telescope. Technical characteristics of a specific instrument are defined by the redistribution matrix (RMF) and the ancillary response file (ARF). Convolution of the photon list obtained in unit 2 with the RMF and ARF yields event files satisfying the standards of real X-ray observations. This enables analysis with the same procedures and tools used for real data. In general, the RMF and ARF are provided by the user and are not predetermined by unit 3. Special care has to be taken for the normalization of the effective area defined in the ARF, w.r.t. the effective area assumed during the projection phase in unit 2 in order to avoid unphysical overabundance of observed photons.

#### 2.3.2 Emission model for hot gas

The gaseous component in cosmological simulations is typically described by thermodynamical properties, such as density, temperature and metallicity. We can derive a thermal Bremsstrahlung continuum from the density and temperature of the gas, which is used to describe the hot plasma in the ICM of galaxy clusters. The metallicity is used to additionally include emission lines from heavy ions. The continuum takes the form

$$\varepsilon_{ff}(\nu) = \frac{32\pi e^6}{3c^3 m_e} \left( \frac{2\pi}{3m_e k_B} \right) g_{ff}(Z, T; \nu) Z^2 n_e n_i \exp \left\{ - \left( \frac{h\nu}{k_B T} \right) \right\}, \quad (2.13)$$

where  $e$  is the electric charge,  $m_e$  is the mass of the electron,  $c$  the speed of light,  $k_B$  the Boltzmann constant,  $Z$  the charge of the ion partaking in the interaction,  $T$  the plasma or hot gas temperature, which in the case of galaxy clusters can be inferred from their mass and vice versa,  $n_e$  the electron number density,  $n_i$  the ion number density,  $h$  is Planck's constant (only here) and  $g_{ff}(Z, T; \nu) \approx 1$  is the Gaunt factor, usually of order unity. Using databases for atomic energy level transitions, either a MEKAL [Mewe et al. (1985), Kaastra and Mewe (1993), and Liedahl et al. (1995)] or an APEC [Smith et al. (2001)] single-temperature, thermal emission model for hot plasma can be calculated using XSPEC. Additionally, an absorption component given by the WABS model [Morrison and McCammon (1983)] can be included. Depending on the aims of the conducted observations, the emission model can be adapted to accommodate a detailed description of metal abundances tracked by the simulation's chemical enrichment (using VMEKAL or VAPEC). In this work we will make use of those descriptions to also model the hot gaseous components of single galaxies, namely their halos and the ISM.

#### 2.3.3 Emission model for AGN

For the description of AGN treatment in PHOX we will follow Biffi, Dolag, and Merloni (2018) and references therein. The standard approach to estimate the bolometric luminosity of accreting BHs was introduced in equation (2.7). By measuring the accretion rate  $\dot{M}$  in units of the Eddington accretion rate (see eq. (1.22)), we can define a dimensionless parameter,

i.e. the BH accretion rate (BHAR)

$$\text{BHAR} = \frac{\dot{M}}{\dot{M}_{\text{edd}}}, \quad (2.14)$$

which can be used to differentiate between the quasar (BHAR > 0.1) and radio regime (BHAR < 0.1) of the AGN. Following Churazov et al. (2005), the resulting AGN luminosity can then be expressed as

$$\frac{L_r}{L_{\text{edd}}} = \begin{cases} \epsilon_r \left( 10 \frac{\dot{M}}{\dot{M}_{\text{edd}}} \right) & , \text{ if BHAR} > 0.1 \\ \epsilon_r \left( 10 \frac{\dot{M}}{\dot{M}_{\text{edd}}} \right)^2 & , \text{ if BHAR} < 0.1 \end{cases} \quad (2.15)$$

which we note uses different accretion ratios ( $f_{\text{edd}} = \text{BHAR}$ ) from the prescription used in determining the AGN feedback in *Magneticum* (see sec. 2.2). As it turns out, the reconstructed bolometric luminosity functions, using data from Hopkins et al. (2007), do only weakly depend on the employed estimation. We therefore adopt the standard estimation as in equation (2.7). Using the third-degree polynomial bolometric corrections presented in Marconi et al. (2004), we can convert the bolometric luminosities into X-ray luminosities of the soft X-ray band (SXR: 0.5 – 2 keV) and the hard X-ray band (HXR: 2 – 10 keV) with

$$\log \left( \frac{L_{\text{HXR}}}{L_{\text{bol}}} \right) = -1.54 - 0.24\mathcal{L} - 0.012\mathcal{L}^2 + 0.0015\mathcal{L}^3, \quad (2.16)$$

$$\log \left( \frac{L_{\text{SXR}}}{L_{\text{bol}}} \right) = -1.65 - 0.22\mathcal{L} - 0.012\mathcal{L}^2 + 0.0015\mathcal{L}^3, \quad (2.17)$$

where  $\mathcal{L} = \log(L_{\text{bol}}/L_{\odot}) - 12$  derived for the luminosity range  $8.5 < \log(L_{\text{bol}}/L_{\odot}) < 13$ . This choice is motivated by the fact that these corrections were derived from redshift-independent template spectra which are closer to the intrinsic AGN luminosity and theoretical estimates of  $L_{\text{bol}}$  from simulations. Assuming an intrinsic power-law spectrum of the form  $E^{-\alpha}$ , with photon index  $\alpha$  in the range of 1.4-2.8 with a Gaussian distribution peaked at  $\sim 1.9 - 2.0$ , for every AGN, we model the AGN spectrum in PHOX according to a single, redshifted power law

$$A(E) = [K(1+z)][E(1+z)]^{-\alpha} \left( \frac{1}{1+z} \right), \quad (2.18)$$

$$= K[E(1+z)]^{-\alpha}, \quad (2.19)$$

with  $K$  as the normalization of the observed spectrum and  $z$  for the redshift. Using eq. (2.18) we can calculate the luminosity in the SXR and HXR band in the object's restframe with

$$\begin{cases} L_{\text{SXR}} = F \int_{0.5/(1+z)}^{2/(1+z)} K[E(1+z)]^{-\alpha} E dE, \\ L_{\text{HXR}} = F \int_{2/(1+z)}^{10/(1+z)} K[E(1+z)]^{-\alpha} E dE, \end{cases} \quad (2.20)$$

with  $L_{\text{SXR}}$  and  $L_{\text{HXR}}$  estimated from equations (2.17) and (2.16) and  $F$  as the conversion factor from flux to luminosity (includes distance to source). Additionally, a Gaussian scatter of  $\sigma = 0.1$  is added on top of both  $L_{\text{SXR}}$  and  $L_{\text{HXR}}$ . We can obtain  $K$  and  $\alpha$  by solving

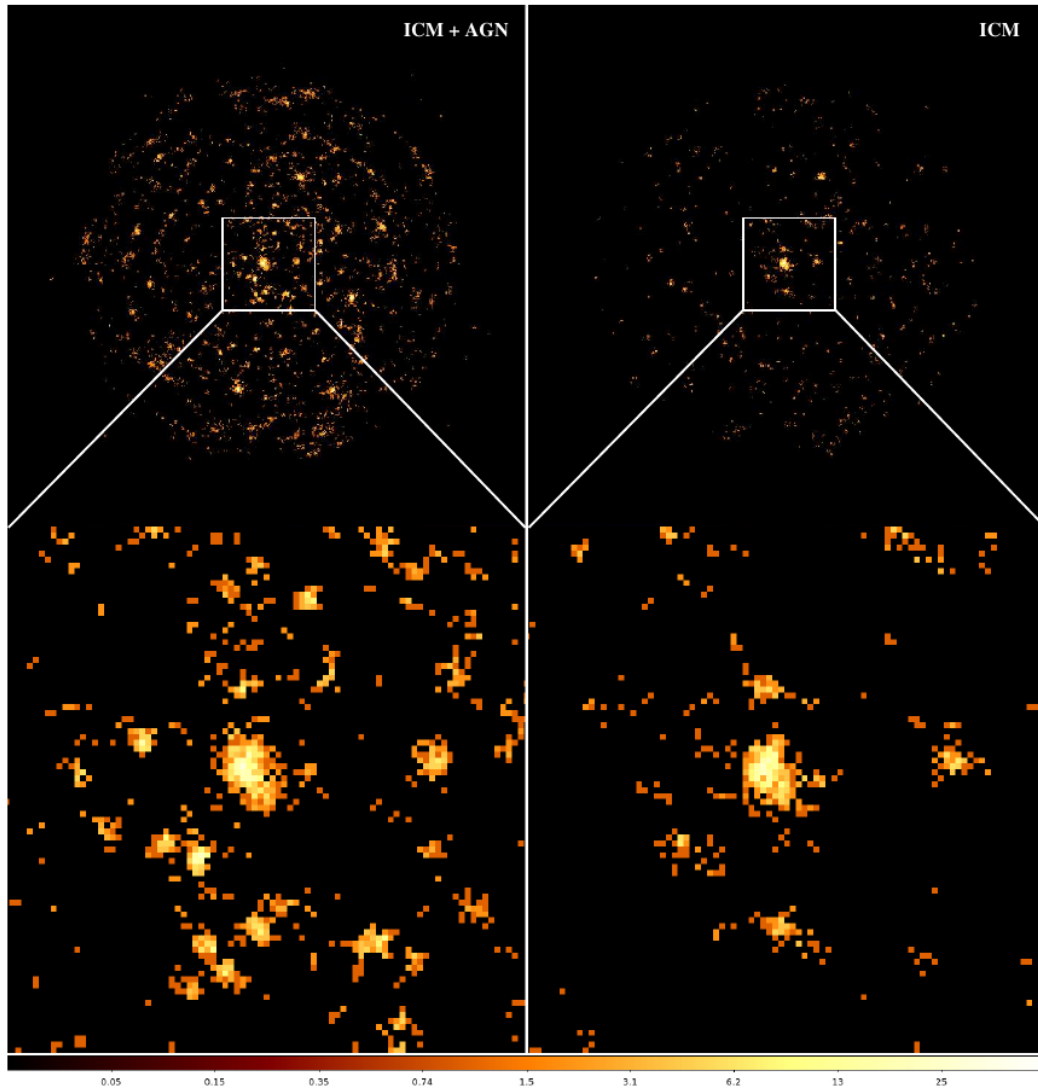


**Figure 2.2:** *eROSITA* mock observation of a galaxy cluster at redshift  $z = 0.1$  illustrating the effects of AGN contamination.

the system of equations (2.20) and use them to calculate the AGN spectrum according to the `zpowerlw` using `XPSEC`. `PHOX` applies this procedure using the intrinsic properties of BH particles of simulations and additionally selects intrinsic absorption coefficients randomly from the distribution presented in Buchner et al. (2014) to account for an obscuring torus using the `zwabs` model. The total spectrum of a BH particle is then computed following the model

$$\mathbf{wabs} \times \mathbf{zwabs} \times \mathbf{zpowerlw}, \quad (2.21)$$

where `wabs` is the galactic foreground absorption. A *eROSITA* mock observation of the AGN contamination in galaxy clusters can be seen in figure 2.2.

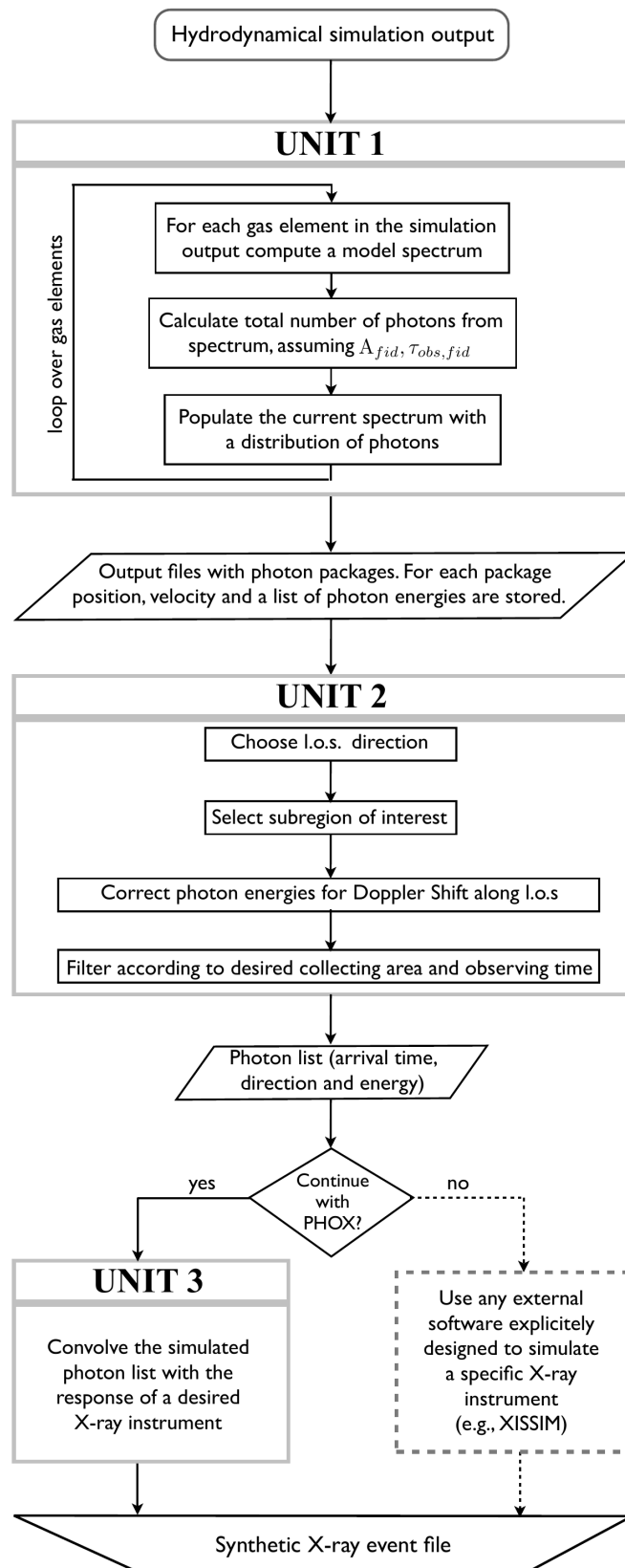


**Figure 2.3:** Flow chart illustrating the main units of PHOX. The dashed box stands for the possibility to use external software designed to simulate observations of a certain X-ray telescope in conjunction with the output of PHOX unit 2. Graphic directly taken from Biffi, Dolag, Böhringer, et al. (2012).



## Chapter 3

# Emission modelling of synthetic XRB populations

In this chapter we will present the procedure to obtain luminosities and spectra for XRBs as a newly added feature in PHOX first unit. We will base the emission model on quantities characterizing the stellar component within the simulation, namely mass, age and IMF. The approach closely follows the implementation for the AGN model, we will however provide some more details on the model specifics.

### 3.1 MC sampling of empirical model

While we were able to calculate estimates for the X-ray luminosities of AGN from their intrinsic properties (see eqs. (2.15)-(2.17)), we do not possess direct information of individual stars represented by a stellar element. In a cosmological framework, stellar elements constitute a SSP, which are statistically evolved during the duration of the simulation. Therefore, we need to devise accurate methods, in order to be able to extract information about a theoretical XRB population within the stellar element. One possible approach uses binary population synthesis models. It works by using galactic scaling relations of the two XRB types, as well as the star formation history (SFH) and metallicity evolution of the universe as inferred from cosmological simulations. One such approach is presented in Fragos, Lehmer, Tremmel, et al. (2013) where they use the binary population synthesis code `StarTrack` Belczynski et al. (2008), semi-analytic galaxy catalogs by Guo et al. (2011), the SFH and metallicity evolution from the MILLENIUM II simulation Boylan-Kolchin et al. (2009) and local galaxy X-ray properties and scaling relations regarding galactic stellar mass and SFR. They find that HMXB dominate the emission for the first 100 Myr of a galaxy after a star formation event and LMXB overtake after 1 Gyr. Also, HMXB emission peaks slightly before the ( $z \sim 3.9$ ) peak of star formation ( $z \sim 3.1$ ) in cosmic evolution. Their model is, however, in significant tension with age observations of local elliptical galaxies [Boroson et al. (2011)]. As old stellar populations are dominated by LMXB emission, they under-predict the almost flat correlation with time presented in Boroson et al. (2011). They attribute this tension to their model not accounting for dynamically formed LMXB in GC and to age estimations of young elliptical galaxies potentially being problematic.

An attempt to circumvent this tension is to abandon theoretical predictions of binary synthesis models and focus only on observational evidence. In particular, the luminosity functions presented in chapter 1 are well suited for this endeavor because they provide a global view on the XRB populations in local galaxies following empirical scaling relations, and can be linked to globally available quantities of the stellar components in the simulations, such as

mass and SFR.

In order to turn LFs into an appropriate tool to assign luminosities to a XRB, we present the following general procedure, suitable for both types of XRBs:

- we integrate the differential LFs presented in eqs. (1.8) and (1.9), by assuming a lower luminosity limit  $L_{\min}$ , to obtain an analytic expression for the expected total number of XRBs of the given type in units of SFR or stellar mass, above  $L_{\min}$

$$N_0 = N(> L_{\min}) = \int_{L_{\min}}^{L_{\text{cut}}} \frac{dN}{dL'} dL', \quad (3.1)$$

- we break eq. (3.1) at  $L_{\min}$  and construct a monotonous pseudo cumulative-density-function (CDF) by re-normalisation and inversion of the original equation

$$C(> L) = 1 - \frac{N(> L)}{N_0}, \quad (3.2)$$

with  $C \in [0, 1]$  and  $L \in [L_{\min}, L_{\text{cut}}]$

- similar to the spectral sampling in PHOX unit 1, we can now use a Monte-Carlo like approach to assign luminosities to a single XRB using eq. (3.2). Assuming a uniformly distributed random number  $p \in [0, 1]$ , we can find the luminosity  $L$  at which  $p = C(> L)$ . In the context of actual code, we have to consider the discrete nature of the problem. The random number  $p$  thus falls into a certain bin of  $[C_1, C_2]$  and consequently into a luminosity range  $[L_1, L_2]$  with  $C_{1,2} = C(> L_{1,2})$  and  $L_1 < L_2$ . We then have to apply corrections based on the position of  $p_i$  with respect to the bin limits to get the true corresponding luminosity

$$L = L_1 + \Delta L \frac{p - C_1}{\Delta C}, \quad (3.3)$$

with  $\Delta C = C_2 - C_1$  and  $\Delta L = L_2 - L_1$ .

Note, that equation (3.2) is scale invariant, meaning that the normalisation of the underlying XLFs do not change the shape of the pseudo CDF. Instead, the scaling relations control the number of expected XRBs  $N'_0$  per galaxy. Here,  $N'_0 = N_0 \times A$ , where  $A$  represents the scaling. Consider a galaxy with  $\text{SFR} = 1 M_{\odot} \text{yr}^{-1}$ , we would thus expect  $N_0$  HMXBs above  $L_{\min}$  in that galaxy according to eq. (3.1), since the XLF for HMXBs is normalized to unit SFR. If the galaxy had  $\text{SFR} = 2 M_{\odot} \text{yr}^{-1}$  instead, we would thus expect  $N'_0 = N_0 \times 2$  HMXBs in that galaxy, assuming a linear scaling of the XLF with SFR. This means, that, in order to populate an entire galaxy with XRBs, we can draw a set  $p_i \in [0, 1]$  of  $N'_0$  uniformly distributed random numbers and use equation (3.3) to generate a population of  $N'_0$  XRBs distributed according to the respective XLF. The resulting raw LF for that galaxy, would be shifted along the  $N(> L)$  axis w.r.t. the  $N(> L)$ - $L$  plane of the XLF, if  $N'_0 \neq N_0$ , but can be easily re-scaled to the original XLF using the underlying relation.

Figure 3.1 presents a visualisation of the procedure presented above. The left panel shows the analytic solution of the XLF for both XRB types. The coloured lines are the reconstructed LF for a XRB population of each type. The population size was set to  $N_0$  which means that  $N_0$  is the next integer number for  $L_{\min}$ . In the LMXB case (orange)  $N_0 = 297$  and in the HMXB case (blue)  $N_0 = 48$  with  $N_0$  after equation (3.1) and both XLFs following the parameter definition in table 1.2 and  $L_{\min} = 10^{36} \text{ergs}^{-1}$ . The LFs were reconstructed by counting how many XRB in the population have a luminosity greater than a certain value. The two right panels show the analytic pseudo CDF calculated according to eq. (3.2) for

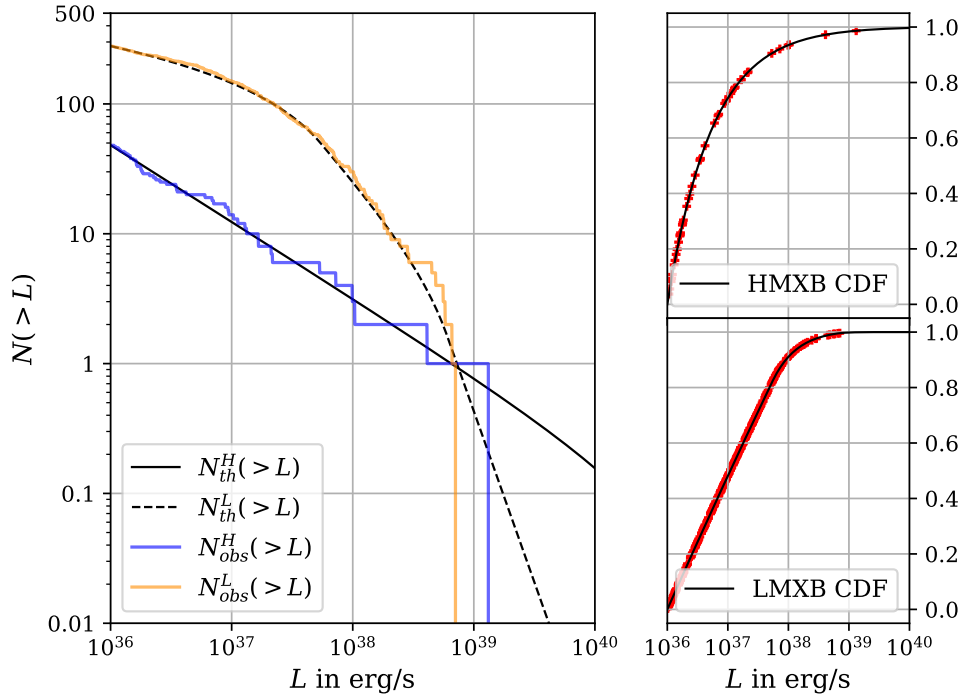


**Figure 3.1:** Illustration of the luminosity sampling of the cumulative XLFs derived from equations (1.8) and (1.9). The left panel shows the two analytic solutions for HMXBs (*solid black*) and LMXBs (*dashed black*). The coloured lines are the reconstructed XLFs by directly counting the number of XRBs above a certain luminosity from an initial sample of  $N_{0,L} = 279$  LMXBs (*orange*) and  $N_{0,H} = 48$  HMXBs (*blue*).  $L_{\min}$  was set to  $10^{36} \text{erg s}^{-1}$ . The two right panels show the corresponding pseudo CDFs (*solid black*) following eq. (3.2). The red crosses indicate the position of a single drawn sample point  $(p_i, L_i)$  from eq. (3.3) with respect to the CDF.

both XRB types. The over-plotted red symbols ('+' signs) represent the discrete distribution of the respective XRB population: each symbol shows the random number  $p_i$  together with its assigned luminosity, calculated according to eq. (3.3). We note that the assignment of luminosities is perfectly aligned with the CDF of the respective XRB type. This shows that our approach is able to accurately sample the CDF and produces XRB populations according to the desired XLFs. The deviation of the reconstructed LF from the analytic model is caused by the discrete sampling of the XLFs with a limited number of points. This choice of under-sampling the luminosity function is deliberate as it reflects the actual behaviour seen in observations. Using this approach, we do not gain information about the spatial distribution of the XRB population inside the galaxy.

## 3.2 Determining the population size from particle quantities

Cosmological simulations pose a limiting factor on the sampling approach presented in section 3.1, since they primarily display a representation of the spatial distribution of different matter components following idealized physical laws. Therefore, structures like galaxies or clusters of galaxies have to be identified from matter over-densities within a certain volume of the simulation post-process [see Dolag, Borgani, Murante, et al. (2009) for a description of the `subfind` algorithm]. Using the estimated properties of the halos defined by this scheme one would be able to estimate the XRB population size but not its spatial distribution within the

halo. This is where PHOX main principle becomes valuable: since we replace the simulation box with a corresponding box of photons, where each photon is associated to a single RE, the distribution of the XRB population should then emerge as a natural consequence of the grouping of stellar REs. We therefore loop over every stellar RE and need to decide which of them are eligible to host a certain type of XRB. We decide this using the age and mass of the stellar RE and make use of the fact that stellar REs are SSPs.

The age of the RE is stored as the age of the simulation at which the element was born. By comparing it to current age of the snapshot being processed, we can calculate, using the intrinsic cosmology, how old the particle is. From life-time estimates in chapter 1 for binary evolution and the specifics of star formation within the simulation (see section 2.2), we can assign a specific XRB type to a certain age of the RE. In our case we chose to assign HMXBs to stellar ages in the range of

$$5 \text{ Myr} < t_H < 100 \text{ Myr} ,$$

and LMXBs when the stellar age is in the range

$$t_L > 1 \text{ Gyr} ,$$

which is also in line with time estimates from Fragos, Lehmer, Tremmel, et al. (2013). In this way we do not have to deal with RE hosting both types of binaries which also enables a clear separation of the two emission components in PHOX where we implemented the possibility to switch off one of the two binary types for the photon simulation. In order to determine the population size for each eligible element, we assume that the scaling relations, derived from local galaxies, hold for the mass resolution of the stellar elements. This is a rather bold assumption, considering there is no generality in the scaling relations for low masses. It is, however, justified in the sense that by segmenting the total mass of a galaxy into smaller chunks, we still capture the total XRB population residing in the galaxy. Even though each chunk will have a lower number of sample points compared to the whole galaxy, the stochastic nature of the approach assures the reconstruction of the original XLF by combining chunks back together. Granted, deviations still occur from the stochastic construction itself as we will demonstrate in chapter 4. Note, that at the mass resolution of individual stars, this scheme would fail since elements are no longer represented by a SSP and need to be tracked individually. In the following we will refer to stellar REs elements associated with LMXB as LMXB element and HMXB element for the HMXB case. If the size of a XRB population per element is greater than 1, we sum over the individual luminosities of the population and take the resulting total luminosity as the value for the emitting element.

### 3.2.1 Mass proportionality of the LMXB population

A straight forward method to determine the population size for a LMXB element is to take its current mass  $m_*$  and use it to determine  $N'_{0,L}$  from the stellar mass scaling relation for LMXB in local galaxies. From the normalisation  $K_1$  of the LMXB XLF (see eq. (1.9)) we know that the number of LMXBs scales with the stellar mass in units of  $10^{11} M_\odot$ . Thus, we get the relation

$$N'_{0,L} = N_{0,L} \times \frac{m_*}{10^{11} M_\odot} , \quad (3.4)$$

where we have to keep in mind that  $m_*$  is given in code units and has to be converted to physical units. Moreover, we need to handle the fact that  $N'_0$  is not a integer number. We can write

$$N'_{0,L} = \lfloor N'_{0,L} \rfloor + q , \quad (3.5)$$

where  $\lfloor N'_{0,L} \rfloor$  is the floored value of  $N'_{0,L}$  representing the integer number part and  $q \in [0, 1]$  is the decimal value of  $N'_{0,L}$ . The floored whole number determines how often we have to sample from the XLF at least, while  $q$  stochastically determines whether to sample for an additional XRB or not. We do this also in a probabilistic way by drawing a uniformly distributed random number  $p_L \in [0, 1]$ . If  $q < p_L$ , no additional XRB will be sampled. With that we assure that we do not consistently under-represent the true number of XRBs in the population. As a reference, assuming a stellar particle mass  $m_* = 1.8 \cdot 10^6 M_\odot$  for *Box4* of *Magneticum*, we would expect

$$N'_{0,L} = 279.22 \times 1.8 \cdot 10^{-5} \approx 0.005$$

LMXBs above  $L_{\min} = 10^{36} \text{ erg s}^{-1}$ . This means that 1 in 200 stellar elements with an age  $t_L > 1 \text{ Gyr}$  will get *one* LMXB with a luminosity of at least  $10^{36} \text{ erg s}^{-1}$ .

### 3.2.2 Formation efficiency of HMXBs as a SFR proxy

For the determination of the population size for a HMXB element, we adopt an approach similar to the one presented in section 3.2.1. Namely, we assume a linear scaling of the XLF normalization of HMXBs with the star formation rate  $\xi \times \text{SFR}$  from equation (1.8). The population size  $N'_{0,H}$  can then be calculated with

$$N'_{0,H} = N_{0,H} \times \text{SFR}. \quad (3.6)$$

But, we recall that for cosmological simulations the star formation rate is defined as the rate at which a gas element is currently forming stars (see section 2.2), so that, pure stellar elements in the simulation hold no information about their previous star formation history as they are created instantaneously. On the other hand, if we estimated the SFR as the stellar mass created during the last 100 Myr, the SFR would only be globally accurate for a halo-sized object. Since we don't want to assign a global value for the SFR to HMXB elements in a predefined region of the simulation, but rather favour using intrinsic properties of the stellar elements, we have to instead find a suitable estimator for the SFR to be assigned to every stellar element. In Shtykovskiy and Gilfanov (2007),2005 the authors present a study on the HMXB population within the Small Magellanic Cloud. They reconstructed the spatially resolved SFH of the dwarf galaxy and used it to constrain the formation efficiency  $\eta_{\text{HMXB}}(t)$  of HMXBs given the time  $t$  past a star formation event. It is defined as

$$\eta_{\text{HMXB}}(t) = \frac{N_{\text{HXB}}}{M(> 8 M_\odot)}, \quad (3.7)$$

where  $t$  is the time past since the star formation event,  $N_{\text{HXB}}(t)$  is the number of HMXB that formed, and  $M(> 8 M_\odot)$  is the total mass of the stars more massive than  $8 M_\odot$ . They also directly relate the formation efficiency to the HMXB XLF normalization presented in Grimm et al. (2003) via

$$\int \eta_{\text{HMXB}}(t) dt = \frac{N(L > L_{\text{lim}})}{\text{SFR}}, \quad (3.8)$$

which makes the connection between the SFR and the stellar mass formed in massive stars. In figure 3.2 we show the formation efficiency of HMXBs together with the age limits imposed on the HMXB elements to be eligible. By assuming a constant formation efficiency of

$$\eta_{\text{HMXB}} = 3 \cdot 10^{-5} M_\odot^{-1},$$

which is the bin weighted average of the efficiency based on the values seen in figure 3.2. We can simply get the expected size of the HMXB population for a single element using its initial mass  $m_i$  at creation

$$N'_{0,H} = \eta_{\text{HMXB}} \times m_i \times \mu(> 8 M_{\odot}), \quad (3.9)$$

where  $\mu(> 8 M_{\odot})$  is the fraction of massive stars as derived from a mass normalized IMF. In the case of *Magneticum Box4*, we have a mass normalized Chabrier IMF [Chabrier (2003)] of the form

$$\xi(m) = \begin{cases} 0.241367 m^{-2.3}, & 1.0 M_{\odot} < m < 100 M_{\odot} \\ 0.241367 m^{-1.8}, & 0.5 M_{\odot} < m < 1.0 M_{\odot} \\ 0.497056 m^{-1.2}, & 0.1 M_{\odot} < m < 0.5 M_{\odot} \end{cases}, \quad (3.10)$$

which yields  $\mu(> 8 M_{\odot}) \approx 0.229$ . Additionally, we have to set  $L_{\text{lim}} = 10^{34} \text{ erg s}^{-1}$  in order to keep the efficiency parameter consistent, since Shtykovskiy and Gilfanov (2007) use HMXB data with the same limit. Using the same example as in section 3.2.1 with  $m_i = 1.8 \cdot 10^6 M_{\odot}$  we get

$$N'_{0,H} \approx 12.36$$

as the population size for a HMXB element. With the same probabilistic approach as in the LMXB case to sample for an additional HMXB, we take a uniformly distributed random number  $p_H \in [0, 1]$  and compare it to the decimal number part  $q$  of  $N'_{0,H}$ . This means for the example presented here, that 36% of stellar elements with an age  $5\text{Myr} < t_H < 5\text{Myr}$  will get 13 HMXBs and the remaining 64% will get 12 HMXBs of at least  $L_{\text{lim}} = 10^{34} \text{ erg s}^{-1}$  in both cases. We use the initial mass of the stellar element in order to account for all massive stars that were initially born with the RE. We assumed a constant value for the efficiency  $\eta_{\text{HMXB}}$  because we initially intended to use it as a test case for a suitable SFR proxy. Note that this HMXB population of  $\sim 12$  is attributed to a single stellar element. Prompted by the success of the test cases we did not adapt the model to a finer time binning also due to the large error bars of  $\eta_{\text{HMXB}}$  presented in figure 12 of Shtykovskiy and Gilfanov (2007) where they plot  $\eta_{\text{HMXB}}$  as a function of time past a star-formation event.

### 3.2.3 Assigning spectral parameters

After assigning a total luminosity to each XRB element, drawn from the population size according to the respective LFs, we need to determine the spectral parameters for the emitting elements. In analogy to the AGN model, also for XRBs we model the spectral shape as a simple redshifted power law according to equation (2.18). Following the reasoning presented in section 2.1, we assume that the XRB power-law slope is well represented with photon indices  $\Gamma_L = 1.7$  for LMXBs and  $\Gamma_H = 2$  for HMXBs, in line with theoretical assumptions for typical XRBs presented in section 1.3. The respective luminosity functions both report luminosities within the 0.5 – 8 keV band. From that, we calculate power law normalization  $K$  at 1 keV with

$$L_{\text{tot}} = K \cdot F \int_{0.5/(1+z)}^{8/(1+z)} [E(1+z)]^{-\Gamma_{L,H}} E dE, \quad (3.11)$$

where  $F = 4\pi \mathcal{D}_L^2 \times \text{KEV\_TO\_ERG}$  is the conversion factor between flux and luminosity with  $\text{KEV\_TO\_ERG} = 1.602 \cdot 10^{-9} \text{ erg keV}^{-1}$  and  $\mathcal{D}_L = (1+z)^2 \mathcal{D}_A$  is the luminosity distance. In general, we get for  $\Gamma \neq 2$  that

$$K = \frac{L_{\text{tot}}(2-\Gamma)(1+z)^2}{F(8^{(2-\Gamma)} - 0.5^{(2-\Gamma)})} \quad (3.12)$$

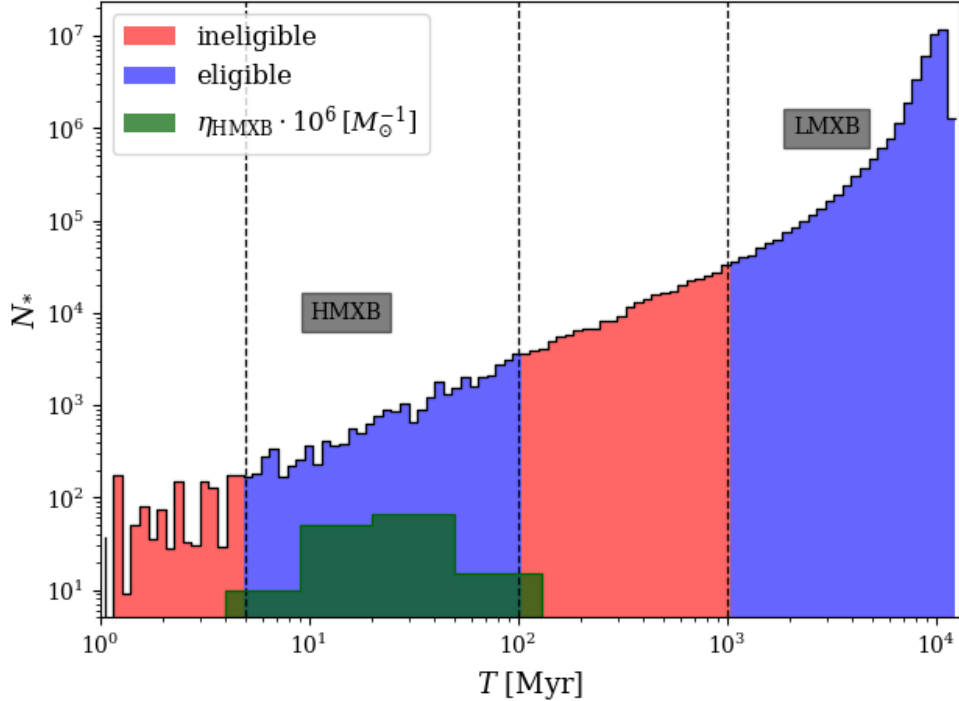


**Figure 3.2:** Age distribution of stellar particles for the 500 most massive halos in *Box4* of *Magneticum*. The dashed vertical lines at 5, 100 and 1000 Myr mark the age boundaries used to determine the eligibility of a stellar element to host a XRB component. The reds histogram shows the distribution of rejected stellar ages. The blue histograms shows the distribution of elements fulfilling the age conditions  $5 \text{ Myr} < t_H < 100 \text{ Myr}$  and  $t_L > 1 \text{ Gyr}$ .  $N_{\text{str}}$  is the number of stellar elements per age bin. The green histogram shows the formation efficiency  $\eta_{\text{HMXB}}(t)$  of HMXBs from Shtykovski and Gilfanov (2007). Number fractions are given in table 3.1.

In order to save computation time, it is more convenient to build a template spectrum using a normalization of  $K = 1$  for our simple case. The individual spectra are then just scaled versions of the template using  $K$  from equation (3.12). If we decide to implement a more sophisticated model, we have to eventually return to calculating the spectrum for each element individually again. We also include a galactic foreground absorption using the `wabs` model incorporated in `XSPEC`. Furthermore, we reserve the possibility to also have an intrinsic absorption component for XRB accounting for heavily absorbed systems. We set the intrinsic absorption coefficient to 0 for now, as it is not clear what the fraction of those intrinsically absorbed systems is. The total spectral model adopted for `XSPEC` then reads

$$\text{wabs} \times \text{zpowerlw}. \quad (3.13)$$

The photon simulation then follows the steps described in section 2.3 on unit 1.

$N_{\text{HXB}}/N_{\text{tot}}$	$N_{\text{LXB}}/N_{\text{tot}}$	$N_{\text{inel}}/N_{\text{tot}}$	$N(< 5 \text{ Myr})/N_{\text{HXB}}$
0.08%	99.21%	0.79%	3.89%

**Table 3.1:** Number fractions of eligible and ineligible XRB elements based on figure 3.2.



# Chapter 4

## Analyzing spectra of simulated galaxies

In this chapter, we will present our findings concerning the composition of synthetic X-ray spectra of simulated galaxies from *Magneticum* using all emission components implemented in PHOX. The structure of this chapter is as follows: in the first section we describe the data sets and the specifics for data retrieval. Section 4.2.2 then deals with the recovery of empirical scaling relations and luminosity functions of simulated galaxies using data from *Magneticum Box4/ubr*. In section 4.3 we analyze the emission ratio between XRB emission and the other two X-ray components as well as between the two distinct XRB components for a larger set of simulated galaxies from *Magneticum Box4/ubr*. In section 4.4 we study the dependence of the relative XRB contribution using different galactic properties, in particular SFR, stellar mass and Hubble type. Finally, in section 4.5 we construct a lightcone from  $z \sim 0$  to  $z \sim 2$  using data from *Magneticum Box2/hr* and analyze the composition of the resulting X-ray background.

### 4.1 The data

For our analysis, we use two different sets of galaxies extracted from *Magneticum Box4/ubr* at a redshift of  $z = 0.066$  using an updated version of the `subfind` algorithm [Dolag, Borgani, Murante, et al. (2009)]:

1. **Set 1** is a smaller set of halos, consisting of  $N_g = 308$  galaxies which were classified as 135 late-type galaxies (LTG) and 173 early-type galaxies (ETG) using their  $b$ -value [see Teklu et al. (2015)] with a stellar mass range of  $1 \cdot 10^{10} M_\odot$  to  $8 \cdot 10^{11} M_\odot$ .
2. **Set 2** is a large set of halos, consisting of  $N_g = 1420$  galaxies in a stellar mass range of  $9 \cdot 10^9 M_\odot$  and  $3 \cdot 10^{12} M_\odot$ .
3. **Set 3** consists of  $N_g = 584$  of varying morphologies of which **Set 1** is a subset. This set was only used to produce figure 4.8.

The simulation employed, *Box4/ubr*, comprises a cosmological volume of  $(48 \text{ Mpc}/h)^3$  with the same number of dark matter and gas particles,  $576^3$ , respectively. Each dark matter particle has a constant mass of  $m_{DM} = 3.6 \cdot 10^7 M_\odot$  and gas particles have a starting mass of  $m_{gas} = 7.3 \cdot 10^6 M_\odot$ . We applied PHOX unit 1 for each emission component to the simulation output using fiducial values for the observing time of  $\tau_{obs} = 10^6 \text{ s}$  and the effective area

$A_{fid} = 10^3 \text{ cm}^2$  assuming a constant galactic foreground column density of  $N_H = 10^{20} \text{ cm}^{-2}$ . The spectra were generated in the energy range of  $E_{\min} = 0.05 \text{ keV}$  and  $E_{\max} = 50.1 \text{ keV}$  using  $5 \cdot 10^4$  energy channels. Gas emission was calculated using the APEC model with varying metallicity among gas particles. AGN emission was calculated using the standard bolometric luminosity estimator (see equation (2.7)) and XRB emission was calculated by simultaneously producing photons for each binary type with lower luminosity limit  $L_{lim}^H = 10^{34} \text{ erg s}^{-1}$  for HMXBs and  $L_{lim}^L = 10^{35} \text{ erg s}^{-1}$  for LMXBs. For section 4.2 and figure 4.8 we produced the emission for the two binary types separately and artificially reduced  $\mathcal{D}_{A,fid}$  from  $\sim 337 \text{ Mpc}$  to  $\sim 43 \text{ Mpc}$  for better photon statistics. The rest of this chapter combined both XRB types into a single emission profile.

We then projected the photon data for each galaxy of our data sets using PHOX unit 2 where we kept observing time  $\tau_{\text{obs}}$ , effective area  $A$  and angular distance  $\mathcal{D}_A$  the same as their fiducial values from unit 1. The projected cylindrical volume was set to be the  $\pi r_{2500}^2 \times 2r_{2500}$ , where  $r_{2500}$  is the radius within which the halo over-density is 2500 times higher than the critical density of the universe at the given redshift. The resulting files retain the structure of the photon packages, namely that energy and position of each photon is derived from its original particle. Note, that the projection also applies a Gaussian scatter to the photon positions using the smoothing length of the original particle. From this point on, we will refer to the photon projection of the simulated galaxies when talking about 'galaxies'. We also remind that, for the purpose of the current study, we never employ PHOX unit 3 for any of our analysis, so we are always considering raw unfolded spectra without including any specific telescope response.

## 4.2 Recovering empirical Relations

In this section we will present our results obtained from recovering observationally constrained scaling relations of galaxies.

### 4.2.1 Luminosity Functions

In order to reconstruct the luminosity functions of simulated galaxies from the projected photon data, we have to count, how many XRBs of which type and of which luminosity there are in each galaxy. Therefore, we make use of the package structure where photons belonging to a single simulation particle are stored in ascending order. This means that when the following photon energy is smaller than the current photon energy, a new photon package, i.e. the emission for a new XRB, has started. Note, that this approach may be inaccurate for low photon statistics where consecutive photons might be in ascending order by chance alone. We apply this scheme to all our galaxies and calculate the luminosity for each photon package in the energy band of  $0.5 - 8 \text{ keV}$  in order to be consistent with the observationally derived XLFs in the same band. We summarize our reconstruction process in figure 4.1, where we show SFR and  $M_*$  normalized cumulative luminosity functions of **Set 1**. Star-formation rate and stellar mass were derived from halo properties. The blue shaded area represents a density map for the underlying analytic model. It was created by randomly computing 10000 variants of the analytic model based on the model parameter uncertainties presented in table 1.2. Thus, the map emulates a measure of the expected model uncertainty. Contour levels were chosen to contain (from darker to lighter color) 68%, 90% and 95% of variants. We want to emphasize that we do not include any parameter scatter when creating the XRB emission through PHOX unit 1. The scatter of the magenta lines in 4.1 is purely a result of the stochastic process with which XRBs are assigned to stellar RE.

While the reconstructed LMXB luminosity functions are in good agreement with the analytic model and are within the estimated uncertainty for luminosities  $L > 5 \cdot 10^{36} \text{ erg s}^{-1}$ , we see gradual flattening of the reconstructed XLF below for  $L < 5 \cdot 10^{36} \text{ erg s}^{-1}$ . This results in a difference of 0.2–0.3 dex between the analytic model and the bulk of reconstructed LMXB LFs for lower luminosities. The scatter of the reconstructed LMXB LFs does not exceed 0.2 dex. This flattening is seen more clearly in the HMXB case where below  $L = 5 \cdot 10^{36} \text{ erg s}^{-1}$  the majority of LFs are flat. The resulting difference is hard to estimate given the generally strong scatter of more than an order of magnitude for the HMXB luminosity functions. The difference is at least 0.5 dex between the flat part of the bulk of HMXB LFs and the analytic model.

We suggest that the flattening of reconstructed LFs below luminosities of  $L = 5 \cdot 10^{36} \text{ erg s}^{-1}$  is connected to our photon generation, in particular to the spectrum discretization and to poor photon statistics. Multiplying equation (3.12) with observing time  $\tau_{\text{obs}} = 10^6$  and effective area  $A = 10^3$  and total luminosity  $L = 5 \cdot 10^{36} \text{ erg s}^{-1}$ , we get an expected number of photons of  $\sim 4.3$ . Naturally, lower total luminosities per XRB element would lead to less expected photons, which in our case should yield no photons for luminosities  $L < 1 \cdot 10^{36} \text{ erg s}^{-1}$ , keeping in mind that the photon simulation is also based on a stochastic approach.

Even though the strong scatter of the reconstructed HMXB XLFs is still in line with the model intrinsic uncertainties, the relation should be tighter for a well constrained star-formation proxy. By observing that most LFs have the expected analytic slope but are shifted along the y-axis, we infer that the SFR rate for those outliers is caused by differences between the halo SFR and our SFR estimate. One possible explanation would be that by assuming a constant formation efficiency  $\eta_{\text{HMXB}}$  we give more weight to older stellar REs while the halo SFR changed drastically during that time and no longer reflects the SFR implicated by  $\eta_{\text{HMXB}}$ . We also find that scaling relation recovered from the total HXMB luminosity appear to follow a non-linear relation (see figure 4.3) potentially influencing the linear scaling. Furthermore, we assumed a static fraction of massive stars implied by the IMF, which may influence the resulting SFR proxy in both directions. In section 4.2.2, we will show however, that this scatter can be entirely explained by small sample sizes.

#### 4.2.2 Mass & SFR relation

In this section we compute the total X-ray luminosity coming from XRBs for each galaxy in **Set 1** with lower  $\mathcal{D}_A$  and separated XRB component and compare them to their underlying observationally constrained scaling relations. The total X-ray luminosity of LMXBs is computed by summing over all LMXBs in the host galaxy which have a luminosity  $L > 5 \cdot 10^{37} \text{ erg s}^{-1}$ , following the same analysis in Zhang, Gilfanov, and Bogdán (2012). In figure 4.2 we show the total X-ray luminosity of LMXBs in each galaxy as a function of its stellar mass (red symbols). Additionally we show the expected linear scaling relation from Zhang, Gilfanov, and Bogdán (2012) as a black line together with the 1- $\sigma$  error bar shaded in grey. The green dots represent a sample of simulated XRB populations. In particular, the simulated XRB elements were created by randomly drawing stellar masses for the normalisation of the LMXB XLF, effectively producing populations of LMXB with different sizes  $N'_0$  (see section 3.2.1) which we sample according to their LF. From the stellar mass, we sampled the pseudo CDF in the same way as implemented in PHOX unit 1 and determined the total luminosity of the simulated population. Both the PHOX data set and the simulated one follow the expected relation with great accuracy. Only in the low stellar mass regimes we observe stronger scatter of the relation which is to be expected from lower sample sizes. The slight underestimation of the expected relation is due to the flattening of the recovered XLFs. In contrast to the neatly fitting relation for LMXBs stands the SFR

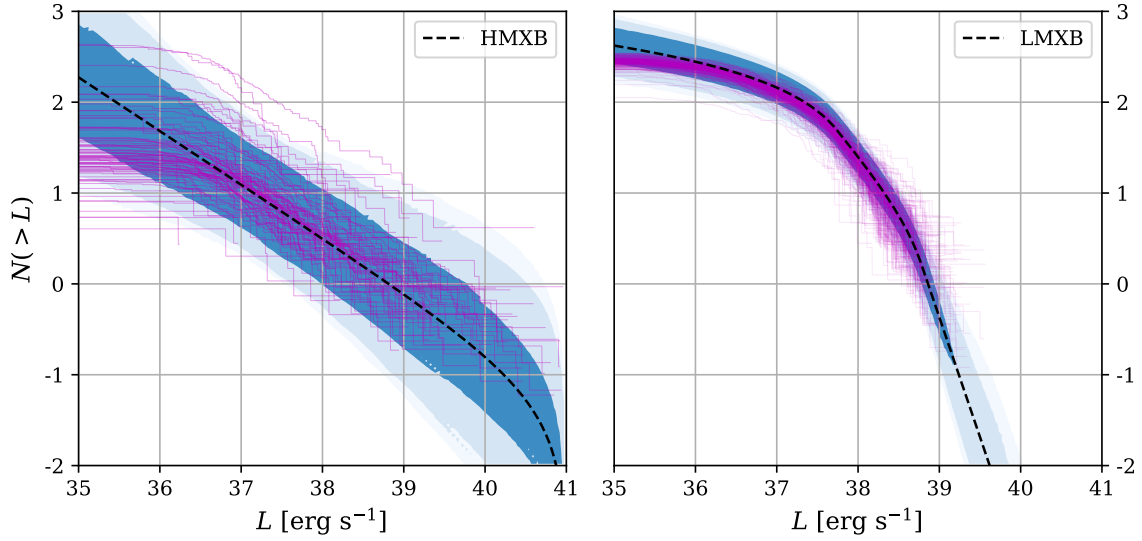


**Figure 4.1:** Reconstructed cumulative Luminosity Functions (*magenta*) using **Set 1**. The dashed black line indicates the analytic model for HMXBs (left panel) and LMXBs (right panel) using parameters from table 1.2, respectively. The LFs were normalized by SFR in the HMXB case and stellar mass in the LMXB case, both quantities derived from halo properties. The blue shaded area is a density map constructed from 10000 analytic XLF variants, from randomly assigning parameters with uncertainties given in table 1.2. From darker to lighter shades, contour levels were chosen to contain 68%, 90% and 95% of variants.

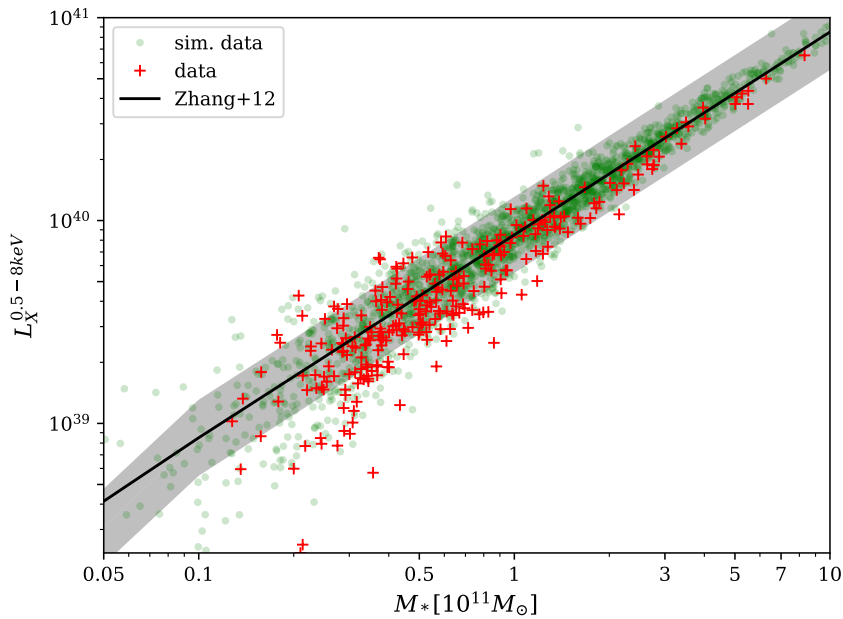


**Figure 4.2:** Mass relation of the total X-ray luminosity of a galaxy, originating only from LMXB emission. The total luminosity is calculated by summation of the 0.5–8 keV luminosity of each LMXB with  $L > 5 \cdot 10^{37} \text{ erg s}^{-1}$  in the galaxy. Depicted here, is **Set 1** (*red*) together with a sample of 2000 simulated XRB populations (*green*). The black line is the expected theoretical relation based on Zhang, Gilfanov, and Bogdán (2012). The shaded area (*grey*) is the  $1\text{-}\sigma$  error of the solid black line.

relation for the total HMXB luminosity of our **Set 1** in figure 4.3. The total luminosity is calculated from all HMXBs in the galaxy with  $L > 10^{36} \text{ erg s}^{-1}$ . Similar to the LMXB case, we show the empirical relation from Mineo et al. (2012a) as the solid black line with the  $1-\sigma$  level as the shaded area. The PHOX data is indicated by blue symbols and a set simulated HMXB populations, where we randomly choose SFRs for the HMXB XLF normalization, is displayed in green. We immediately notice that our data set is in strong tension to the scaling relation of Mineo et al. (2012a), seemingly following a non-linear SFR scaling. We calculated the scaling relation expected from integrating the underlying model in PHOX which is shown as the dash-dotted line and based the simulated green dots on the model in PHOX as well. For reference, we also show the scaling relation calculated for an alternative definition of the luminosity function for HMXBs from Mineo et al. (2012a) which appears to be in better agreement with the empirical relation. We observe that 1) the scaling relation expected from PHOX is clearly different from the empirical one in Mineo et al. (2012a), and 2) the simulated XRB population perfectly matches the distribution of the real data.

The latter clearly excludes badly constrained halo SFRs as a possible origin since both the PHOX and simulated data seem to show the same behaviour. We attribute this scatter to low number statistics. As Mineo et al. (2012a) put it themselves, the total X-ray luminosity is dominated by the low luminosity end of the LFs for small sample sizes. The apparent non-linear relation is thus only an artifact of preferentially sampling lower luminosities. The relation is much tighter and more symmetric for large SFRs. The reason that the stellar mass relation appears more constrained is due to the fact that for luminosities  $L > 10^{35} \text{ erg s}^{-1}$ , the cumulative XLF for LMXB has more than thrice the number of sources than the HMXB counterpart (see 4.1) thus also more than thrice the number of sampling points. And since the luminosity regimes, at which the HMXB XLF would be bigger than the LMXB one, are obscured through XLF flattening, the HMXB relation suffers from overall poor statistics. This also explains the behaviour seen in figure 4.1. Note, that the empirical SFR relation in Mineo et al. (2012a) does not experience the same scattering behaviour which is caused by them selecting only galaxies which have a sufficient number count above their detection limit, and overall good number statistics.

### 4.2.3 Spatial distribution of XRB emission

This section is dedicated to a crude spatial analysis of XRB emission. We will present a poster-child disk galaxy from **Set 1** and show the spatial conformance of the projected XRB component with star-formation regions, the gas surface-density and the stellar age distribution. The poster-child disk galaxy has FSUB-ID 13633 ( $F-13$ ), a SFR of  $8.34 M_{\odot} \text{ yr}^{-1}$  and stellar mass of  $2.73 \cdot 10^{11} M_{\odot}$ . In figure 4.4 we show the raw LMXB (red 2D histograms) and HMXB (green 2D histograms) photon count of  $F-13$  where we chose arbitrary contour levels for illustrative purposes. Darker colours mean a higher photon count. The LMXB emission is concentrated at the center of  $F-13$  with some patches towards the outskirts, though with lower photon count. The HMXB emission is encircling the center and is more continuous. In figure 4.5 we show both XRB emission contours in green for HMXBs and red for LMXBs, together with the star-forming regions where darker colors correspond to regions of low star-formation and orange-ellow colours to regions of high star-formation. We note, that the HMXB component nicely traces the SFR region which is as expected. The same can be said for figure 4.6 where we show that the HMXB component also traces the gas surface density. That is also as expected since the gas surface density is connected to star-formation via the Schmidt-Kennicutt relation Kennicutt (1998) and Schmidt (1959). In figure 4.7 we show the stellar age distribution of  $F-13$ , with HMXBs tracing the young stellar component and LMXB tracing the older stellar component in the galactic bulge. This shows that our modelling of the XRB emission in PHOX produces satisfying results regarding spatial

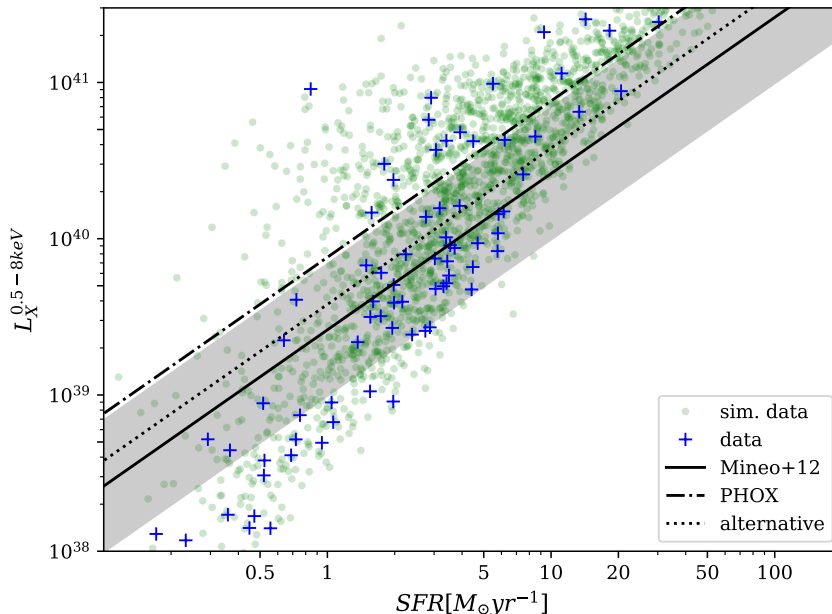


**Figure 4.3:** SFR relation of the total X-ray luminosity of a galaxy originating only from HMXB emission. The total luminosity is calculated by summation of the 0.5 – 8 keV luminosity of each LMXB with  $L > 10^{36}$  erg s $^{-1}$  in the galaxy. Depicted here, is **Set 1** (*blue*) together with a sample of 2000 simulated galaxies (*green*). The simulated galaxies were created by randomly drawing SFRs for the normalisation of the HMXB XLF. The black line is the expected theoretical relation based on Mineo et al. (2012a). The shaded area (*grey*) is the 1- $\sigma$  error of the solid black line. The dash-dotted line is the

relations.

### 4.3 Ratio of XRB, AGN and gas emission

In this section we present our analysis on the emission ratio of XRBs relative to other emission models, namely gas and AGN emission. For section 4.3.1 we use data of **Set 3** with separated XRB component and shifted toward smaller  $\mathcal{D}_A$ . For the remaining sections we use **Set 2** where we keep  $\mathcal{D}_{A, fid}$ , computed by the snapshot redshift of  $z = 0.066$ , and combine the XRB emission from both types. We compute the emission ratio in section 4.3.2 and 4.3.3 as

$$r = \frac{c_{\text{XRB}} + c_i}{c_i}, \quad (4.1)$$

with  $c_i$  as the photon count of the component against which we compared. We use it to determine, how large the fraction of galaxies, dominated by XRB emission, is. Values of  $r \sim 1$  correspond to the secondary component  $c_i$  being dominant, and  $r \sim 2$  corresponds to equal emission strength. For every ratio  $r > 2$ , we consider the primary component, in our case XRBs, to be dominant.

#### 4.3.1 LXB vs HXB

In figure 4.8 we compare the emission of the LMXBs to the emission of HMXBs for the spectral range of 0.1 – 50 keV. The halo SFR derived from simulation data is in colors from low SFR in blue to high SFR in red for each galaxy. We observe the expected trend

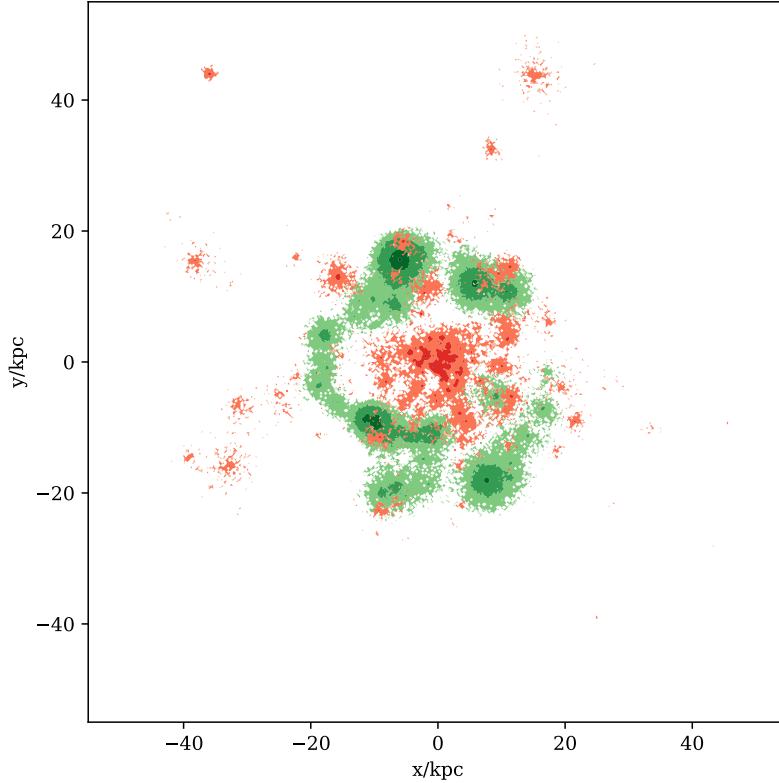


**Figure 4.4:** Projected XRB emission of a poster-child LTG of our galaxy sample. It is shown face-on and has FSUB-ID 13633, a SFR of  $8.34 M_{\odot} \text{yr}^{-1}$  and stellar mass  $2.73 \cdot 10^{11} M_{\odot}$ . Coordinates are in physical units. Photon energies are in the range  $0.1 - 50 \text{keV}$ . Red shades correspond to LMXB emission, blue shades to HMXB. Darker shades correspond to a higher photon count. The contour levels were chosen arbitrarily for illustrative purposes.

of HMXB emission increasing with SFR, with some low SFR galaxies having a too strong HMXB emission, and some high SFR galaxies having too weak HMXB emission. Both is connected to small sample size argument from section 4.2.2. Galaxies with no star-formation are plotted with left-pointing arrows at  $\log c_{HXB} = 0.9$ . The  $\log c_{LXB}$  range is in agreement with the linear stellar mass scaling presented in figure 4.2. Of our sample,  $\approx 81\%$  of galaxies have a ratio  $c_{HXB}/c_{LXB} < 1/2$  and are thus dominated by LMXB emission, which is in agreement with the statement, that at  $z \sim 0$ , galactic XRB emission is mostly coming from LMXB sources [Madau and Fragos (2017) and Fragos, Lehmer, Tremmel, et al. (2013)]. The HMXB emission is dominant ( $c_{HXB}/c_{LXB} > 2$ ) in  $\approx 12\%$  of galaxies.

### 4.3.2 Gas vs. XRB

From this point on we use **Set 2** for our analysis with  $\mathcal{D}_A$  unchanged. We follow a similar approach as in Biffi, Dolag, and Merloni (2018) to quantify the relative strength of the XRB component using the ratio from equation (4.1). In figure 4.9 we show the histograms of the fraction of galaxies as a function of the photon count ratio  $r$ , normalized to the number of galaxies in each spectral band (solid lines with diamond symbols). We find that in the hard X-ray band, XRB emission is dominant over the gas emission in  $80 - 90\%$  of cases. The strong increase in the last ratio bin is caused by placing all galaxies with no photons coming from gas emission into that bin. In the soft X-ray band (red), the XRB component is dominant in  $\approx 30 - 40\%$  of galaxies. Both results are connected to the underlying spectral models: the

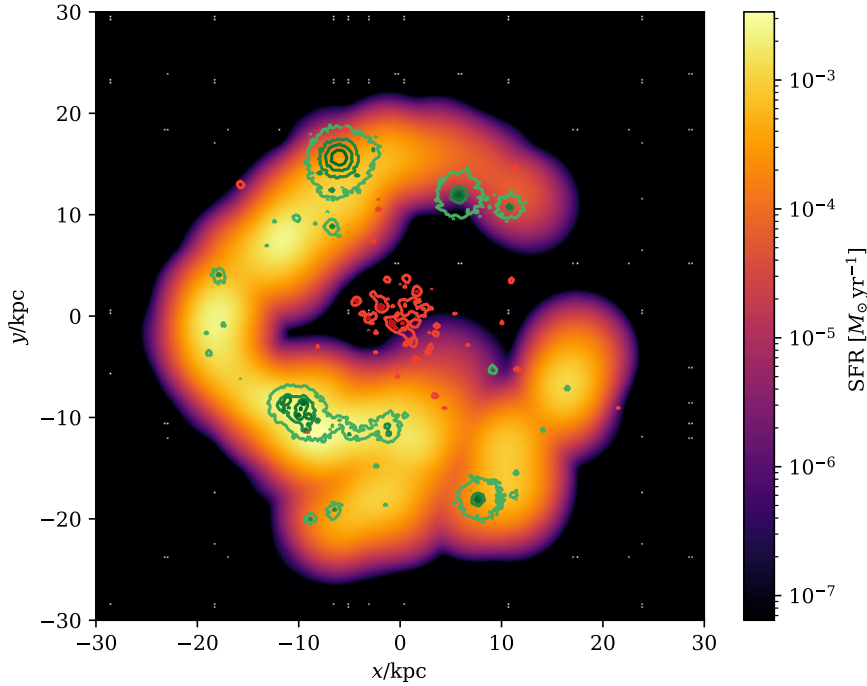


**Figure 4.5:** Star-formation map of galaxy FID-13633 in units of  $M_{\odot} \text{yr}^{-1}$ . Overlaid is the projected XRB emission of HMXB (*green*) and LMXB (*red*). The contour levels correspond to photon counts of 15, 70, 140 and 300 from light to dark. Some of the white pixels seen in the outskirts are artifacts of the smoothing. Distances are in physical units. Photon energies are in the range 0.1–50keV. Image created with `pynbody` v1.0.2 [Pontzen et al. (2013)].

thermal Bremsstrahlung emitted by hot gas peaks in the soft X-ray band for typical galactic gas temperatures of  $10^6$  K and quickly declines for photon energies  $> 1$  keV, whereas the XRB power-law spectrum has its peak, though lower than the gas emission peak, in the soft band (with absorption) and also extends into the hard X-ray band. In the broad X-ray band (green) we essentially follow the soft band distribution with a slightly lower fraction in the first ratio bin. Since we have additional XRB emission from the hard X-ray band, we expect less galaxies in that bin than for the soft band. The distribution of the combined band quickly approaches the soft band distribution for higher ratios since an increase in photon numbers in XRBs is more likely to happen in the soft band because of the underlying power-law.

### 4.3.3 AGN vs. XRB

Similar to section 4.3.2, we analyse the emission ratio between the XRB and AGN component in figure 4.10. In the soft band, approximately 50 – 60% of galaxies have a dominant XRB component. This is to be expected, since the soft emission of the AGN power-law model is suppressed by a double absorption coefficient, one constant foreground and the other intrinsic, resulting in a lot of galaxies with no soft AGN photons. In the hard X-ray band, only 10–20% of galaxies have a dominant XRB component, and if so, mostly for  $r > 50$ . This means that a quiescent AGN is required, in order for the XRB component to become dominant in the hard X-ray band. The behaviour of the broad band can again be understood from the fact that XRBs have their peak emission in the soft band, which increases the total photon count.

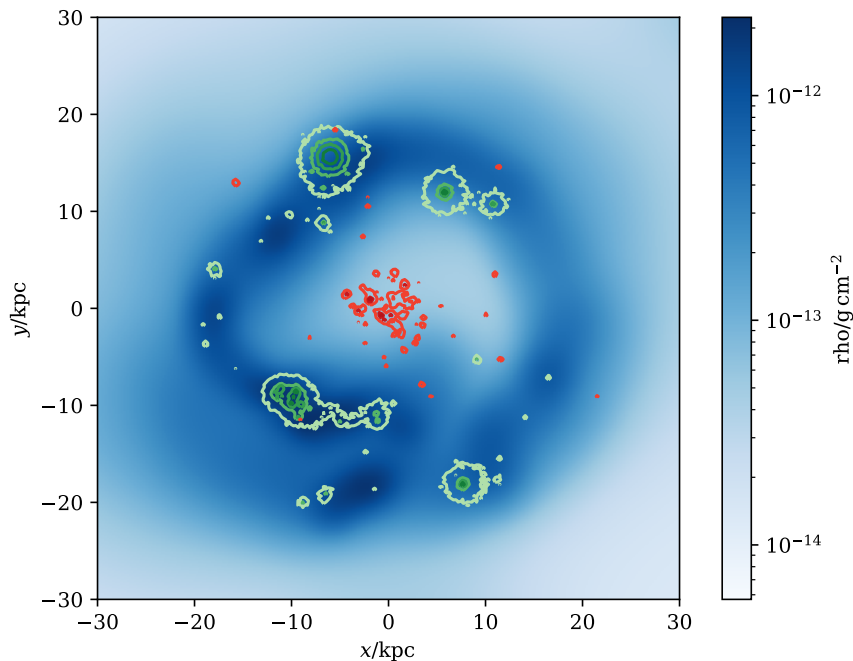


**Figure 4.6:** Gas surface-density map of galaxy FID-13633. Overlaid is the projected XRB emission of HMXB (*green*) and LMXB (*red*). The contour levels correspond to photon counts of 15, 70, 140 and 300 from light to dark. Distances are in physical units. Photon energies are in the range 0.1 – 50keV. Image created with `pynbody` v1.0.2 [Pontzen et al. (2013)].

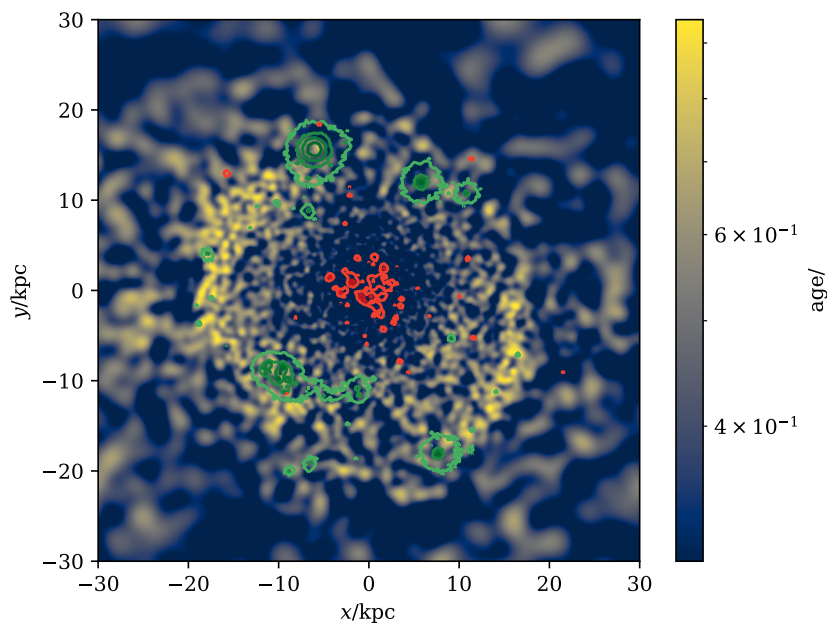


**Figure 4.7:** Stellar age map of galaxy FID-13633 given as the scale factor. Darker colors correspond to older regions. Overlaid is the projected XRB emission of HMXB (*green*) and LMXB (*red*). The contour levels correspond to photon counts of 15, 70, 140 and 300 from light to dark. Distances are in physical units. Photon energies are in the range 0.1 – 50keV. Image created with `pynbody` v1.0.2 [Pontzen et al. (2013)].

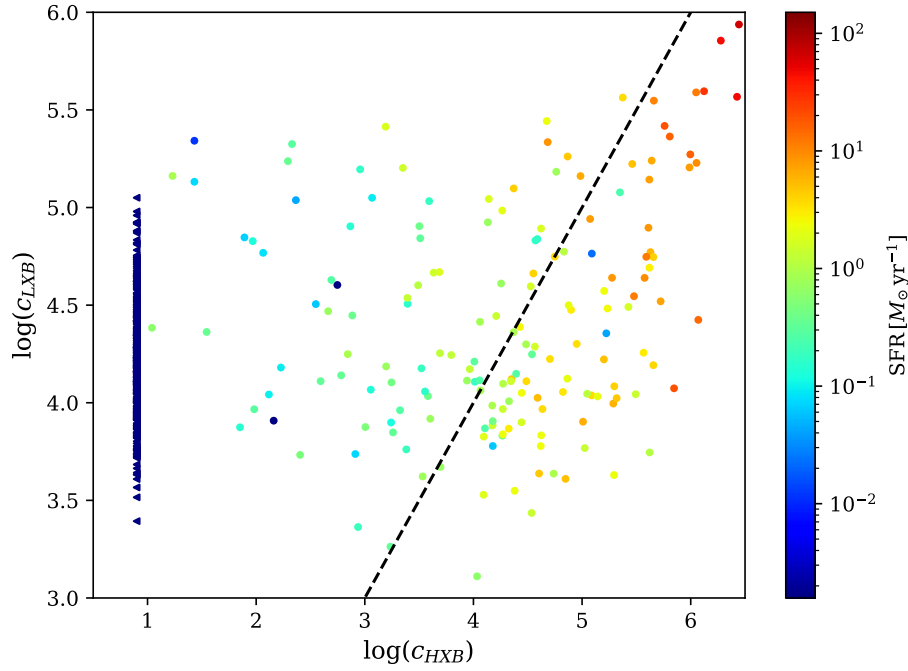


**Figure 4.8:** Photon counts of LMXB component as a function of HMXB photon counts for all galaxies in **Set 1** with reduced  $\mathcal{D}_A$ . The dashed black line is the 1:1 ratio. Colors are halo SFRs of the galaxies derived from simulation data. Left pointing arrows aligned at the vertical line  $\log c_{HXB} = 0.9$  indicate galaxies with no HMXB photons and SFR = 0.

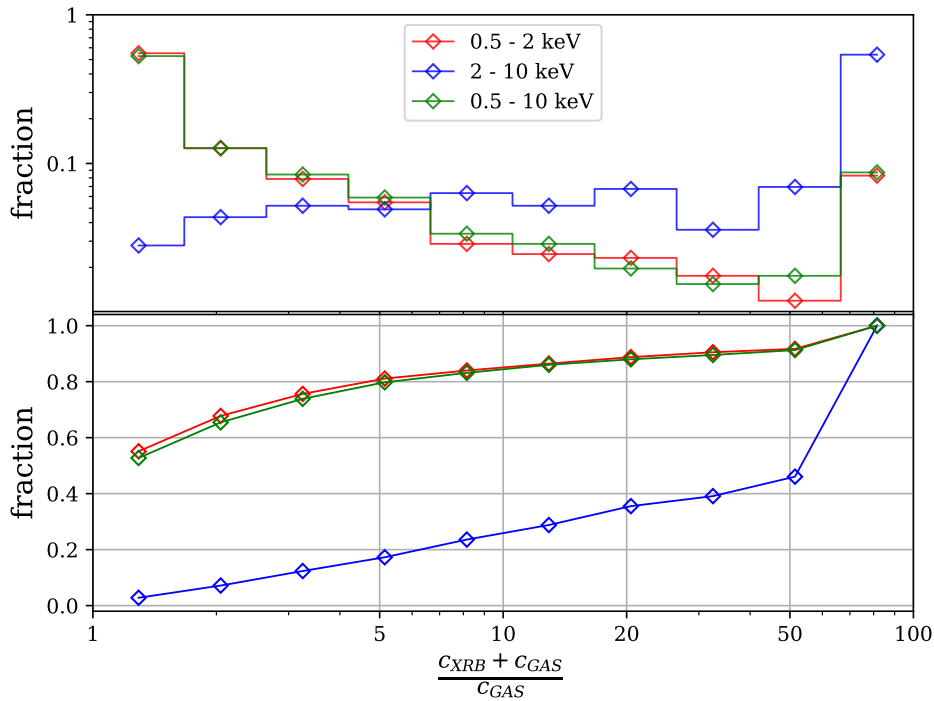


**Figure 4.9:** Fraction of galaxies in **Set 2** as a function of the count ratio  $r$  between XRB and GAS emission. Colors correspond to different emission bands in both panels. The lower panel shows the cumulative version of the top panel histogram. Galaxies with no photons coming from the gas component were placed into the highest ratio bin.

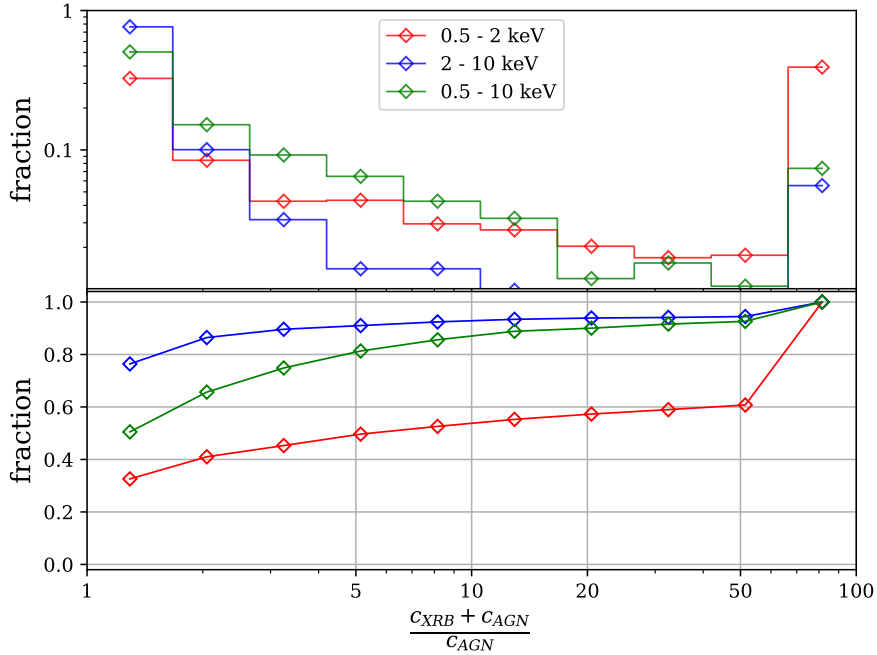


Figure 4.10: Same as in figure 4.9 but for the AGN component.

## 4.4 Average galaxy spectra

In this section we present our results regarding the average spectra of galaxies and the relative contribution of the three emission components, based on various galactic properties. In particular, we show the effects of selecting by galaxy type, stellar mass and star-formation on the average spectrum. Spectra will be given as normalized photons counts meaning that the spectrum of each individual galaxy is normalized its total photon count. We do not take the observing time  $\tau_{\text{obs}}$  and effective area  $A$  into account since they equal for every galaxy and do not affecting the relative contribution of the emission components. Average spectra are then calculated from the normalized height of each photon energy bin across all galaxies in the sample. With that approach, we make sure that all galaxies can be fairly compared among each other. This also guarantees that the sum of all energy bins of the resulting average spectrum will be equal to one. Changes in the relative contribution can thus be more easily identified by the relative height of each component.

### 4.4.1 Hubble-type Correlation

We use galaxies from **Set 1** with combined XRB component and unaltered angular distance  $\mathcal{D}_A$  and produce the average spectra for late-type and early-type subsamples in the energy range of 0.3 – 10 keV, both of which can be seen in the upper panel of figure 4.11 and 4.12 respectively. The lower panel of each figure shows the relative contribution of the respective component to the total spectrum. Spikes in the gas spectrum are caused by emission lines of contributing metals. The XRB and gas component have similar relative contributions in the soft band of 40% – 60%, with XRBs peaking at  $\sim 0.5$  keV and  $\sim 1.4$  keV, and gas emission peaking at  $\sim 0.8$  keV. The AGN component becomes the dominant contributor at energies higher than  $\sim 1.8$  keV. Our observations complement the results obtained in section 4.3 and are equally true for the LTG and ETG case, since they appear to be congruent. We expected more significant differences especially in the XRB part. But keeping in mind our results from previous sections, the effects of star-formation on the HMXB contribution are

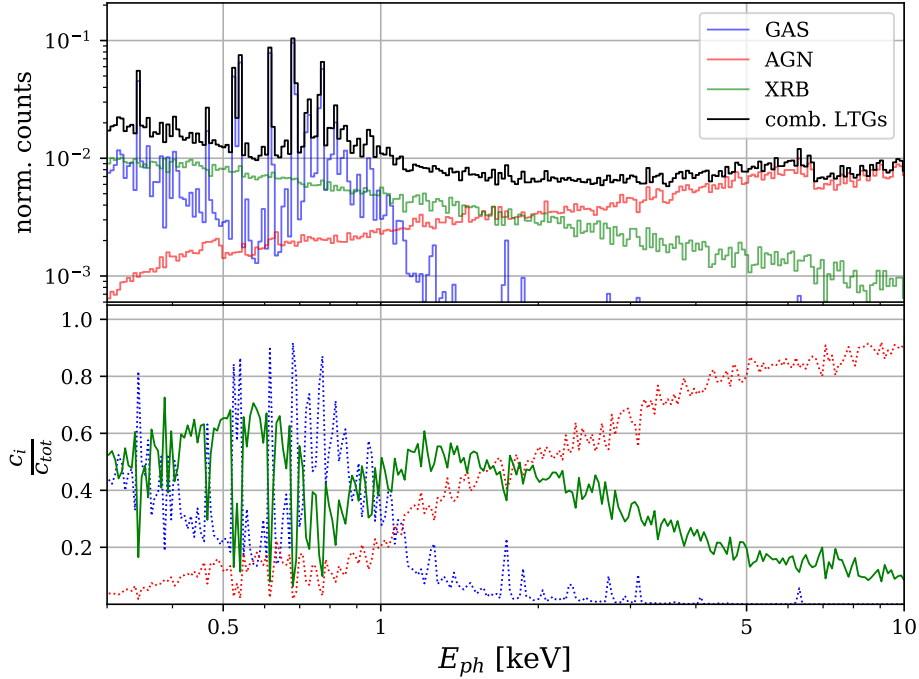


**Figure 4.11:** *Top panel:* Cumulative average photon counts per energy bin of 135 LTGs (black). Prior to taking the average photon count per energy bin, each spectrum was normalized by the total photon count, which is the sum of each of the constituents (GAS: blue, AGN: red, XRB: green). This gives equal weight to each contributing galaxy. *Lower panel:* Relative contribution of the individual components to the total spectrum, with the XRB contribution being solid for highlighting.

easily suppressed by averaging over a large SFR range, especially with the large scatter we encounter in our SFR scaling relation.

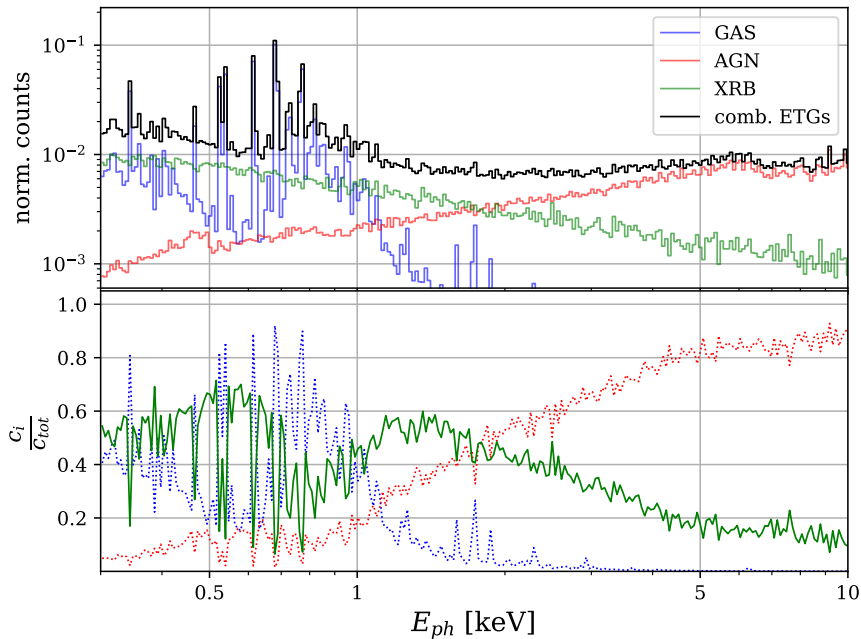


**Figure 4.12:** Same as figure 4.11, but for the 173 ETGs in our sample.

If we omit AGN emission, our relative contributions for the XRB and gas component are

very similar to a study performed by Wik et al. (2014) on the starburst galaxy *NGC 253* (see their figure 14). They based their analysis on the galactic X-ray model of Persic and Rephaeli (2003; 2002) which uses more sophisticated estimates for the hot gas and XRB component. In fact, this results in a XRB component which is 10% weaker in the case of *NGC 253* than for our prediction. Given our simple model, however, we appreciate the achieved similarities.

#### 4.4.2 Stellar Mass and Star-formation Binning

In order to study the dependence of the XRB binary contribution on galactic properties, we use **Set 2** and divide it into bins of roughly equal size for the respective property. In principle, any property can be studied and with an arbitrary amount of property bins. We chose stellar mass and star-formation rate as a showcase out of a multitude of possible studies since they are related to the expected emission of the XRB component. The specific stellar mass and SFR cuts are shown as dashed lines in figure 4.13, where we also illustrate the SFR –  $M_*$  relation of **Set 2**. The colour code is given by the count ratio  $c_{XB}/c_G$  between the XRB and gas component in the energy range 0.1 – 50 keV, with blue corresponding to an excess in gas emission and red to an excess in XRB emission. We placed every galaxy with zero star-formation on  $\log(\text{SFR}) = -4$  for illustrative purposes.

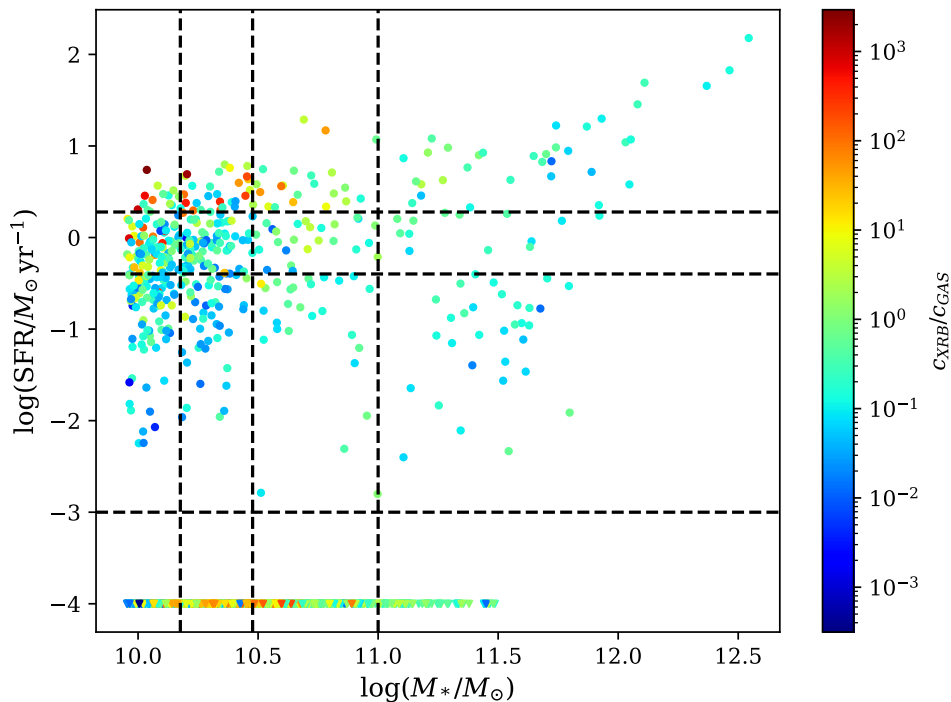


**Figure 4.13:** SFR –  $M_*$  relation of **Set 2** colour coded by the emission ratio  $c_{XB}/c_G$  between the XRB and gas component in the energy range 0.1 – 50 keV. The dashed lines indicate the mass and SFR cuts used for the property binning in figure 4.14 and 4.15. Galaxies with zero star-formation were placed at  $\log(\text{SFR}) = -4$ .

In figure 4.14 we show the average spectra of the four chosen stellar mass bins. The number of galaxies  $N_g$  per bin as well as the cuts defining the bin are given in the gray boxes at the top of the respective panel. We note, that the AGN component does not experience any significant change across the different stellar mass bins. Because of that and the unreliable contributions below 0.3 keV due to absorption, we will mainly investigate the soft bands up to 2 keV. The lowest mass bin shows a relative XRB contribution of 30 – 40% in the soft band

above 0.3 keV with the gas contribution at 60 – 70%. For the intermediate mass bins, the the XRB and gas contribution is equal at 40 – 50% in the soft band, which is comparable to the average contribution from section 4.4.1, and at the highest mass bin the XRB contribution drops to 20 – 30% with the average gas spectra broadening up to energies of 2 keV. This behaviour is expected since with an increase in stellar mass, also the virial mass is expected to increase resulting in higher gas temperatures due to a deeper potential. This is also seen in the color gradient of the highest mass bin of figure 4.13 which shows no dominant XRB component for any of the galaxies in that bin. Similarly, the increase in gas contribution for the lowest mass bin is also seen in 4.13, though the average gas spectra is not as broad as for the highest mass bin. This indicates that for the lowest mass bin, the XRB component is comparatively weak, which we attribute to the scatter of the scaling relations of LMXBs and HMXBs at low stellar masses and SFRs towards lower luminosities. The two intermediate mass bins are similar to each other, since they contain masses of roughly the same order of magnitude which makes little difference for the XRB scaling relations.

In figure 4.15 we show the the average spectra for the four chosen SFR bins. The figure layout is the same as for 4.14. Note, that it was not possible to create equal-sized SFR bins due to the large number of zero star-formation galaxies. Instead we tried to have equal number of galaxies for the other three remaining SFR bins. Immediately, we notice a non-monotonous development of the XRB contribution with increasing SFR bins. For the zero SFR bin and for the highest SFR bin, the XRB contributions are again similar to the values of 4.4.1 around 40 – 50% in the soft band above 0.3 keV. The highest SFR bin additionally has a broader gas emission profile indicating a significant contribution from massive halos. Furthermore, the hard XRB spectrum show  $\sim 10\%$  less contribution in the highest SFR bin compared to the lowest, which comes from the slightly softer HMXB spectrum ( $\Gamma_H > \Gamma_L$ ). Indeed, we take from figure 4.13 that both the lowest and highest SFR bin contain galaxies of a broad range of count ratios  $c_{XB}/c_G$  with the highest bin additionally containing the most massive ones. The XRB contribution in the low SFR bin (top right panel of figure 4.15) is below 20% in the whole displayed spectral range. This has mainly two reasons: 1) the HMXB content is low from the SFR scaling and 2) the bin contains massive galaxies. The latter can also be seen in figure 4.16, where we show the virial temperature distribution for the different SFR bins. We normalized the distribution by the number of galaxies in each bin to have a better comparison between the SFR bins. We see that the temperatures for the intermediate SFR bins are similar with a secondary peak for high temperatures in the low SFR case. The slightly increased SFR for the intermediate bin causes an average increase to the HMXB content and thus a larger XRB contribution in the soft band compared to the low SFR bin. Interestingly, the zero SFR bin has on average a emission ratio  $c_{XB}/c_G > 1$ , from which we infer, given the absence of HMXB emission (see figure 4.8), that the gas content of those galaxies is significantly lower than for star-forming galaxies with similar masses. The exact reason is unclear, but we suggest some gas stripping event or feedback mechanism from the cosmological simulation being responsible.

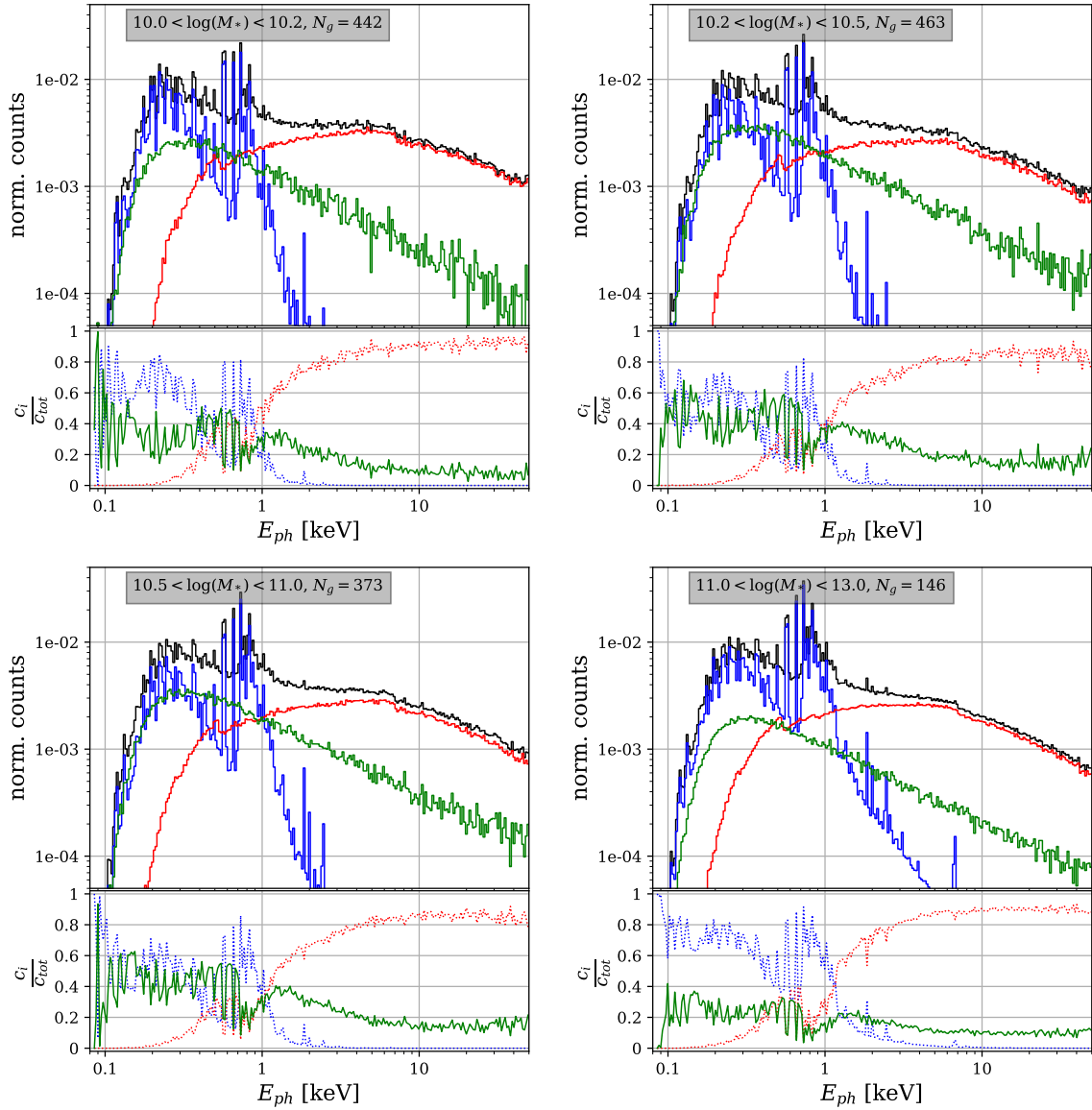


**Figure 4.14:** Cumulative average photon counts per energy bin, split by stellar mass, in the upper panels of each quadrant. Prior to taking the average photon count per energy bin, each spectrum was normalized by the total photon count, which is the sum of each of the constituents (GAS: *blue*, AGN: *red*, XRB: *green*). This gives equal weight to each contributing galaxy. Lower panels in each quadrant show the relative contribution of each component to the total spectrum. Mass splits were chosen such that each mass bin is roughly equal sized (indicated by  $N_g$ ). The grey boxes indicate the limits of the chosen mass bin.

## 4.5 Estimates of the Cosmic X-ray background

In this section we will use the three components included in PHOX to model the cosmic X-ray background of *Magneticum Box2*. For that we construct a lightcone through the simulation data and analyze the collective emission of the different redshift slices. Lightcones are constructed by taking a certain line of sight (l.o.s.) direction from  $z = 0$  and tracing it through the simulation snapshots under a certain viewing angle and taking into account the distribution of particle inside the snapshot. We sort the particles into discrete redshift bins based on the redshift coverage and volume of the individual snapshots. From the l.o.s

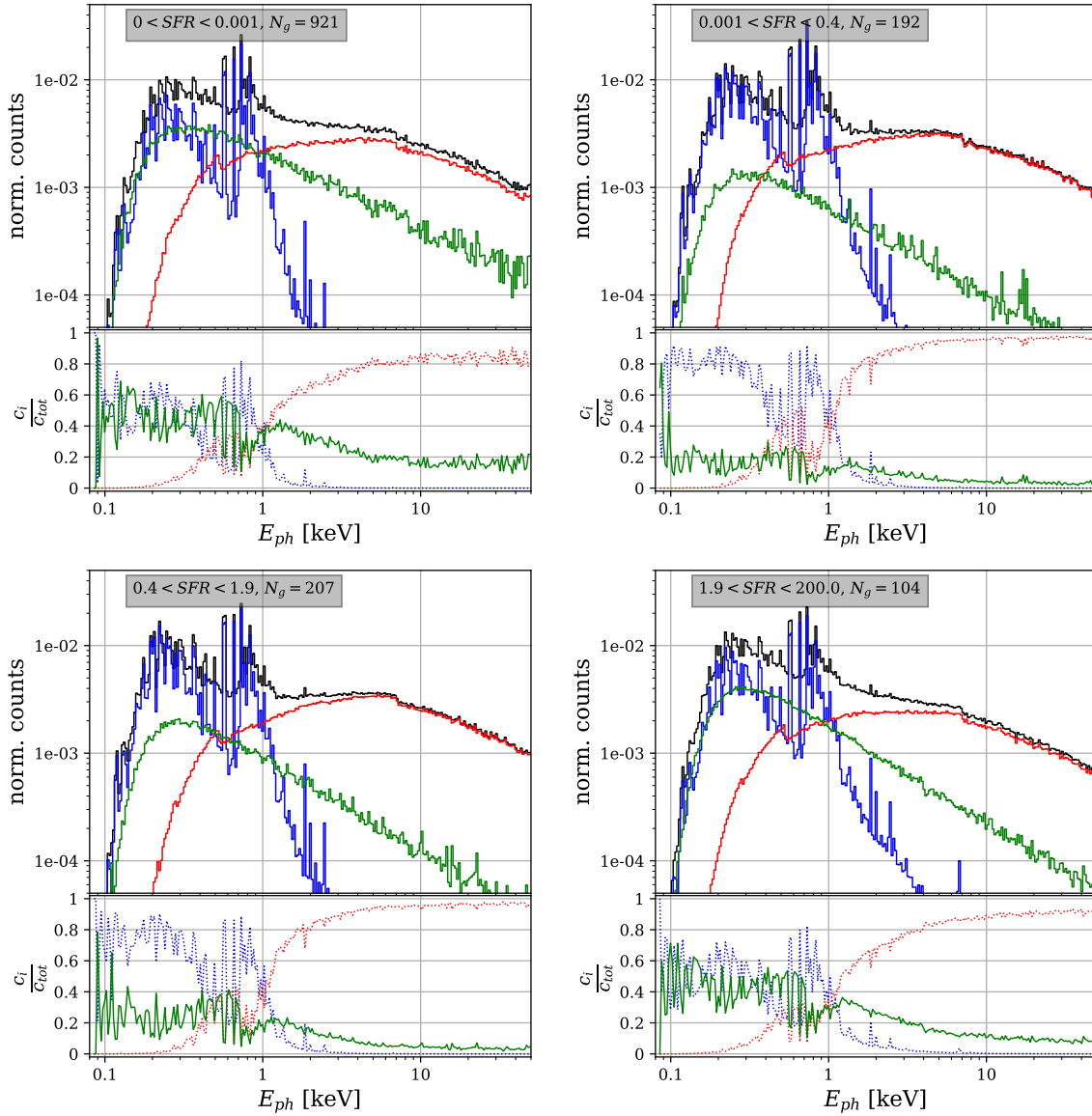


**Figure 4.15:** Cumulative average photon counts per energy bin, split by SFR, in the upper panels of each quadrant. Prior to taking the average photon count per energy bin, each spectrum was normalized by the total photon count, which is the sum of each of the constituents (GAS: *blue*, AGN: *red*, XRB: *green*). This gives equal weight to each contributing galaxy. Lower panels in each quadrant show the relative contribution of each component to the total spectrum. SFR splits were chosen such that each SFR bin is roughly equal sized (indicated by  $N_g$ ). The grey boxes indicate the limits of the chosen SFR bin.

direction and angle we calculate what particles would be in our view for a specific redshift bin and geometrically stack them onto the previous bin, essentially approximating a real observation of continuous redshift with finitely many thick slices obtained from simulation snapshots. In particular, we trace a lightcone through *Magneticum Box2* data from  $z \gtrsim 0$  to  $z \sim 2$  and viewing angle of 5 deg in right-ascension and declination. We assumed a column density  $N_H = 10^{20} \text{ cm}^{-2}$ , observing time  $\tau_{\text{obs},fid} = 10^6 \text{ s}$  and effective area  $A_{fid} = 1000 \text{ cm}^2$ . From the construction we also obtain information about virial mass and virial radius (in units of the viewing angle) of halos in our field of view. We apply PHOX unit 2 with a suitable patch for lightcones, accounting for the reordering of particle data within the redshift slices of the lightcone to generate appropriate photon projections. The resulting raw image of the

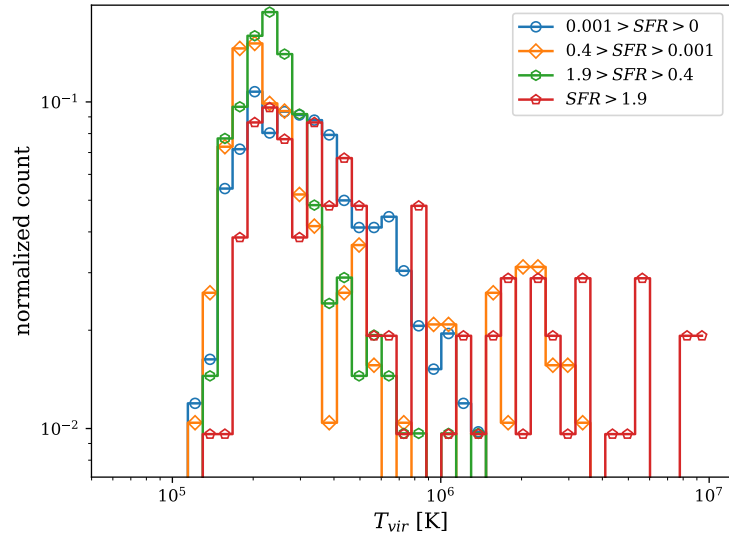


**Figure 4.16:** Virial temperature distribution for each of the SFR splits from figure 4.15 indicated by different colors. The distributions have been normalized by the number of galaxies in each SFR bin, in order to see differences in the width of the distribution. Notice the  $\log - \log$  scale of the image. The symbols indicate the temperature bin centers and serve as a viewing aid.

lightcone in the energy range of 0.1 – 50 keV is shown in figure 4.17

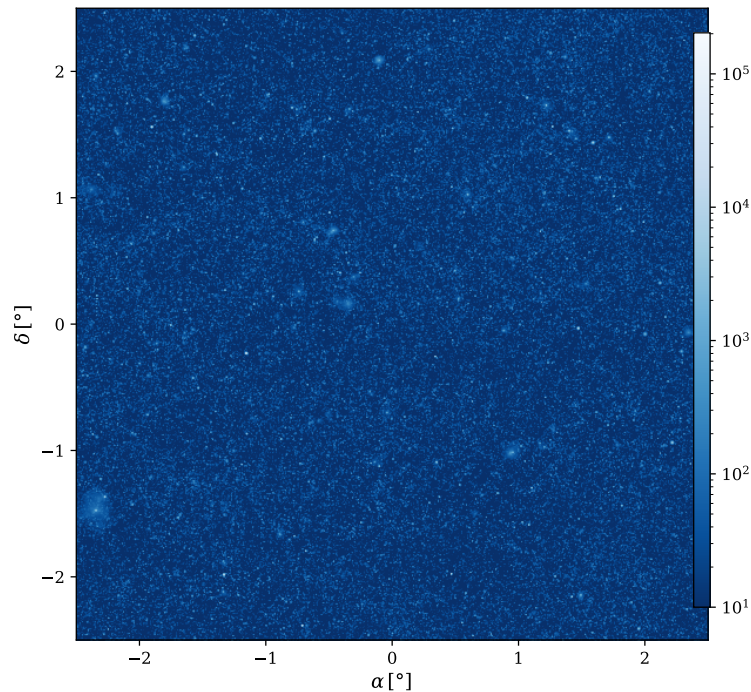


**Figure 4.17:** Full view of the  $5 \text{ deg}^2$  lightcone produced from *Magneticum*, *Box2* with photon energy range of 0.1 – 50 keV using gas, AGN and XRB emission. The color-bar indicates photon counts in each pixel. One pixel corresponds to  $0.00244 \text{ deg}^2$ .

### 4.5.1 Background & Source removal

The raw X-ray spectrum of the lightcone in the 0.3–10 keV band is shown in figure 4.18 where we compare to the extra-galactic X-ray background (CXB) measurements from Cappelluti et al. (2017), specifically their power law models from removing detected X-ray sources (uCXB, for unresolved CXB) and from additionally removing faint galaxies with magnitude  $i_{AB} \sim 27 - 28$  (nsCXB, for non-source CXB) in the spectral range of 0.3–7 keV. We do not take into account their galactic thermal X-ray models considering that we do not model a galactic foreground emission for our lightcone view. We find that neither of the two considered power law models are in good agreement with the full lightcone spectrum. The disagreement can have a multitude of reasons, from modelling differences especially at low energies as well as the considered redshift depth, for instance. A more in depth comparison would be necessary in the future. Nevertheless, our analysis shows that AGN are the largest contributors to the lightcone spectrum, which is as expected from AGN synthesis models [see e.g. Ueda et al. (2014) and Gilli et al. (2007)]. The XRB component is completely negligible with a peak contribution of  $< 4\%$  at .3 keV.

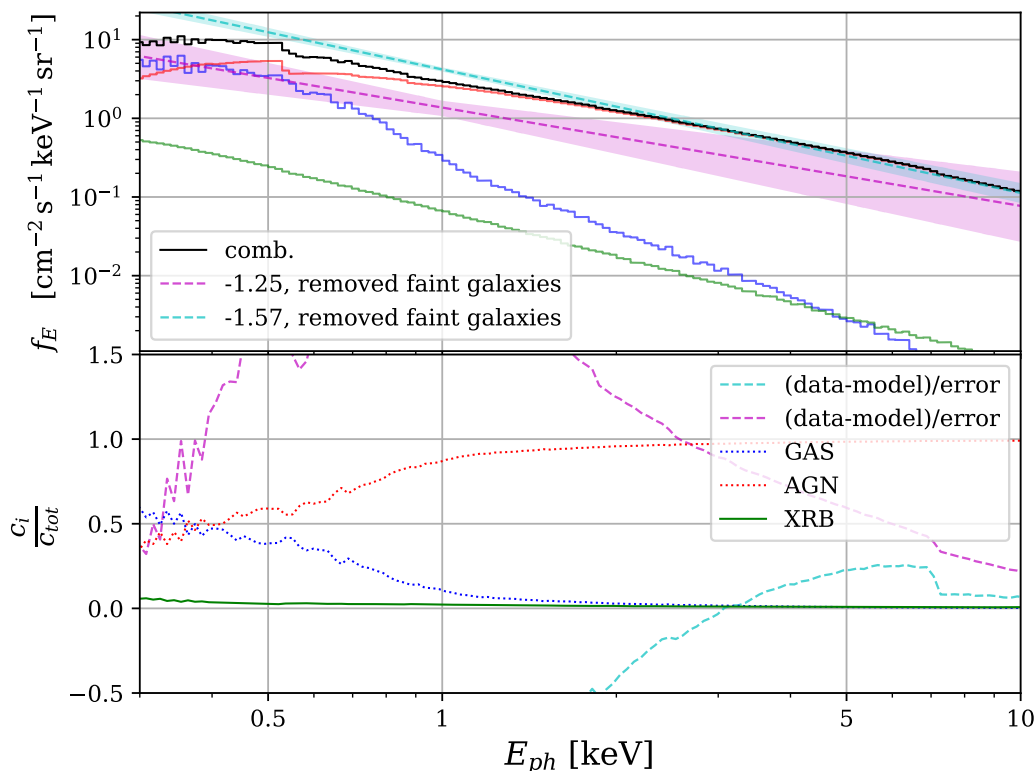


**Figure 4.18:** Spectrum of the full lightcone view (figure 4.17) in the energy range 0.3–10 keV. Included are the power-laws of Cappelluti et al. (2017) for the uCXB (*cyan*) and the nsCXB (*magenta*) with their  $1-\sigma$  uncertainty (shaded area) in the top panel. The lower panel shows the relative contribution of each component to the total spectrum. Included in the lower panel is also the absolute deviation of the power law models from the total spectrum normalized to the error of the power law model. By error we specifically mean the absolute difference between the upper and lower  $1-\sigma$  bounds.

Since we know the position, angular radius and their mass of halos in our field of view, we can mask the emission of these halos to better match the approach used in Cappelluti et al. (2017). First we determine the position and virial radius of the halos in our view and subsequently remove all photons from every redshift slice coming from the region of the lightcone encircled by the virial radius of that halo. In this way, we emulate the masking of these sources from

an observational perspective using telescope data. The resulting masked lightcone view for halos more massive than  $2 \cdot 10^{13} M_{\odot}$  can be seen in figure 4.19. We take the spectrum of

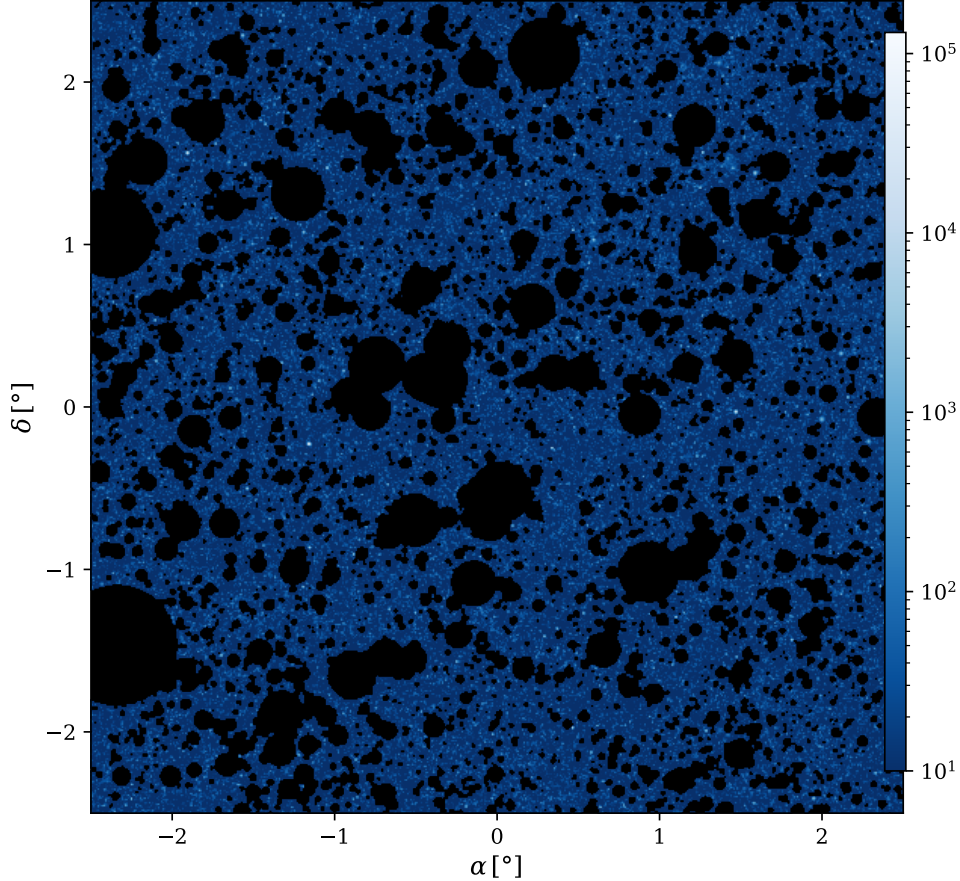


**Figure 4.19:** Same as in figure 4.17. The black patches in the field of view correspond to masked halos of a specific mass. In this case, all photons within the virial radius  $R_{vir}$  of a halo with virial mass  $M_{vir} > 2 \cdot 10^{13} M_{\odot}$  were removed from each redshift slice of the lightcone.

the masked lightcone and compare it to the same power-laws as for figure 4.18. Note, that the mass cut for the halo masks was chosen such that the normalization of our spectrum at 1 keV is the same as for the power-law normalization of the nsCXB from Cappelluti et al. (2017). Nevertheless, we find excellent agreement between the spectrum and the power-law model for the nsCXB, especially for the power law slope. The absolute deviation of the uCXB is well outside our chosen range due to a four time higher normalization. The relative contribution of the individual components remains almost unchanged, with only the gas component contributing  $\lesssim 5\%$  less, which is expected, since we specifically remove massive halos with hot gaseous components.

#### 4.5.2 Redshift dependence of relative XRB contribution

As an additional study, the redshift dependence of the three different emission components will be analyzed. In particular, the relative contribution of each component will be extracted

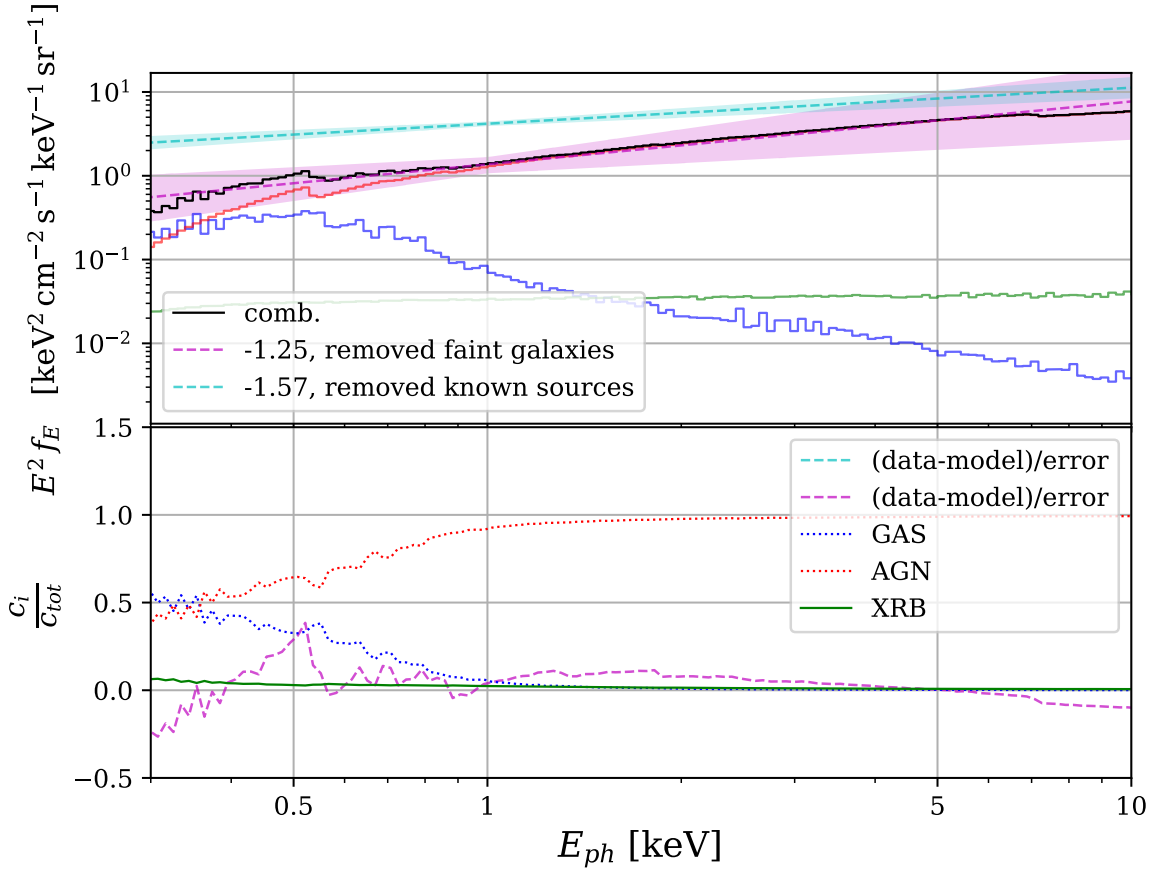


**Figure 4.20:** Spectrum of the masked lightcone view (figure 4.19) in the energy range 0.3 – 10 keV. Included are the power-laws of Cappelluti et al. (2017) for the uCXB (cyan) and the nsCXB (magenta) with their  $1-\sigma$  uncertainty (shaded area) in the top panel. The lower panel shows the relative contribution of each component to the total spectrum. Included in the lower panel is also the absolute deviation of the power law models from the total spectrum normalized to the error of the power law model. By error we specifically mean the absolute difference between the upper and lower  $1-\sigma$  bounds.

for each redshift slice separately which we show in figure 4.21. The XRB binary component has its strongest contribution for low redshifts with  $\lesssim 10\%$  in the soft band up to 1 keV and  $\lesssim 5\%$  in the hard X-ray band. The strongest contribution in the soft band up to 1 keV for low redshifts comes from the gas component with 50 – 60%. For increasing redshifts, the contribution of XRBs and gas declines in the soft-band due to more of the AGN emission being redshifted into the soft energy regimes. Gas contribution shrinks to  $< 20\%$  for the highest redshift slices, while XRB contribution notably decreases in the hard band and retains a  $\lesssim 5\%$  contribution in for very low photon energies. Independent of redshift, the AGN component always dominates the hard X-ray band and increases its contribution in the soft band from 20 – 30% at the lowest redshift to  $> 80\%$  at the highest redshift. All of this is to be expected, since the AGN population size should increase with an increasing redshift and dominate the X-ray emission with their large luminosities. Note, that we do not show the redshift dependence by accounting for the frame of reference for the observed photon energies. This is due to the fact, that we produce photons down to 0.05 keV for which we would have to account for our assumed absorption coefficient. We have to revisit the proper analysis of this issue in a future study due to time constraints.

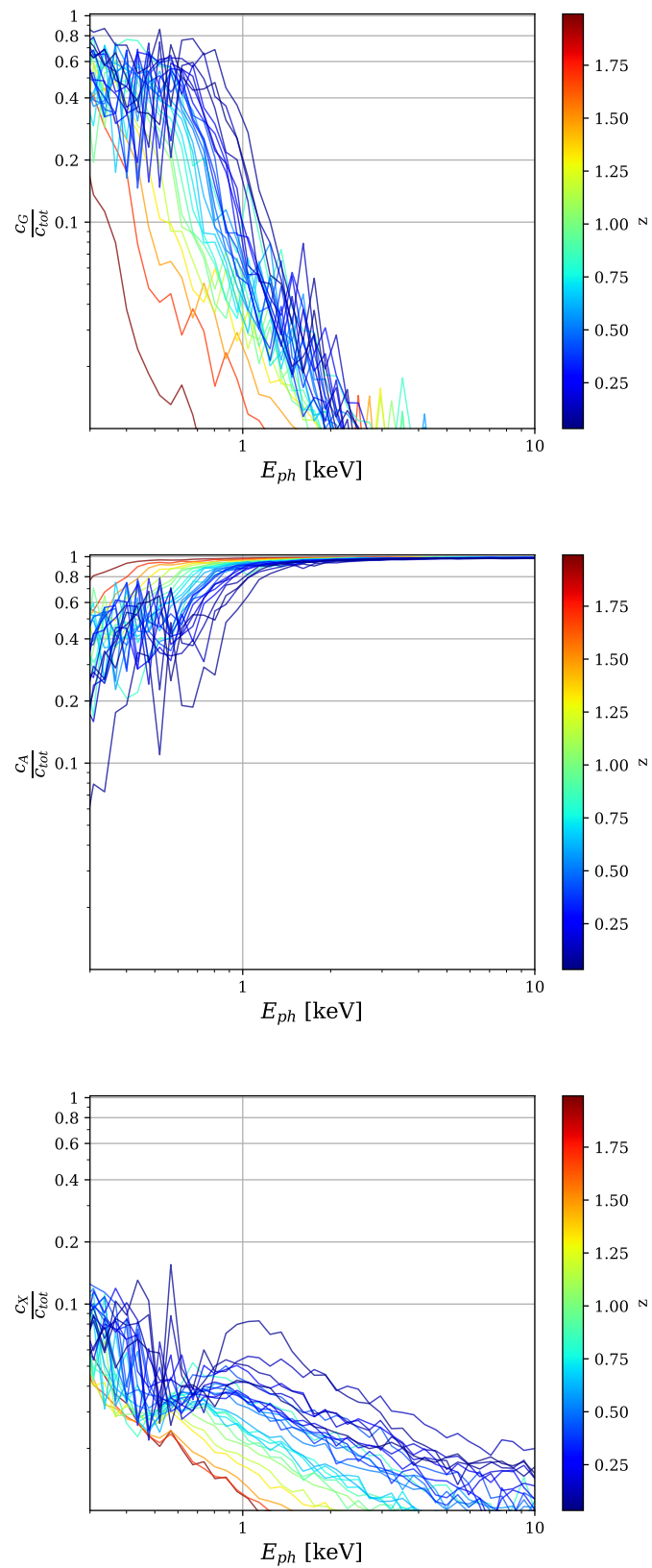


**Figure 4.21:** Relative contribution of gas (top panel), AGN (middle panel) and XRB emission to each redshift slice of the lightcone for the energy range 0.3 – 10 keV. The redshift of each slice is given by the colour gradient.



# Chapter 5

## Discussion

In this work we presented the implementation of a new X-ray emission model for the stellar component of cosmological simulations in the form of X-ray binary emission within the framework of the virtual photon simulator PHOX. We confirmed the validity of our model by reconstructing X-ray luminosity functions of local galaxies and confirming X-ray scaling relations. We then analysed the relative contribution of XRB emission for a set of simulated galaxies of the *Magneticum Pathfinder Simulation* set over a broad range of energies, with respect to their ISM and AGN emission. Lastly, we compared the X-ray emission within a lightcone view build from data of the *Magneticum Pathfinder simulation* with the unresolved cosmic X-ray background and find reasonable agreement for the power law behaviour in the hard X-ray band ( $E > 2$  keV). In the following we will summarize our main findings and provide an outlook on possible future investigations and improvements to the approach presented here.

### 5.1 Conclusions

X-ray luminosity functions of point sources like X-ray binaries have been used to study their abundance and distribution in local galaxies. It was found, that the population size of the two distinct types of XRBs follow observationally well constrained scaling relations which we used to provide estimates for the luminosity output of simulated coeval stellar populations [see e.g. Mineo et al. (2012a), Zhang, Gilfanov, and Bogdán (2012), Gilfanov (2004), and Grimm et al. (2003)]. In particular, we converted the cumulative XLFs into a pseudo CDF, which we statistically sampled to produce XRB populations distributed according to the underlying XLF within the SSP. With this approach we self-consistently derived XRB populations for stellar resolution elements in cosmological simulations by assuming linear scaling with stellar mass for the LMXB component, according to Gilfanov (2004), and using a star formation proxy based on Shtykovskiy and Gilfanov (2007), 2005 for the scaling of the HMXB component. We embedded the spectral modelling of the XRB component into the photon simulator PHOX in order to compare the synthetic X-ray emission caused by the XRB component with the spectral models already included (Chapter 4). Using simulated galaxies from *Magneticum*, we attempted to reconstruct the underlying cumulative XLF for each binary type (see 4.1) and achieved good agreement in the LMXB case for luminosities  $> 10^{36}$  erg s $^{-1}$  at  $z = 0.01$  (Section 4.2.1). For luminosities  $< 10^{36}$  erg s $^{-1}$  we find that we underestimate the analytic model by a factor of  $\sim 1.5$  and notice a significant flattening of the reconstructed XLF. The latter behaviour is also seen in reconstructed HMXB XLFs for which we generally report a strong deviation, attributed to significant scatter of the SFR scaling relation for low SFR due to low number statistics. The reconstructed XLFs also show evidence for some XRBs in the

ultra-luminous regime  $> 10^{39} \text{ erg s}^{-1}$  supporting a connection between ULXs and the high luminosity end of the XLFs.

The recovered stellar mass scaling relations for LMXB emission in local galaxies (Section 4.2.2) is in excellent agreement with the expected model of Zhang, Gilfanov, and Bogdán (2012) for stellar masses  $> 5 \cdot 10^{10} M_{\odot}$  and shows some scatter for stellar masses below that limit. The slightly lower luminosities compared to the model prediction by Zhang, Gilfanov, and Bogdán (2012) is connected to the flattening of the recovered XLFs still affecting the number prediction of LMXBs at luminosities  $> 5 \cdot 10^{37} \text{ erg s}^{-1}$ . In the HMXB case, the SFR scaling relation appears to follow a different relation than the one presented in Mineo et al. (2012a). We show that this is caused by (a) a different underlying model assumed by the authors and (b) significant scatter of the relation for low SFRs due to low number statistics. We note, that the relation in Mineo et al. (2012a) does not experience the same scatter seen in the reconstructed SFR relation due to a selection bias in their observations favouring galaxies with a bright HMXB component with sufficient number counts.

We showed that our implemented XRB model nicely reproduces expected spatial relations, namely that LMXB emission preferentially correlates with the position of old stars, and HMXB emission traces the star-formation regions and cold gas of a star-forming galaxy. We compared the relative strength of the two XRB components using our **Set 1** of simulated galaxies with  $\log(M_*/M_{\odot}) > 10.3$  (Section 4.3) at a redshift of  $z = 0.01$  in figure 4.8. It shows that the LMXB component is more prominent for 81% of the galaxies in our sample and the HXMB component only dominates for highly star-forming galaxies. The former observation is in line with theoretical predictions of binary synthesis models [Madau and Fragos (2017) and Fragos, Lehmer, Tremmel, et al. (2013)] claiming a LMXB dominance for low redshifts. Observations of Lehmer, Basu-Zych, et al. (2016) using the *Chandra* telescope came to similar conclusions of LMXBs dominating below redshift  $z \lesssim 2$ . From comparing the combined XRB component to the other two components already included in PHOX, we find that AGN emission dominates the XRB emission in the hard X-ray band 2 – 10 keV in 80% of the galaxy sample, while XRBs are dominant in the soft band (0.5 – 2 keV) in 50 – 60%. This is expected as the AGN model employed here has similar spectral properties and is much more luminous. The additional intrinsic absorption shipped with the AGN emission strongly suppresses the soft emission of AGN compared to XRB. For the gaseous component we find, that it dominates the XRB emission in the soft band in 55% of galaxies and is getting dominated in the hard X-ray band in 80 – 90% of galaxies. This, too, is not surprising given that thermal Bremsstrahlung is soft for plasma temperatures  $< 10^6 \text{ K}$  and has an additional temperature dependent cut-off in the hard part of the spectrum.

We analyzed the average composition of broad galaxy X-ray spectra and the relative contribution of the gaseous, XRB and AGN component over the whole spectral range:

- We did not find a clear difference in the average X-ray composition of early and late-type galaxies. For one, we attribute this observation to our choice of the projected halo volume being too small to capture extended hot gas halos of ETGs (see Fabbiano (1989)). Secondly, the hot gas component in the ISM of simulated galaxies may be overheated by insufficiently calibrated feedback mechanisms. Moreover, the effects of SFR on the XRB spectrum are lost by averaging over a large range of SFRs.
- We find that our average composite galaxy spectra are in good agreement with similar studies on star-burst galaxies from Wik et al. (2014) and Lehmer, Basu-Zych, et al. 2016, figure 4(a). Wik et al. (2014) also observe relative contributions of gas and XRB emission in agreement with our findings.
- We find a monotonous decrease in the relative contribution of the XRB component in

galaxies form intermediate to large stellar masses connected to an increase in hot gas emission resulting from deeper potential wells of the galaxies. Unexpectedly, we also find a slight decrease of the XRB component for low mass galaxies which is connected to a strong scatter seen in the  $L_X^{\text{HMXB}} - \text{SFR}$  relation (Figure 4.3) and moderate scatter for the  $L_X^{\text{LMXB}} - M_*$  (figure 4.2) relation for small values of SFR and  $M_*$  respectively.

- We find a non-monotonous behaviour in the XRB contribution with increasing SFR: the contribution is equally largest for non star-forming and highly star-forming galaxies but smallest for intermediate star-formation. This is connected to contamination of massive galaxies in the high star-formation bin, and LMXB contamination in the non star-forming bin. The reason for the relatively strong LMXB component in the non star-forming galaxies might be the inset of different feedback processes in the simulation disturbing the gas content which needs to be analyzed in more detail.

By constructing lightcones from *Box2* of *Magneticum* data, we show good agreement with measurements of the non-source cosmic X-ray background (nsCXB) in the 0.3 – 7 keV band [Cappelluti et al. (2017)] (Section 4.5). We find that the majority of the background is comprised of AGN emission analogous to AGN population synthesis studies [Ueda et al. (2014) and Gilli et al. (2007)]. However, we fail to reproduce the normalization of the unmasked, full CXB spectrum of Cappelluti et al. (2017) by a factor of  $\sim 4 - 5$ . This is probably due to the lightcone only extending to  $z \approx 2$  with a great fraction of more unresolved AGN missing from higher redshifts and a inconsistent treatment of AGN absorption. The latter has been corrected for future work. The contribution of the XRB component to the CXB is insignificant with less than 3% in the soft X-ray band and less than 1% in the hard X-ray band. We also show the redshift dependence of the relative contribution for each component where we find the XRB component decreasing for energies  $> 0.5$  keV with increasing redshift, which is expected since we do not account for the frame of reference when processing photon energies for the individual redshift slices. Also, Lehmer, Basu-Zych, et al. (2016) strongly argue for a redshift dependence in scaling relations of  $N_{\text{LMXB}} - M_*$  and  $N_{\text{HMXB}} - \text{SFR}$ .

## 5.2 Future Investigations

While we showed that our newly implemented model for XRB emission in SSPs is able to reasonably reproduce X-ray properties of local galaxies in agreement with observations, there is still room for improvement especially in the modelling of the HMXB component. Foremost, we want to update the implemented models based on more recent studies of Lehmer, Eufrasio, Basu-Zych, et al. (2021), Lehmer, Ferrell, et al. (2020), Lehmer, Eufrasio, Tzanavaris, et al. (2019), and Lehmer, Basu-Zych, et al. (2016) on the subject of XLFs and their scaling relations which were in part published during the course of this thesis. Additionally, the formation efficiency of HMXB in our model needs to be revisited due to it possibly being a badly constrained star-formation estimator. More recent studies on the formation efficiency of HMXB for different normalizations are presented in Antoniou et al. (2019) for the Small Magellanic Cloud and in Lehmer, Eufrasio, Markwardt, et al. (2017) for M51, which we want to test for compatibility. Furthermore, it is a known fact that low metallicity environments enhance the high-luminosity end of the HMXB XLF [Lehmer, Eufrasio, Basu-Zych, et al. (2021) and Garofali et al. (2020)]. Since most modern cosmological simulation track the metallicity evolution of baryonic matter [see e.g. Dolag, Mevius, et al. (2017)], it would be interesting to address this possibility in the future. Another interesting study that can be conducted with higher resolution simulations of galaxies are radial profiles of the XRB distribution or X-ray emission in general [see e.g. Fabbiano (2006)]. A general performance improvement might be the inclusion of a hard-coded luminosity limit. The main bottleneck

for a more sophisticated model, as proposed above, would be the repeated system call to `XSPEC` for every stellar element. Thus, we discard elements with total luminosity smaller than the luminosity limit, avoiding an unnecessary call to `XSPEC`. Of course, the limit has to be chosen such that the expected photon count is far below  $N_{ph} = 1$  in order to not distort the results.

Regarding the results acquired in this thesis, some of the correlations between galactic properties like stellar mass or SFR binning need to be revisited and investigated in more detail to explain the unexpected behaviour in some of the bins. Since we proposed that feedback mechanisms in the simulation might be involved, it would be interesting to follow up on this subject. Of course, influences of other galactic properties on the XRB contribution can be investigated, e.g. for their morphological b-Value [Teklu et al. (2015)], BH accretion rate, metallicity, etc. Also, the influence of the projected volume on galactic scaling relations requires additional investigation to reduce potential systematic errors. Furthermore, it would be interesting to analyze the simulated CXB up to higher redshifts to see if the observed turnover at 30 keV can be recreated. With respect to the redshift dependence of the XRB component, a different approach can be used to avoid having to deal with absorption when shifting the spectrum into the rest-frame. Namely, we would shift each snapshot to a common low redshift and produce the spectra at that redshift. In this way, we simulate an observer being at roughly the same redshift as the snapshot such that we can compare differences in the relative contribution more accurately and can make predictions of the emissivity (total luminosity per cosmic volume in units of  $\text{erg s}^{-1} \text{Mpc}^{-3}$ ) for the different components [see e.g. Madau and Fragos (2017) and Lehmer, Basu-Zych, et al. (2016)].

# References

- Abramowicz, Marek A., Xingming Chen, Shoji Kato, Jean-Pierre Lasota, and Oded Regev (Jan. 1995). “Thermal Equilibria of Accretion Disks”. In: *The Astrophysical Journal, Letters* 438, p. L37. DOI: 10.1086/187709. arXiv: astro-ph/9409018 [astro-ph].
- Andersen, J. (Jan. 1991). “Accurate masses and radii of normal stars”. In: *Astronomy & Astrophysics, Reviews* 3.2, pp. 91–126. DOI: 10.1007/BF00873538.
- Antoniou, Vallia, Andreas Zezas, Jeremy J. Drake, Carles Badenes, Frank Haberl, Nicholas J. Wright, Jaesub Hong, Rosanne Di Stefano, Terrance J. Gaetz, Knox S. Long, Paul P. Plucinsky, Manami Sasaki, Benjamin F. Williams, P. Frank Winkler, and SMC XVP Collaboration (Dec. 2019). “Deep Chandra Survey of the Small Magellanic Cloud. III. Formation Efficiency of High-mass X-Ray Binaries”. In: *The Astrophysical Journal* 887.1, 20, p. 20. DOI: 10.3847/1538-4357/ab4a7a. arXiv: 1901.01237 [astro-ph.HE].
- Appenzeller, I. and R. Mundt (Nov. 1989). “T Tauri stars”. In: *Astronomy & Astrophysics, Reviews* 1.3-4, pp. 291–334. DOI: 10.1007/BF00873081.
- Arnaud, K. A. (Jan. 1996). “XSPEC: The First Ten Years”. In: *Astronomical Data Analysis Software and Systems V*. Ed. by George H. Jacoby and Jeannette Barnes. Vol. 101. Astronomical Society of the Pacific Conference Series, p. 17.
- Arth, Alexander, Klaus Dolag, Alexander M. Beck, Margarita Petkova, and Harald Lesch (Dec. 2014). “Anisotropic thermal conduction in galaxy clusters with MHD in Gadget”. In: *arXiv e-prints*, arXiv:1412.6533, arXiv:1412.6533. arXiv: 1412.6533 [astro-ph.CO].
- Balbus, Steven A. and John F. Hawley (July 1991). “A Powerful Local Shear Instability in Weakly Magnetized Disks. I. Linear Analysis”. In: *The Astrophysical Journal* 376, p. 214. DOI: 10.1086/170270.
- Banerjee, Srimanta, Marat Gilfanov, Sudip Bhattacharyya, and Rashid Sunyaev (Nov. 2020). “Observing imprints of black hole event horizon on X-ray spectra”. In: *Monthly Notices of the Royal Astronomical Society* 498.4, pp. 5353–5360. DOI: 10.1093/mnras/staa2788. arXiv: 2009.07222 [astro-ph.HE].
- Baraffe, I., G. Chabrier, F. Allard, and P. H. Hauschildt (Sept. 1998). “Evolutionary models for solar metallicity low-mass stars: mass-magnitude relationships and color-magnitude diagrams”. In: *Astronomy & Astrophysics* 337, pp. 403–412. arXiv: astro-ph/9805009 [astro-ph].
- Beck, A. M., G. Murante, A. Arth, R. -S. Remus, A. F. Teklu, J. M. F. Donnert, S. Planelles, M. C. Beck, P. Förster, M. Imgrund, K. Dolag, and S. Borgani (Jan. 2016). “An improved SPH scheme for cosmological simulations”. In: *Monthly Notices of the Royal Astronomical Society* 455.2, pp. 2110–2130. DOI: 10.1093/mnras/stv2443. arXiv: 1502.07358 [astro-ph.CO].
- Beckmann, Volker and Chris R. Shrader (2012). *Active Galactic Nuclei*.
- Belczynski, Krzysztof, Vassiliki Kalogera, Frederic A. Rasio, Ronald E. Taam, Andreas Zezas, Tomasz Bulik, Thomas J. Maccarone, and Natalia Ivanova (Jan. 2008). “Compact Object Modeling with the StarTrack Population Synthesis Code”. In: *The Astrophysical Journal, Supplement* 174.1, pp. 223–260. DOI: 10.1086/521026. arXiv: astro-ph/0511811 [astro-ph].

- Biffi, V., K. Dolag, H. Böhringer, and G. Lemson (Mar. 2012). “Observing simulated galaxy clusters with PHOX: a novel X-ray photon simulator”. In: *Monthly Notices of the Royal Astronomical Society* 420.4, pp. 3545–3556. DOI: 10.1111/j.1365-2966.2011.20278.x. arXiv: 1112.0314 [astro-ph.CO].
- Biffi, V., K. Dolag, and A. Merloni (Dec. 2018). “AGN contamination of galaxy-cluster thermal X-ray emission: predictions for eRosita from cosmological simulations”. In: *Monthly Notices of the Royal Astronomical Society* 481.2, pp. 2213–2227. DOI: 10.1093/mnras/sty2436. arXiv: 1804.01096 [astro-ph.CO].
- Bondi, H. (Jan. 1952). “On spherically symmetrical accretion”. In: *Monthly Notices of the Royal Astronomical Society* 112, p. 195. DOI: 10.1093/mnras/112.2.195.
- Bondi, H. and F. Hoyle (Jan. 1944). “On the mechanism of accretion by stars”. In: *Monthly Notices of the Royal Astronomical Society* 104, p. 273. DOI: 10.1093/mnras/104.5.273.
- Borson, Bram, Dong-Woo Kim, and Giuseppina Fabbiano (Mar. 2011). “Revisiting with Chandra the Scaling Relations of the X-ray Emission Components (Binaries, Nuclei, and Hot Gas) of Early-type Galaxies”. In: *The Astrophysical Journal* 729.1, 12, p. 12. DOI: 10.1088/0004-637X/729/1/12. arXiv: 1011.2529 [astro-ph.HE].
- Boylan-Kolchin, Michael, Volker Springel, Simon D. M. White, Adrian Jenkins, and Gerard Lemson (Sept. 2009). “Resolving cosmic structure formation with the Millennium-II Simulation”. In: *Monthly Notices of the Royal Astronomical Society* 398.3, pp. 1150–1164. DOI: 10.1111/j.1365-2966.2009.15191.x. arXiv: 0903.3041 [astro-ph.CO].
- Buchner, J., A. Georgakakis, K. Nandra, L. Hsu, C. Rangel, M. Brightman, A. Merloni, M. Salvato, J. Donley, and D. Kocevski (Apr. 2014). “X-ray spectral modelling of the AGN obscuring region in the CDFS: Bayesian model selection and catalogue”. In: *Astronomy & Astrophysics* 564, A125, A125. DOI: 10.1051/0004-6361/201322971. arXiv: 1402.0004 [astro-ph.HE].
- Cappelluti, Nico, Yanxia Li, Angelo Ricarte, Bhaskar Agarwal, Viola Allevato, Tonima Tasnim Ananna, Marco Ajello, Francesca Civano, Andrea Comastri, Martin Elvis, Alexis Finoguenov, Roberto Gilli, Günther Hasinger, Stefano Marchesi, Priyamvada Natarajan, Fabio Pacucci, E. Treister, and C. Megan Urry (Mar. 2017). “The Chandra COSMOS Legacy Survey: Energy Spectrum of the Cosmic X-Ray Background and Constraints on Undetected Populations”. In: *The Astrophysical Journal* 837.1, 19, p. 19. DOI: 10.3847/1538-4357/aa5ea4. arXiv: 1702.01660 [astro-ph.HE].
- Chabrier, Gilles (July 2003). “Galactic Stellar and Substellar Initial Mass Function”. In: *Publications of the ASP* 115.809, pp. 763–795. DOI: 10.1086/376392. arXiv: astro-ph/0304382 [astro-ph].
- Churazov, E., S. Sazonov, R. Sunyaev, W. Forman, C. Jones, and H. Böhringer (Oct. 2005). “Supermassive black holes in elliptical galaxies: switching from very bright to very dim”. In: *Monthly Notices of the Royal Astronomical Society* 363.1, pp. L91–L95. DOI: 10.1111/j.1745-3933.2005.00093.x. arXiv: astro-ph/0507073 [astro-ph].
- D’Orazio, Daniel J. and Paul C. Duffell (Mar. 2021). “Orbital Evolution of Equal-Mass Eccentric Binaries Due to a Gas Disk: Eccentric Inspirals and Circular Outspirals”. In: *arXiv e-prints*, arXiv:2103.09251, arXiv:2103.09251. arXiv: 2103.09251 [astro-ph.HE].
- Di Matteo, Tiziana, Volker Springel, and Lars Hernquist (Feb. 2005). “Energy input from quasars regulates the growth and activity of black holes and their host galaxies”. In: *Nature* 433.7026, pp. 604–607. DOI: 10.1038/nature03335. arXiv: astro-ph/0502199 [astro-ph].
- Dolag, K., S. Borgani, G. Murante, and V. Springel (Oct. 2009). “Substructures in hydrodynamical cluster simulations”. In: *Monthly Notices of the Royal Astronomical Society* 399.2, pp. 497–514. DOI: 10.1111/j.1365-2966.2009.15034.x. arXiv: 0808.3401 [astro-ph].

- Dolag, K., S. Borgani, S. Schindler, A. Diaferio, and A. M. Bykov (Feb. 2008). “Simulation Techniques for Cosmological Simulations”. In: *Space Science Reviews* 134.1-4, pp. 229–268. DOI: 10.1007/s11214-008-9316-5. arXiv: 0801.1023 [astro-ph].
- Dolag, K., M. Jubelgas, V. Springel, S. Borgani, and E. Rasia (May 2004). “Thermal Conduction in Simulated Galaxy Clusters”. In: *The Astrophysical Journal, Letters* 606.2, pp. L97–L100. DOI: 10.1086/420966. arXiv: astro-ph/0401470 [astro-ph].
- Dolag, K., E. Komatsu, and R. Sunyaev (Dec. 2016). “SZ effects in the Magneticum Pathfinder simulation: comparison with the Planck, SPT, and ACT results”. In: *Monthly Notices of the Royal Astronomical Society* 463.2, pp. 1797–1811. DOI: 10.1093/mnras/stw2035. arXiv: 1509.05134 [astro-ph.CO].
- Dolag, K., F. Vazza, G. Brunetti, and G. Tormen (Dec. 2005). “Turbulent gas motions in galaxy cluster simulations: the role of smoothed particle hydrodynamics viscosity”. In: *Monthly Notices of the Royal Astronomical Society* 364.3, pp. 753–772. DOI: 10.1111/j.1365-2966.2005.09630.x. arXiv: astro-ph/0507480 [astro-ph].
- Dolag, Klaus, Emilio Mevius, and Rhea-Silvia Remus (Aug. 2017). “Distribution and Evolution of Metals in the Magneticum Simulations”. In: *Galaxies* 5.3, p. 35. DOI: 10.3390/galaxies5030035. arXiv: 1708.00027 [astro-ph.GA].
- Done, Chris, Marek Gierliński, and Aya Kubota (Dec. 2007). “Modelling the behaviour of accretion flows in X-ray binaries. Everything you always wanted to know about accretion but were afraid to ask”. In: *Astronomy & Astrophysics, Reviews* 15.1, pp. 1–66. DOI: 10.1007/s00159-007-0006-1. arXiv: 0708.0148 [astro-ph].
- Duffell, Paul C., Daniel D’Orazio, Andrea Derdzinski, Zoltan Haiman, Andrew MacFadyen, Anna L. Rosen, and Jonathan Zrake (Sept. 2020). “Circumbinary Disks: Accretion and Torque as a Function of Mass Ratio and Disk Viscosity”. In: *The Astrophysical Journal* 901.1, 25, p. 25. DOI: 10.3847/1538-4357/abab95. arXiv: 1911.05506 [astro-ph.SR].
- Eker, Z., F. Soyduğan, E. Soyduğan, S. Bilir, E. Yaz Gökçe, I. Steer, M. Tüysüz, T. Şenyüz, and O. Demircan (Apr. 2015). “Main-Sequence Effective Temperatures from a Revised Mass-Luminosity Relation Based on Accurate Properties”. In: *The Astronomical Journal* 149.4, 131, p. 131. DOI: 10.1088/0004-6256/149/4/131. arXiv: 1501.06585 [astro-ph.SR].
- Fabbiano, G. (Jan. 1989). “X-rays from normal galaxies.” In: *Annual Review of Astronomy & Astrophysics* 27, pp. 87–138. DOI: 10.1146/annurev.aa.27.090189.000511.
- Fabbiano, G. (Sept. 2006). “Populations of X-Ray Sources in Galaxies”. In: *Annual Review of Astronomy & Astrophysics* 44.1, pp. 323–366. DOI: 10.1146/annurev.astro.44.051905.092519. arXiv: astro-ph/0511481 [astro-ph].
- Fabjan, D., S. Borgani, L. Tornatore, A. Saro, G. Murante, and K. Dolag (Jan. 2010). “Simulating the effect of active galactic nuclei feedback on the metal enrichment of galaxy clusters”. In: *Monthly Notices of the Royal Astronomical Society* 401.3, pp. 1670–1690. DOI: 10.1111/j.1365-2966.2009.15794.x. arXiv: 0909.0664 [astro-ph.CO].
- Fragos, T., B. Lehmer, M. Tremmel, P. Tzanavaris, A. Basu-Zych, K. Belczynski, A. Hornschemeier, L. Jenkins, V. Kalogera, A. Ptak, and A. Zezas (Feb. 2013). “X-Ray Binary Evolution Across Cosmic Time”. In: *The Astrophysical Journal* 764.1, 41, p. 41. DOI: 10.1088/0004-637X/764/1/41. arXiv: 1206.2395 [astro-ph.HE].
- Fragos, T., B. D. Lehmer, S. Naoz, A. Zezas, and A. Basu-Zych (Oct. 2013). “Energy Feedback from X-Ray Binaries in the Early Universe”. In: *The Astrophysical Journal, Letters* 776.2, L31, p. L31. DOI: 10.1088/2041-8205/776/2/L31. arXiv: 1306.1405 [astro-ph.CO].
- Frank, Juhan, Andrew King, and Derek J. Raine (2002). *Accretion Power in Astrophysics: Third Edition*.
- Garofali, Kristen, Bret D. Lehmer, Antara Basu-Zych, Lacey A. West, Daniel Wik, Mihoko Yukita, Neven Vulic, Andrew Ptak, and Ann Hornschemeier (Nov. 2020). “On the X-Ray Spectral Energy Distributions of Star-forming Galaxies: The 0.3-30 keV Spectrum of

- the Low-metallicity Starburst Galaxy VV 114”. In: *The Astrophysical Journal* 903.2, 79, p. 79. DOI: 10.3847/1538-4357/abba2d. arXiv: 2009.08985 [astro-ph.HE].
- Ge, Hongwei, Ronald F. Webbink, and Zhanwen Han (July 2020). “The Thermal Equilibrium Mass-loss Model and Its Applications in Binary Evolution”. In: *The Astrophysical Journal, Supplement* 249.1, 9, p. 9. DOI: 10.3847/1538-4365/ab98f6. arXiv: 2006.00774 [astro-ph.SR].
- Gilfanov, M. (Mar. 2004). “Low-mass X-ray binaries as a stellar mass indicator for the host galaxy”. In: *Monthly Notices of the Royal Astronomical Society* 349.1, pp. 146–168. DOI: 10.1111/j.1365-2966.2004.07473.x. arXiv: astro-ph/0309454 [astro-ph].
- Gilfanov, M., H. -J. Grimm, and R. Sunyaev (Jan. 2004). “ $L_X$ -SFR relation in star-forming galaxies”. In: *Monthly Notices of the Royal Astronomical Society* 347.3, pp. L57–L60. DOI: 10.1111/j.1365-2966.2004.07450.x. arXiv: astro-ph/0301331 [astro-ph].
- Gilli, R., A. Comastri, and G. Hasinger (Feb. 2007). “The synthesis of the cosmic X-ray background in the Chandra and XMM-Newton era”. In: *Astronomy & Astrophysics* 463.1, pp. 79–96. DOI: 10.1051/0004-6361:20066334. arXiv: astro-ph/0610939 [astro-ph].
- Grimm, H. -J., M. Gilfanov, and R. Sunyaev (Mar. 2003). “High-mass X-ray binaries as a star formation rate indicator in distant galaxies”. In: *Monthly Notices of the Royal Astronomical Society* 339.3, pp. 793–809. DOI: 10.1046/j.1365-8711.2003.06224.x. arXiv: astro-ph/0205371 [astro-ph].
- Guo, Qi, Simon White, Michael Boylan-Kolchin, Gabriella De Lucia, Guinevere Kauffmann, Gerard Lemson, Cheng Li, Volker Springel, and Simone Weinmann (May 2011). “From dwarf spheroidals to cD galaxies: simulating the galaxy population in a  $\Lambda$ CDM cosmology”. In: *Monthly Notices of the Royal Astronomical Society* 413.1, pp. 101–131. DOI: 10.1111/j.1365-2966.2010.18114.x. arXiv: 1006.0106 [astro-ph.CO].
- Haardt, F. and P. Madau (Jan. 2001). “Modelling the UV/X-ray cosmic background with CUBA”. In: *Clusters of Galaxies and the High Redshift Universe Observed in X-rays*. Ed. by D. M. Neumann and J. T. V. Tran, p. 64. arXiv: astro-ph/0106018 [astro-ph].
- Hirschmann, Michaela, Klaus Dolag, Alexandro Saro, Lisa Bachmann, Stefano Borgani, and Andreas Burkert (Aug. 2014). “Cosmological simulations of black hole growth: AGN luminosities and downsizing”. In: *Monthly Notices of the Royal Astronomical Society* 442.3, pp. 2304–2324. DOI: 10.1093/mnras/stu1023. arXiv: 1308.0333 [astro-ph.CO].
- Hopkins, Philip F., Gordon T. Richards, and Lars Hernquist (Jan. 2007). “An Observational Determination of the Bolometric Quasar Luminosity Function”. In: *The Astrophysical Journal* 654.2, pp. 731–753. DOI: 10.1086/509629. arXiv: astro-ph/0605678 [astro-ph].
- Hoyle, F. and R. A. Lyttleton (Jan. 1939). “The effect of interstellar matter on climatic variation”. In: *Proceedings of the Cambridge Philosophical Society* 35.3, p. 405. DOI: 10.1017/S0305004100021150.
- Kaastra, J. S. and R. Mewe (Jan. 1993). “X-ray emission from thin plasmas. I - Multiple Auger ionisation and fluorescence processes for Be to Zn”. In: *Astronomy & Astrophysics, Supplements* 97.2, pp. 443–482.
- Katz, Neal, David H. Weinberg, and Lars Hernquist (July 1996). “Cosmological Simulations with TreeSPH”. In: *The Astrophysical Journal, Supplement* 105, p. 19. DOI: 10.1086/192305. arXiv: astro-ph/9509107 [astro-ph].
- Kawamuro, T., H. Negoro, T. Yoneyama, S. Ueno, H. Tomida, M. Ishikawa, Y. Sugawara, N. Isobe, R. Shimomukai, T. Mihara, M. Sugizaki, S. Nakahira, W. Iwakiri, F. Yatabe, Y. Takao, M. Matsuoka, N. Kawai, S. Sugita, T. Yoshii, Y. Tachibana, S. Harita, K. Morita, A. Yoshida, T. Sakamoto, M. Serino, Y. Kawakubo, Y. Kitaoka, T. Hashimoto, H. Tsunemi, M. Nakajima, T. Kawase, A. Sakamaki, W. Maruyama, Y. Ueda, T. Hori, A. Tanimoto, S. Oda, T. Morita, S. Yamada, Y. Tsuboi, Y. Nakamura, R. Sasaki, H. Kawai, T. Sato, M. Yamauchi, C. Hanyu, K. Hidaka, K. Yamaoka, and M. Shidatsu (Mar. 2018).

- “MAXI/GSC detection of a probable new X-ray transient MAXI J1820+070”. In: *The Astronomer’s Telegram* 11399, p. 1.
- Kennicutt Robert C., Jr. (May 1998). “The Global Schmidt Law in Star-forming Galaxies”. In: *The Astrophysical Journal* 498.2, pp. 541–552. DOI: 10.1086/305588. arXiv: astro-ph/9712213 [astro-ph].
- Kim, Dong-Woo and Giuseppina Fabbiano (Oct. 2010). “X-ray Properties of Young Early-type Galaxies. I. X-ray Luminosity Function of Low-mass X-ray Binaries”. In: *The Astrophysical Journal* 721.2, pp. 1523–1530. DOI: 10.1088/0004-637X/721/2/1523. arXiv: 1004.2427 [astro-ph.CO].
- Komatsu, E., K. M. Smith, J. Dunkley, C. L. Bennett, B. Gold, G. Hinshaw, N. Jarosik, D. Larson, M. R.olta, L. Page, D. N. Spergel, M. Halpern, R. S. Hill, A. Kogut, M. Limon, S. S. Meyer, N. Odegard, G. S. Tucker, J. L. Weiland, E. Wollack, and E. L. Wright (Feb. 2011). “Seven-year Wilkinson Microwave Anisotropy Probe (WMAP) Observations: Cosmological Interpretation”. In: *The Astrophysical Journal, Supplement* 192.2, 18, p. 18. DOI: 10.1088/0067-0049/192/2/18. arXiv: 1001.4538 [astro-ph.CO].
- Körding, Elmar G., Sebastian Jester, and Rob Fender (Nov. 2006). “Accretion states and radio loudness in active galactic nuclei: analogies with X-ray binaries”. In: *Monthly Notices of the Royal Astronomical Society* 372.3, pp. 1366–1378. DOI: 10.1111/j.1365-2966.2006.10954.x. arXiv: astro-ph/0608628 [astro-ph].
- Kovlakas, K., A. Zezas, J. J. Andrews, A. Basu-Zych, T. Fragos, A. Hornschemeier, B. Lehmer, and A. Ptak (Nov. 2020). “A census of ultraluminous X-ray sources in the local Universe”. In: *Monthly Notices of the Royal Astronomical Society* 498.4, pp. 4790–4810. DOI: 10.1093/mnras/staa2481. arXiv: 2008.10572 [astro-ph.GA].
- Kravtsov, Andrey V. (Jan. 1999). “High-resolution simulations of structure formation in the universe”. PhD thesis. NEW MEXICO STATE UNIVERSITY.
- Kravtsov, Andrey V. and Stefano Borgani (Sept. 2012). “Formation of Galaxy Clusters”. In: *Annual Review of Astronomy & Astrophysics* 50, pp. 353–409. DOI: 10.1146/annurev-astro-081811-125502. arXiv: 1205.5556 [astro-ph.CO].
- Kravtsov, Andrey V., Anatoly Klypin, and Yehuda Hoffman (June 2002). “Constrained Simulations of the Real Universe. II. Observational Signatures of Intergalactic Gas in the Local Supercluster Region”. In: *The Astrophysical Journal* 571.2, pp. 563–575. DOI: 10.1086/340046. arXiv: astro-ph/0109077 [astro-ph].
- Kudritzki, Rolf-Peter and Joachim Puls (Jan. 2000). “Winds from Hot Stars”. In: *Annual Review of Astronomy & Astrophysics* 38, pp. 613–666. DOI: 10.1146/annurev.astro.38.1.613.
- Lehmer, B. D., A. R. Basu-Zych, S. Mineo, W. N. Brandt, R. T. Eufrazio, T. Fragos, A. E. Hornschemeier, B. Luo, Y. Q. Xue, F. E. Bauer, M. Gilfanov, P. Ranalli, D. P. Schneider, O. Shemmer, P. Tozzi, J. R. Trump, C. Vignali, J. -X. Wang, M. Yukita, and A. Zezas (July 2016). “The Evolution of Normal Galaxy X-Ray Emission through Cosmic History: Constraints from the 6 MS Chandra Deep Field-South”. In: *The Astrophysical Journal* 825.1, 7, p. 7. DOI: 10.3847/0004-637X/825/1/7. arXiv: 1604.06461 [astro-ph.GA].
- Lehmer, B. D., R. T. Eufrazio, L. Markwardt, A. Zezas, A. Basu-Zych, T. Fragos, A. E. Hornschemeier, A. Ptak, P. Tzanavaris, and M. Yukita (Dec. 2017). “On the Spatially Resolved Star Formation History in M51. II. X-Ray Binary Population Evolution”. In: *The Astrophysical Journal* 851.1, 11, p. 11. DOI: 10.3847/1538-4357/aa9578. arXiv: 1710.09403 [astro-ph.GA].
- Lehmer, Bret D., Rafael T. Eufrazio, Antara Basu-Zych, Keith Doore, Tassos Fragos, Kristen Garofali, Konstantinos Kovlakas, Benjamin F. Williams, Andreas Zezas, and Luidhy Santana-Silva (Jan. 2021). “The Metallicity Dependence of the High-mass X-Ray Binary Luminosity Function”. In: *The Astrophysical Journal* 907.1, 17, p. 17. DOI: 10.3847/1538-4357/abcec1. arXiv: 2011.09476 [astro-ph.GA].

- Lehmer, Bret D., Rafael T. Eufrazio, Panayiotis Tzanavaris, Antara Basu-Zych, Tassos Fragos, Andrea Prestwich, Mihoko Yukita, Andreas Zezas, Ann E. Hornschemeier, and Andrew Ptak (July 2019). “X-Ray Binary Luminosity Function Scaling Relations for Local Galaxies Based on Subgalactic Modeling”. In: *The Astrophysical Journal, Supplement* 243.1, 3, p. 3. DOI: 10.3847/1538-4365/ab22a8. arXiv: 1905.05197 [astro-ph.GA].
- Lehmer, Bret D., Andrew P. Ferrell, Keith Doore, Rafael T. Eufrazio, Erik B. Monson, David M. Alexander, Antara Basu-Zych, William N. Brandt, Gregory R. Sivakoff, Panayiotis Tzanavaris, Mihoko Yukita, Tassos Fragos, and Andrew Ptak (June 2020). “X-Ray Binary Luminosity Function Scaling Relations in Elliptical Galaxies: Evidence for Globular Cluster Seeding of Low-mass X-Ray Binaries in Galactic Fields”. In: *The Astrophysical Journal, Supplement* 248.2, 31, p. 31. DOI: 10.3847/1538-4365/ab9175. arXiv: 2004.13045 [astro-ph.GA].
- Lewin, Walter H. G. and Michiel van der Klis (2006). *Compact Stellar X-ray Sources*. Vol. 39. ISBN: 0-511-16808-x.
- Lewin, Walter H. G., Jan van Paradijs, and Ronald E. Taam (Sept. 1993). “X-Ray Bursts”. In: *Space Science Reviews* 62.3-4, pp. 223–389. DOI: 10.1007/BF00196124.
- Lewin, Walter H. G., Jan van Paradijs, and Edward Peter Jacobus van den Heuvel (1995). *X-ray Binaries*. Cambridge University Press. ISBN: 0-521-41684-1.
- Liedahl, Duane A., Albert L. Osterheld, and William H. Goldstein (Jan. 1995). “New Calculations of Fe L-Shell X-Ray Spectra in High-Temperature Plasmas”. In: *The Astrophysical Journal, Letters* 438, p. L115. DOI: 10.1086/187729.
- Lotz, Marcel, Rhea-Silvia Remus, Klaus Dolag, Andrea Biviano, and Andreas Burkert (Oct. 2019). “Gone after one orbit: How cluster environments quench galaxies”. In: *Monthly Notices of the Royal Astronomical Society* 488.4, pp. 5370–5389. DOI: 10.1093/mnras/stz2070. arXiv: 1810.02382 [astro-ph.GA].
- Madau, Piero and Tassos Fragos (May 2017). “Radiation Backgrounds at Cosmic Dawn: X-Rays from Compact Binaries”. In: *The Astrophysical Journal* 840.1, 39, p. 39. DOI: 10.3847/1538-4357/aa6af9. arXiv: 1606.07887 [astro-ph.GA].
- Maio, Umberto, Massimo Dotti, Margarita Petkova, Albino Perego, and Marta Volonteri (Apr. 2013). “Effects of Circumnuclear Disk Gas Evolution on the Spin of Central Black Holes”. In: *The Astrophysical Journal* 767.1, 37, p. 37. DOI: 10.1088/0004-637X/767/1/37. arXiv: 1203.1877 [astro-ph.HE].
- Marconi, A., G. Risaliti, R. Gilli, L. K. Hunt, R. Maiolino, and M. Salvati (June 2004). “Local supermassive black holes, relics of active galactic nuclei and the X-ray background”. In: *Monthly Notices of the Royal Astronomical Society* 351.1, pp. 169–185. DOI: 10.1111/j.1365-2966.2004.07765.x. arXiv: astro-ph/0311619 [astro-ph].
- Mewe, R., E. H. B. M. Gronenschild, and G. H. J. van den Oord (Nov. 1985). “Calculated X-radiation from optically thin plasmas. V.” In: *Astronomy & Astrophysics, Supplements* 62, pp. 197–254.
- Mineo, S., M. Gilfanov, and R. Sunyaev (Jan. 2012a). “X-ray emission from star-forming galaxies - I. High-mass X-ray binaries”. In: *Monthly Notices of the Royal Astronomical Society* 419.3, pp. 2095–2115. DOI: 10.1111/j.1365-2966.2011.19862.x. arXiv: 1105.4610 [astro-ph.HE].
- Mineo, S., M. Gilfanov, and R. Sunyaev (Nov. 2012b). “X-ray emission from star-forming galaxies - II. Hot interstellar medium”. In: *Monthly Notices of the Royal Astronomical Society* 426.3, pp. 1870–1883. DOI: 10.1111/j.1365-2966.2012.21831.x. arXiv: 1205.3715 [astro-ph.HE].
- Misra, D., T. Fragos, T. M. Tauris, E. Zapartas, and D. R. Aguilera-Dena (Oct. 2020). “The origin of pulsating ultra-luminous X-ray sources: Low- and intermediate-mass X-ray binaries containing neutron star accretors”. In: *Astronomy & Astrophysics* 642, A174, A174. DOI: 10.1051/0004-6361/202038070. arXiv: 2004.01205 [astro-ph.HE].

- Moe, Maxwell and Rosanne Di Stefano (June 2017). “Mind Your Ps and Qs: The Interrelation between Period (P) and Mass-ratio (Q) Distributions of Binary Stars”. In: *The Astrophysical Journal, Supplement* 230.2, 15, p. 15. DOI: 10.3847/1538-4365/aa6fb6. arXiv: 1606.05347 [astro-ph.SR].
- Morrison, R. and D. McCammon (July 1983). “Interstellar photoelectric absorption cross sections, 0.03-10 keV.” In: *The Astrophysical Journal* 270, pp. 119–122. DOI: 10.1086/161102.
- Neijssel, Coenraad J., Serena Vinciguerra, Alejandro Vigna-Gómez, Ryosuke Hirai, James C. A. Miller-Jones, Arash Bahramian, Thomas J. Maccarone, and Ilya Mandel (Feb. 2021). “Wind Mass-loss Rates of Stripped Stars Inferred from Cygnus X-1”. In: *The Astrophysical Journal* 908.2, 118, p. 118. DOI: 10.3847/1538-4357/abde4a. arXiv: 2102.09092 [astro-ph.SR].
- Persic, M. and Y. Rephaeli (Feb. 2002). “X-ray spectral components of starburst galaxies”. In: *Astronomy & Astrophysics* 382, pp. 843–859. DOI: 10.1051/0004-6361:20011679. arXiv: astro-ph/0112030 [astro-ph].
- Persic, M. and Y. Rephaeli (Feb. 2003). “Starburst galaxies and the X-ray background”. In: *Astronomy & Astrophysics* 399, pp. 9–17. DOI: 10.1051/0004-6361:20021738. arXiv: astro-ph/0211532 [astro-ph].
- Pontzen, A., R. Roškar, G. S. Stinson, R. Woods, D. M. Reed, J. Coles, and T. R. Quinn (2013). *pynbody: Astrophysics Simulation Analysis for Python*. Astrophysics Source Code Library, ascl:1305.002.
- Postnov, Konstantin A. and Lev R. Yungelson (May 2014). “The Evolution of Compact Binary Star Systems”. In: *Living Reviews in Relativity* 17.1, 3, p. 3. DOI: 10.12942/lrr-2014-3. arXiv: 1403.4754 [astro-ph.HE].
- Predehl, P., R. Andritschke, V. Arefiev, V. Babyshkin, O. Batanov, W. Becker, H. Böhringer, A. Bogomolov, T. Boller, K. Borm, W. Bornemann, H. Bräuninger, M. Brüggem, H. Brunner, M. Brusa, E. Bulbul, M. Buntov, V. Burwitz, W. Burkert, N. Clerc, E. Churazov, D. Coutinho, T. Dauser, K. Dennerl, V. Doroshenko, J. Eder, V. Emberger, T. Eraerds, A. Finoguenov, M. Freyberg, P. Friedrich, S. Friedrich, M. Fürmetz, A. Georgakakis, M. Gilfanov, S. Granato, C. Grossberger, A. Gueguen, P. Gureev, F. Haberl, O. Hälker, G. Hartner, G. Hasinger, H. Huber, L. Ji, A. v. Kienlin, W. Kink, F. Korotkov, I. Kreykenbohm, G. Lamer, I. Lomakin, I. Lapshov, T. Liu, C. Maitra, N. Meidinger, B. Menz, A. Merloni, T. Mernik, B. Mican, J. Mohr, S. Müller, K. Nandra, V. Nazarov, F. Pacaud, M. Pavlinsky, E. Perinati, E. Pfeffermann, D. Pietschner, M. E. Ramos-Ceja, A. Rau, J. Reiffers, T. H. Reiprich, J. Robrade, M. Salvato, J. Sanders, A. Santangelo, M. Sasaki, H. Scheuerle, C. Schmid, J. Schmitt, A. Schwöpe, A. Shirshakov, M. Steinmetz, I. Stewart, L. Strüder, R. Sunyaev, C. Tenzer, L. Tiedemann, J. Trümper, V. Voron, P. Weber, J. Wilms, and V. Yaroshenko (Mar. 2021). “The eROSITA X-ray telescope on SRG”. In: *Astronomy & Astrophysics* 647, A1, A1. DOI: 10.1051/0004-6361/202039313. arXiv: 2010.03477 [astro-ph.HE].
- Remus, Rhea-Silvia, Andreas Burkert, Klaus Dolag, Peter H. Johansson, Thorsten Naab, Ludwig Oser, and Jens Thomas (Apr. 2013). “The Dark Halo—Spheroid Conspiracy and the Origin of Elliptical Galaxies”. In: *The Astrophysical Journal* 766.2, 71, p. 71. DOI: 10.1088/0004-637X/766/2/71. arXiv: 1211.3420 [astro-ph.GA].
- Remus, Rhea-Silvia, Klaus Dolag, Thorsten Naab, Andreas Burkert, Michaela Hirschmann, Tadzium L. Hoffmann, and Peter H. Johansson (Jan. 2017). “The co-evolution of total density profiles and central dark matter fractions in simulated early-type galaxies”. In: *Monthly Notices of the Royal Astronomical Society* 464.3, pp. 3742–3756. DOI: 10.1093/mnras/stw2594. arXiv: 1603.01619 [astro-ph.GA].

- Reynolds, S. P. (Sept. 2008). “Supernova remnants at high energy.” In: *Annual Review of Astronomy & Astrophysics* 46, pp. 89–126. DOI: 10.1146/annurev.astro.46.060407.145237.
- Sazonov, S. and I. Khabibullin (June 2017). “The intrinsic collective X-ray spectrum of luminous high-mass X-ray binaries”. In: *Monthly Notices of the Royal Astronomical Society* 468.2, pp. 2249–2255. DOI: 10.1093/mnras/stx626. arXiv: 1703.03354 [astro-ph.HE].
- Schmidt, Maarten (Mar. 1959). “The Rate of Star Formation.” In: *The Astrophysical Journal* 129, p. 243. DOI: 10.1086/146614.
- Schulze, Felix, Rhea-Silvia Remus, Klaus Dolag, Sabine Bellstedt, Andreas Burkert, and Duncan A. Forbes (Apr. 2020). “Kinematics of simulated galaxies II: Probing the stellar kinematics of galaxies out to large radii”. In: *Monthly Notices of the Royal Astronomical Society* 493.3, pp. 3778–3799. DOI: 10.1093/mnras/staa511. arXiv: 2001.02237 [astro-ph.GA].
- Schulze, Felix, Rhea-Silvia Remus, Klaus Dolag, Andreas Burkert, Eric Emsellem, and Glenn van de Ven (Nov. 2018). “Kinematics of simulated galaxies - I. Connecting dynamical and morphological properties of early-type galaxies at different redshifts”. In: *Monthly Notices of the Royal Astronomical Society* 480.4, pp. 4636–4658. DOI: 10.1093/mnras/sty2090. arXiv: 1802.01583 [astro-ph.GA].
- Shakura, N. I. and R. A. Sunyaev (June 1973). “Reprint of 1973A&A....24..337S. Black holes in binary systems. Observational appearance.” In: *Astronomy & Astrophysics* 500, pp. 33–51.
- Shtykovskiy, P. and M. Gilfanov (Sept. 2005). “High-mass X-ray binaries in the Small Magellanic Cloud: the luminosity function”. In: *Monthly Notices of the Royal Astronomical Society* 362.3, pp. 879–890. DOI: 10.1111/j.1365-2966.2005.09320.x. arXiv: astro-ph/0503477 [astro-ph].
- Shtykovskiy, P. E. and M. R. Gilfanov (July 2007). “High-mass X-ray binaries and recent star formation history of the Small Magellanic Cloud”. In: *Astronomy Letters* 33.7, pp. 437–454. DOI: 10.1134/S106377370707002X. arXiv: 0710.3059 [astro-ph].
- Smith, Randall K., Nancy S. Brickhouse, Duane A. Liedahl, and John C. Raymond (Aug. 2001). “Collisional Plasma Models with APEC/APED: Emission-Line Diagnostics of Hydrogen-like and Helium-like Ions”. In: *The Astrophysical Journal, Letters* 556.2, pp. L91–L95. DOI: 10.1086/322992. arXiv: astro-ph/0106478 [astro-ph].
- Springel, Volker (Dec. 2005). “The cosmological simulation code GADGET-2”. In: *Monthly Notices of the Royal Astronomical Society* 364.4, pp. 1105–1134. DOI: 10.1111/j.1365-2966.2005.09655.x. arXiv: astro-ph/0505010 [astro-ph].
- Springel, Volker, Tiziana Di Matteo, and Lars Hernquist (Aug. 2005). “Modelling feedback from stars and black holes in galaxy mergers”. In: *Monthly Notices of the Royal Astronomical Society* 361.3, pp. 776–794. DOI: 10.1111/j.1365-2966.2005.09238.x. arXiv: astro-ph/0411108 [astro-ph].
- Springel, Volker and Lars Hernquist (Feb. 2003). “Cosmological smoothed particle hydrodynamics simulations: a hybrid multiphase model for star formation”. In: *Monthly Notices of the Royal Astronomical Society* 339.2, pp. 289–311. DOI: 10.1046/j.1365-8711.2003.06206.x. arXiv: astro-ph/0206393 [astro-ph].
- Steinborn, Lisa K., Klaus Dolag, Julia M. Comerford, Michaela Hirschmann, Rhea-Silvia Remus, and Adelheid F. Teklu (May 2016). “Origin and properties of dual and offset active galactic nuclei in a cosmological simulation at  $z=2$ ”. In: *Monthly Notices of the Royal Astronomical Society* 458.1, pp. 1013–1028. DOI: 10.1093/mnras/stw316. arXiv: 1510.08465 [astro-ph.GA].
- Steinborn, Lisa K., Klaus Dolag, Michaela Hirschmann, M. Almudena Prieto, and Rhea-Silvia Remus (Apr. 2015). “A refined sub-grid model for black hole accretion and AGN feedback

- in large cosmological simulations”. In: *Monthly Notices of the Royal Astronomical Society* 448.2, pp. 1504–1525. DOI: 10.1093/mnras/stv072. arXiv: 1409.3221 [astro-ph.GA].
- Steiner, Andrew W., James M. Lattimer, and Edward F. Brown (Oct. 2010). “The Equation of State from Observed Masses and Radii of Neutron Stars”. In: *The Astrophysical Journal* 722.1, pp. 33–54. DOI: 10.1088/0004-637X/722/1/33. arXiv: 1005.0811 [astro-ph.HE].
- Swartz, Douglas A., Kajal K. Ghosh, Allyn F. Tennant, and Kinwah Wu (Oct. 2004). “The Ultraluminous X-Ray Source Population from the Chandra Archive of Galaxies”. In: *The Astrophysical Journal, Supplement* 154.2, pp. 519–539. DOI: 10.1086/422842. arXiv: astro-ph/0405498 [astro-ph].
- Tanaka, Y. (1997). “X-ray spectrum of low-mass X-ray binaries”. In: *Accretion Disks - New Aspects*. Ed. by Emmi Meyer-Hofmeister and Henk Spruit. Vol. 487, p. 1. DOI: 10.1007/BFb0105817.
- Tauris, Thomas M., Edward P. J. van den Heuvel, and Gerrit J. Savonije (Feb. 2000). “Formation of Millisecond Pulsars with Heavy White Dwarf Companions: Extreme Mass Transfer on Subthermal Timescales”. In: *The Astrophysical Journal, Letters* 530.2, pp. L93–L96. DOI: 10.1086/312496. arXiv: astro-ph/0001013 [astro-ph].
- Teklu, Adelheid F., Rhea-Silvia Remus, Klaus Dolag, Alexander M. Beck, Andreas Burkert, Andreas S. Schmidt, Felix Schulze, and Lisa K. Steinborn (Oct. 2015). “Connecting Angular Momentum and Galactic Dynamics: The Complex Interplay between Spin, Mass, and Morphology”. In: *The Astrophysical Journal* 812.1, 29, p. 29. DOI: 10.1088/0004-637X/812/1/29. arXiv: 1503.03501 [astro-ph.GA].
- Teklu, Adelheid Franziska (2018). “A Dress Code for Galaxies: How the Interplay of Gas, Stars, Dark Matter and Environment Shapes Their Appearance in Simulations”. PhD thesis. Ludwig-Maximilians-Universität, München.
- Tornatore, L., S. Borgani, K. Dolag, and F. Matteucci (Dec. 2007). “Chemical enrichment of galaxy clusters from hydrodynamical simulations”. In: *Monthly Notices of the Royal Astronomical Society* 382.3, pp. 1050–1072. DOI: 10.1111/j.1365-2966.2007.12070.x. arXiv: 0705.1921 [astro-ph].
- Tornatore, L., S. Borgani, F. Matteucci, S. Recchi, and P. Tozzi (Mar. 2004). “Simulating the metal enrichment of the intracluster medium”. In: *Monthly Notices of the Royal Astronomical Society* 349.1, pp. L19–L24. DOI: 10.1111/j.1365-2966.2004.07689.x. arXiv: astro-ph/0401576 [astro-ph].
- Torres, G., J. Andersen, and A. Giménez (Feb. 2010). “Accurate masses and radii of normal stars: modern results and applications”. In: *Astronomy & Astrophysics, Reviews* 18.1-2, pp. 67–126. DOI: 10.1007/s00159-009-0025-1. arXiv: 0908.2624 [astro-ph.SR].
- Ueda, Yoshihiro, Masayuki Akiyama, Günther Hasinger, Takamitsu Miyaji, and Michael G. Watson (May 2014). “Toward the Standard Population Synthesis Model of the X-Ray Background: Evolution of X-Ray Luminosity and Absorption Functions of Active Galactic Nuclei Including Compton-thick Populations”. In: *The Astrophysical Journal* 786.2, 104, p. 104. DOI: 10.1088/0004-637X/786/2/104. arXiv: 1402.1836 [astro-ph.CO].
- Verbunt, F. (2015). *Lecture Notes on Compact Binaries*. URL: <https://www.astro.ru.nl/~fverbunt/binaries/> (visited on 02/23/2021).
- Weisskopf, Martin C., Harvey D. Tananbaum, Leon P. Van Speybroeck, and Stephen L. O’Dell (July 2000). “Chandra X-ray Observatory (CXO): overview”. In: *X-Ray Optics, Instruments, and Missions III*. Ed. by Joachim E. Truemper and Bernd Aschenbach. Vol. 4012. Society of Photo-Optical Instrumentation Engineers (SPIE) Conference Series, pp. 2–16. DOI: 10.1117/12.391545. arXiv: astro-ph/0004127 [astro-ph].
- White, N. E., L. Stella, and A. N. Parmar (Jan. 1988). “The X-Ray Spectral Properties of Accretion Disks in X-Ray Binaries”. In: *The Astrophysical Journal* 324, p. 363. DOI: 10.1086/165901.

- White, Simon D. M., Ulrich G. Briel, and J. P. Henry (Mar. 1993). “X-ray archeology in the Coma cluster.” In: *Monthly Notices of the Royal Astronomical Society* 261, pp. L8–L12. DOI: 10.1093/mnras/261.1.L8.
- Wiersma, Robert P. C., Joop Schaye, and Britton D. Smith (Feb. 2009). “The effect of photoionization on the cooling rates of enriched, astrophysical plasmas”. In: *Monthly Notices of the Royal Astronomical Society* 393.1, pp. 99–107. DOI: 10.1111/j.1365-2966.2008.14191.x. arXiv: 0807.3748 [astro-ph].
- Wik, D. R., B. D. Lehmer, A. E. Hornschemeier, M. Yukita, A. Ptak, A. Zezas, V. Antoniou, M. K. Argo, K. Bechtol, S. Boggs, F. Christensen, W. Craig, C. Hailey, F. Harrison, R. Krivonos, T. J. Maccarone, D. Stern, T. Venters, and W. W. Zhang (Dec. 2014). “Spatially Resolving a Starburst Galaxy at Hard X-Ray Energies: NuSTAR, Chandra, and VLBA Observations of NGC 253”. In: *The Astrophysical Journal* 797.2, 79, p. 79. DOI: 10.1088/0004-637X/797/2/79. arXiv: 1411.1089 [astro-ph.HE].
- Wilkins, D. R. and L. C. Gallo (Mar. 2015). “The Comptonization of accretion disc X-ray emission: consequences for X-ray reflection and the geometry of AGN coronae”. In: *Monthly Notices of the Royal Astronomical Society* 448.1, pp. 703–712. DOI: 10.1093/mnras/stu2524. arXiv: 1412.0015 [astro-ph.HE].
- Zdziarski, A. A., W. N. Johnson, and P. Magdziarz (Nov. 1996). “Broad-band  $\gamma$ -ray and X-ray spectra of NGC 4151 and their implications for physical processes and geometry.” In: *Monthly Notices of the Royal Astronomical Society* 283.1, pp. 193–206. DOI: 10.1093/mnras/283.1.193. arXiv: astro-ph/9607015 [astro-ph].
- Zdziarski, Andrzej A., Marta A. Dzielak, Barbara De Marco, Michal Szanecki, and Andrzej Niedzwiecki (Jan. 2021). “Accretion Geometry in the Hard State of the Black-Hole X-Ray Binary MAXI J1820+070”. In: *arXiv e-prints*, arXiv:2101.04482, arXiv:2101.04482. arXiv: 2101.04482 [astro-ph.HE].
- Zdziarski, Andrzej A., Juri Poutanen, William S. Paciesas, and Linqing Wen (Oct. 2002). “Understanding the Long-Term Spectral Variability of Cygnus X-1 with Burst and Transient Source Experiment and All-Sky Monitor Observations”. In: *The Astrophysical Journal* 578.1, pp. 357–373. DOI: 10.1086/342402. arXiv: astro-ph/0204135 [astro-ph].
- Zhang, Z., M. Gilfanov, and Á. Bogdán (Oct. 2012). “Dependence of the low-mass X-ray binary population on stellar age”. In: *Astronomy & Astrophysics* 546, A36, A36. DOI: 10.1051/0004-6361/201219015. arXiv: 1202.2331 [astro-ph.HE].
- Zhang, Z., M. Gilfanov, and Á. Bogdán (Aug. 2013). “Low-mass X-ray binary populations in galaxy outskirts: Globular clusters and supernova kicks”. In: *Astronomy & Astrophysics* 556, A9, A9. DOI: 10.1051/0004-6361/201220685. arXiv: 1211.0399 [astro-ph.HE].
- Zhang, Z., M. Gilfanov, R. Voss, G. R. Sivakoff, R. P. Kraft, N. J. Brassington, A. Kundu, A. Jordán, and C. Sarazin (Sept. 2011). “Luminosity functions of LMXBs in different stellar environments”. In: *Astronomy & Astrophysics* 533, A33, A33. DOI: 10.1051/0004-6361/201116936. arXiv: 1103.4486 [astro-ph.HE].

# List of Figures

1.1	Schematic illustration of typical HMXB and LMXB orbital configurations. The HMXB case depicts the more spherically symmetric accretion of wind material of the donor. The LMXB case shows the RLO of an evolved MS low mass star. Graphic directly taken from Lewin and van der Klis (2006). . . . .	4
1.2	Cross section of equatorial plane of equipotential surfaces in binaries. The thick curve enclosing the binaries through L1 represents the Roche-Lobe. Graphic directly taken from Lewin and van der Klis (2006). . . . .	7
1.3	Evolutionary steps of a typical Be binary system developing into a HMXB source. Individual steps will be outlined in the text. Note, that the timestamps presented here are assumed from a MLR of $L \propto M^{3.5}$ . Graphic directly taken from Lewin and van der Klis (2006). . . . .	9
1.4	Evolutionary steps of a typical low mass binary system developing into a LMXB source. Note, that the timestamps presented here are assumed from a MLR of $L \propto M^{3.5}$ . Individual steps will be outlined in the text. Graphic directly taken from Lewin and van der Klis (2006). . . . .	10
1.5	Graphics directly taken from Mineo et al. (2012a). <b>(a)</b> : Observed XLFs of HMXB in nearby spiral galaxies normalized w.r.t. SFR in different colors. In black, the cumulative version of the XLF model from equation (1.8) is shown. The y-axis gives the number of HMXBs which have a luminosity $L$ above $L_X$ . <b>(b)</b> : Shown here is the XLF normalization $A$ for HMXBs w.r.t. the SFR in a given galaxy. Red dots are different galaxies with error bars, the solid line is the best fit linear relation, the dashed line is the best fit relation of the form $A = \xi \times \text{SFR}^\beta$ , where $\beta = 0.73 \pm 0.05$ . We assume a linear relation for the XLF normalization in this thesis. . . . .	11
1.6	Graphic <b>(a)</b> directly taken from Zhang, Gilfanov, and Bogdán (2012) and <b>(b)</b> from Gilfanov (2004). <b>(a)</b> : Correlation between LMXB XLF normalization $f_{XLF}$ and age of the elliptical host galaxy. Stellar ages were determined from previous works. Numbers refer to the name of the galaxy in question. Red circles indicate galaxies with globular cluster specific frequency $S_N > 2.0$ . <b>(b)</b> : Shows relation between number of LMXBs and stellar mass of a host galaxy. Red circles are elliptical, blue triangles are spiral galaxies. Empty symbols indicate galaxies observed with smaller annuli. . . . .	12

- 1.7 Broadband spectrum of *Cyg X1* for different pointed observations. Hard-state: *Ginga*/OSSE June 6 1991 (*black*); *BeppoSAX* May 3-4 1998 (*blue*) and Sep 12 1996 (*cyan*). Soft and intermediate states: *BeppoSAX* June 22 1996 together with *CGRO*/OSSE and COMPTEL June 14-22 1996 (*red*); *ASCA*/*RXTE* May 30-21 1996 (*magenta*); *RTXE* May 23 1996 (*green*). Solid curves are best-fit Comptonization models. *Yellow*: Average hard state at 0.75-5 MeV from *CGRO*/COMPTEL. Graphic directly taken from Zdziarski, Poutanen, et al. (2002). . . . . 13
- 1.8 Accretion geometry around *Maxi J1820+070* derived from X-ray observations. The disk is truncated at  $R_{\text{in}}$ , and covered by a Comptonizing coronal plasma,  $C_s$ , from  $R_{\text{in}}$  to  $R_{\text{tr}}$ . Interior to  $R_{\text{in}}$ , there is a hot accretion flow with a relatively large scale height,  $C_h$ . Comptonization in  $C_s$  and  $C_h$  gives rise to the observed softer and harder, respectively, incident spectral components. The emission of  $C_h$  is reflected from the flared disk beyond  $R_{\text{tr}}$ , marked as  $R_h$ . The emission of the coronal plasma,  $C_s$ , is reflected from the disk beneath it, marked as  $R_s$ . Graphic and description directly taken from Zdziarski, Dzielak, et al. (2021). . . . . 17
- 1.9 Transitions of the accretion flow in XRB systems causing different spectral states. The ultra-soft state coincides with a stable thin disk configuration. The thermally dominant state shows the black body spectrum of the increasing temperature of the AD caused by high mass accretion. The very high state shows signs in both soft and very hard X-rays and is associated with the state shortly before the breakdown of the inner accretion flow leading to large comptonizing regions. When the inner accretion flow breaks down we reach the low/hard state dominated by hard X-ray emission from the diffuse comptonizing region in the central flow. The hard state is usually accompanied by radio emission from a developing jet outflow. . . . . 17
- 2.1 Illustration of the different cosmological volumes within the *Magneticum* set of simulations. Indicated are box sizes, number of particles (dark matter + gas) 22
- 2.2 *eROSITA* mock observation of a galaxy cluster at redshift  $z = 0.1$  illustrating the effects of AGN contamination. . . . . 28
- 2.3 Flow chart illustrating the main units of PHOX. The dashed box stands for the possibility to use external software designed to simulate observations of a certain X-ray telescope in conjunction with the output of PHOX unit 2. Graphic directly taken from Biffi, Dolag, Böhringer, et al. (2012). . . . . 29
- 3.1 Illustration of the luminosity sampling of the cumulative XLFs derived from equations (1.8) and (1.9). The left panel shows the two analytic solutions for HMXBs (*solid black*) and LMXBs (*dashed black*). The coloured lines are the reconstructed XLFs by directly counting the number of XRBs above a certain luminosity from an initial sample of  $N_{0,L} = 279$  LMXBs (*orange*) and  $N_{0,H} = 48$  HMXBs (*blue*).  $L_{\text{min}}$  was set to  $10^{36} \text{erg s}^{-1}$ . The two right panels show the corresponding pseudo CDFs (*solid black*) following eq. (3.2). The red crosses indicate the position of a single drawn sample point  $(p_i, L_i)$  from eq. (3.3) with respect to the CDF. . . . . 33

- 3.2 Age distribution of stellar particles for the 500 most massive halos in *Box4* of *Magneticum*. The dashed vertical lines at 5, 100 and 1000 Myr mark the age boundaries used to determine the eligibility of a stellar element to host a XRB component. The reds histogram shows the distribution of rejected stellar ages. The blue histograms shows the distribution of elements fulfilling the age conditions  $5 \text{ Myr} < t_H < 100 \text{ Myr}$  and  $t_L > 1 \text{ Gyr}$ .  $N_{\text{str}}$  is the number of stellar elements per age bin. The green histogram shows the formation efficiency  $\eta_{\text{HMXB}}(t)$  of HMXBs from Shtykovskiy and Gilfanov (2007). Number fractions are given in table 3.1. . . . . 37
- 4.1 Reconstructed cumulative Luminosity Functions (*magenta*) using **Set 1**. The dashed black line indicates the analytic model for HMXBs (left panel) and LMXBs (right panel) using parameters from table 1.2, respectively. The LFs were normalized by SFR in the HMXB case and stellar mass in the LMXB case, both quantities derived from halo properties. The blue shaded area is a density map constructed from 10000 analytic XLF variants, from randomly assigning parameters with uncertainties given in table 1.2. From darker to lighter shades, contour levels were chosen to contain 68%, 90% and 95% of variants. . . . . 42
- 4.2 Mass relation of the total X-ray luminosity of a galaxy, originating only from LMXB emission. The total luminosity is calculated by summation of the 0.5 – 8 keV luminosity of each LMXB with  $L > 5 \cdot 10^{37} \text{ erg s}^{-1}$  in the galaxy. Depicted here, is **Set 1** (*red*) together with a sample of 2000 simulated XRB populations (*green*). The black line is the expected theoretical relation based on Zhang, Gilfanov, and Bogdán (2012). The shaded area (*grey*) is the  $1\text{-}\sigma$  error of the solid black line. . . . . 42
- 4.3 SFR relation of the total X-ray luminosity of a galaxy originating only from HMXB emission. The total luminosity is calculated by summation of the 0.5 – 8 keV luminosity of each LMXB with  $L > 10^{36} \text{ erg s}^{-1}$  in the galaxy. Depicted here, is **Set 1** (*blue*) together with a sample of 2000 simulated galaxies (*green*). The simulated galaxies were created by randomly drawing SFRs for the normalisation of the HMXB XLF. The black line is the expected theoretical relation based on Mineo et al. (2012a). The shaded area (*grey*) is the  $1\text{-}\sigma$  error of the solid black line. The dash-dotted line is the . . . . . 44
- 4.4 Projected XRB emission of a poster-child LTG of our galaxy sample. It is shown face-on and has FSUB-ID 13633, a SFR of  $8.34 M_{\odot} \text{ yr}^{-1}$  and stellar mass  $2.73 \cdot 10^{11} M_{\odot}$ . Coordinates are in physical units. Photon energies are in the range 0.1 – 50keV. Red shades correspond to LMXB emission, blue shades to HMXB. Darker shades correspond to a higher photon count. The contour levels were chosen arbitrarily for illustrative purposes. . . . . 45
- 4.5 Star-formation map of galaxy FID-13633 in units of  $M_{\odot} \text{ yr}^{-1}$ . Overlaid is the projected XRB emission of HMXB (*green*) and LMXB (*red*). The contour levels correspond to photon counts of 15, 70, 140 and 300 from light to dark. Some of the white pixels seen in the outskirts are artifacts of the smoothing. Distances are in physical units. Photon energies are in the range 0.1 – 50keV. Image created with *pynbody* v1.0.2 [Pontzen et al. (2013)]. . . . . 46

- 4.6 Gas surface-density map of galaxy FID-13633. Overlaid is the projected XRB emission of HMXB (*green*) and LMXB (*red*). The contour levels correspond to photon counts of 15, 70, 140 and 300 from light to dark. Distances are in physical units. Photon energies are in the range 0.1 – 50keV. Image created with `pynbody v1.0.2` [Pontzen et al. (2013)]. . . . . 47
- 4.7 Stellar age map of galaxy FID-13633 given as the scale factor. Darker colors correspond to older regions. Overlaid is the projected XRB emission of HMXB (*green*) and LMXB (*red*). The contour levels correspond to photon counts of 15, 70, 140 and 300 from light to dark. Distances are in physical units. Photon energies are in the range 0.1 – 50keV. Image created with `pynbody v1.0.2` [Pontzen et al. (2013)]. . . . . 47
- 4.8 Photon counts of LMXB component as a function of HMXB photon counts for all galaxies in **Set 1** with reduced  $\mathcal{D}_A$ . The dashed black line is the 1:1 ratio. Colors are halo SFRs of the galaxies derived from simulation data. Left pointing arrows aligned at the vertical line  $\log c_{HXB} = 0.9$  indicate galaxies with no HMXB photons and SFR = 0. . . . . 48
- 4.9 Fraction of galaxies in **Set 2** as a function of the count ratio  $r$  between XRB and GAS emission. Colors correspond to different emission bands in both panels. The lower panel shows the cumulative version of the top panel histogram. Galaxies with no photons coming from the gas component were placed into the highest ratio bin. . . . . 48
- 4.10 Same as in figure 4.9 but for the AGN component. . . . . 49
- 4.11 *Top panel:* Cumulative average photon counts per energy bin of 135 LTGs (*black*). Prior to taking the average photon count per energy bin, each spectrum was normalized by the total photon count, which is the sum of each of the constituents (GAS: *blue*, AGN: *red*, XRB: *green*). This gives equal weight to each contributing galaxy. *Lower panel:* Relative contribution of the individual components to the total spectrum, with the XRB contribution being solid for highlighting. . . . . 50
- 4.12 Same as figure 4.11, but for the 173 ETGs in our sample. . . . . 50
- 4.13 SFR –  $M_*$  relation of **Set 2** colour coded by the emission ratio  $c_{XB}/c_G$  between the XRB and gas component in the energy range 0.1 – 50 keV. The dashed lines indicate the mass and SFR cuts used for the property binning in figure 4.14 and 4.15. Galaxies with zero star-formation were placed at  $\log(\text{SFR}) = -4$ . 51
- 4.14 Cumulative average photon counts per energy bin, split by stellar mass, in the upper panels of each quadrant. Prior to taking the average photon count per energy bin, each spectrum was normalized by the total photon count, which is the sum of each of the constituents (GAS: *blue*, AGN: *red*, XRB: *green*). This gives equal weight to each contributing galaxy. Lower panels in each quadrant show the relative contribution of each component to the total spectrum. Mass splits were chosen such that each mass bin is roughly equal sized (indicated by  $N_g$ ). The grey boxes indicate the limits of the chosen mass bin. . . . . 53

4.15	Cumulative average photon counts per energy bin, split by SFR, in the upper panels of each quadrant. Prior to taking the average photon count per energy bin, each spectrum was normalized by the total photon count, which is the sum of each of the constituents (GAS: <i>blue</i> , AGN: <i>red</i> , XRB: <i>green</i> ). This gives equal weight to each contributing galaxy. Lower panels in each quadrant show the relative contribution of each component to the total spectrum. SFR splits were chosen such that each SFR bin is roughly equal sized (indicated by $N_g$ ). The grey boxes indicate the limits of the chosen SFR bin. . . . .	54
4.16	Virial temperature distribution for each of the SFR splits from figure 4.15 indicated by different colors. The distributions have been normalized by the number of galaxies in each SFR bin, in order to see differences in the width of the distribution. Notice the $\log - \log$ scale of the image. The symbols indicate the temperature bin centers and serve as a viewing aid. . . . .	55
4.17	Full view of the $5 \text{ deg}^2$ lightcone produced from <i>Magneticum</i> , <i>Box2</i> with photon energy range of $0.1 - 50 \text{ keV}$ using gas, AGN and XRB emission. The color-bar indicates photon counts in each pixel. One pixel corresponds to $0.00244 \text{ deg}^2$ . . . . .	55
4.18	Spectrum of the full lightcone view (figure 4.17) in the energy range $0.3 - 10 \text{ keV}$ . Included are the power-laws of Cappelluti et al. (2017) for the uCXB ( <i>cyan</i> ) and the nsCXB ( <i>magenta</i> ) with their $1-\sigma$ uncertainty (shaded area) in the top panel. The lower panel shows the relative contribution of each component to the total spectrum. Included in the lower panel is also the absolute deviation of the power law models from the total spectrum normalized to the error of the power law model. By error we specifically mean the absolute difference between the upper and lower $1-\sigma$ bounds. . . . .	56
4.19	Same as in figure 4.17. The black patches in the field of view correspond to masked halos of a specific mass. In this case, all photons within the virial radius $R_{vir}$ of a halo with virial mass $M_{vir} > 2 \cdot 10^{13} M_{\odot}$ were removed from each redshift slice of the lightcone. . . . .	57
4.20	Spectrum of the masked lightcone view (figure 4.19) in the energy range $0.3 - 10 \text{ keV}$ . Included are the power-laws of Cappelluti et al. (2017) for the uCXB ( <i>cyan</i> ) and the nsCXB ( <i>magenta</i> ) with their $1-\sigma$ uncertainty (shaded area) in the top panel. The lower panel shows the relative contribution of each component to the total spectrum. Included in the lower panel is also the absolute deviation of the power law models from the total spectrum normalized to the error of the power law model. By error we specifically mean the absolute difference between the upper and lower $1-\sigma$ bounds. . . . .	58
4.21	Relative contribution of gas (top panel), AGN (middle panel) and XRB emission to each redshift slice of the lightcone for the energy range $0.3 - 10 \text{ keV}$ . The redshift of each slice is given by the colour gradient. . . . .	59
A.1	Spectral composition of galaxy <i>F-13</i> . . . . .	85
A.2	Similar to figure 4.13 with color bar depicting XRB emission strength. We see a diagonal color gradient which is expected from the scaling relations. . . . .	85
A.3	Virial temperature distribution for each of the stellar mass splits from figure 4.14 indicated by different colors. . . . .	86
A.4	Similar to figure 4.5 for sSFR bins. . . . .	86
A.5	Zoomed image of a portion of the lightcone in $0.1-50 \text{ keV}$ band. . . . .	87

A.6	Same as figure 4.20 but as photon flux per bin normalized by bin width. . . .	87
-----	---	----

# List of Tables

1.1	Empirical mass-radius and mass-luminosity relations from stars in binary systems. <sup>1</sup> : Values adopted from table 11.3 in Lewin, van Paradijs, and van den Heuvel (1995) which uses data from Andersen (1991). No uncertainties given. <sup>2</sup> : Best-fit power law slope derived from data in table 2 of Torres et al. (2010). <sup>3</sup> : Best-fit power law slope derived from data in table 2 of Eker et al. (2015) .	5
1.2	Parameter values for XLFs of equations (1.8) and (1.9) given by the work of Mineo et al. (2012a) for HMXBs ( <i>right</i> ) and Zhang, Gilfanov, and Bogdán (2012) for LMXBs ( <i>left</i> ). The uncertainty of $\xi$ is given as 0.28 dex. Luminosities are given in units of $10^{36}$ erg s <sup>-1</sup> . $K_1$ has the unit $10^{-11} M_{\odot}^{-1}$ . $\gamma$ and $\alpha$ are dimensionless power-law slopes of the respective XLFs. . . . .	13
2.1	Sizes, resolutions, particle numbers $N_{\text{part}}$ , particle mass for dark matter $m_{\text{DM}}$ and gas $m_{\text{gas}}$ as well as softening lengths $\epsilon$ for dark matter/gas and stars for each of the <i>Magneticum Pathfinder</i> boxes. Table recreated from table 1.1 in Teklu (2018). . . . .	21
3.1	Number fractions of eligible and ineligible XRB elements based on figure 3.2.	37



# Abbreviations

AD	Accretion Disk
AGN	Active Galactic Nucleus
ARF	Ancillary Response File
BH	Black Hole
CE	Common Envelope
CMB	Cosmic Microwave Background
CO	Compact Object
CV	Cataclysmic Variable
CXB	Cosmic X-ray Background
EH	Event Horizon
ETG	Early Type Galaxy
GC	Globular Cluster
HMXB, HXRB, HXB	High-mass X-ray binary
ICM	Intra-Cluster Medium
IMF	Initial Mass Function
IMXB	Intermediate-mass X-ray binary
ISM	Interstellar Medium
LF	Luminosity Function
LMXB, LXR, LXB	Low-mass X-ray Binary
LTG	Late Type Galaxy
MLR	Mass-Luminosity Relation
MRI	Magneto-Rotational Instability
MRR	Mass-Radius Relation
MS	Main Sequence
NS	Neutron Star
QPO	Quasi Periodic Oscillation
RE	Resolution Element
RLO	Roche-Lobe Overflow
RMF	Redistribution Matrix File
SED	Spectral Energy Distribution
SFH	Star Formation History
SFR	Star Formation Rate
SMBH	Super Massive Black Hole
SPH	Smoothed Particle Hydrodynamics
SPMHD	Smoothed Particle Magneto-Hydrodynamics
SSP	Single Stellar Population
ULX	Ultra Luminous X-ray source
WD	White Dwarf
XR	X-ray Binary
XL	X-ray Luminosity Function
ZAMS	Zero-Age Main-Sequence



# Appendix A

## Additional Figures

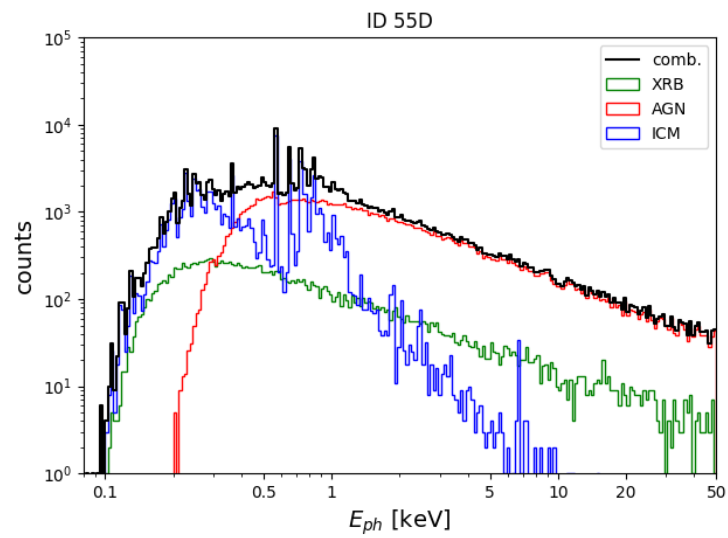


Figure A.1: Spectral composition of galaxy *F-13*.

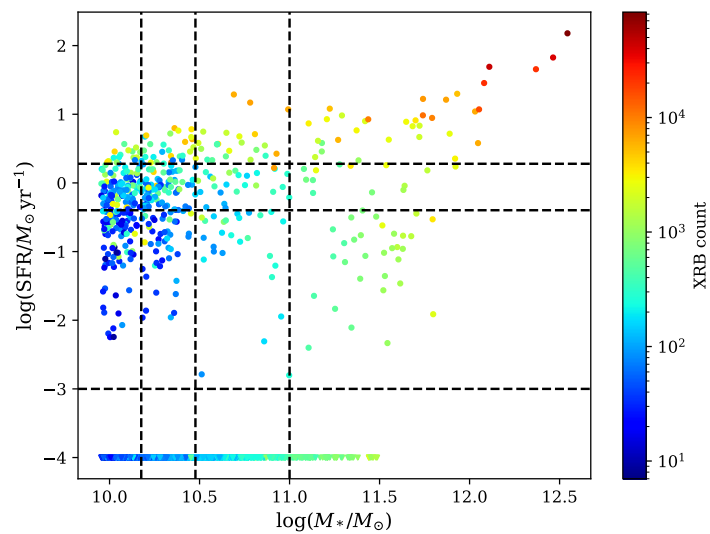
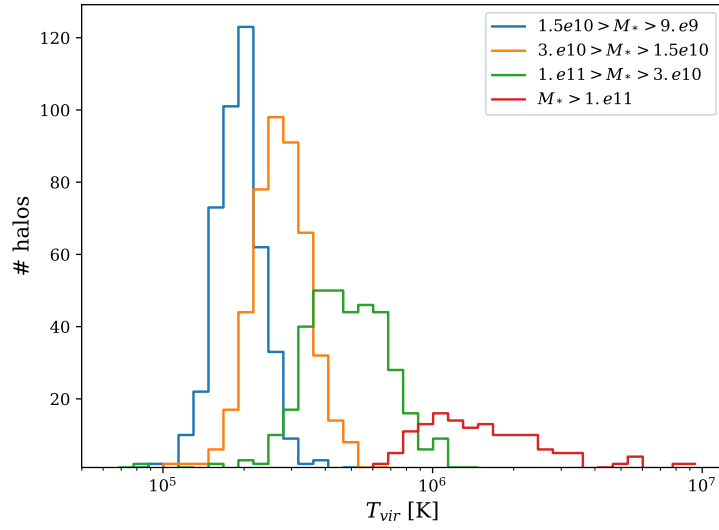
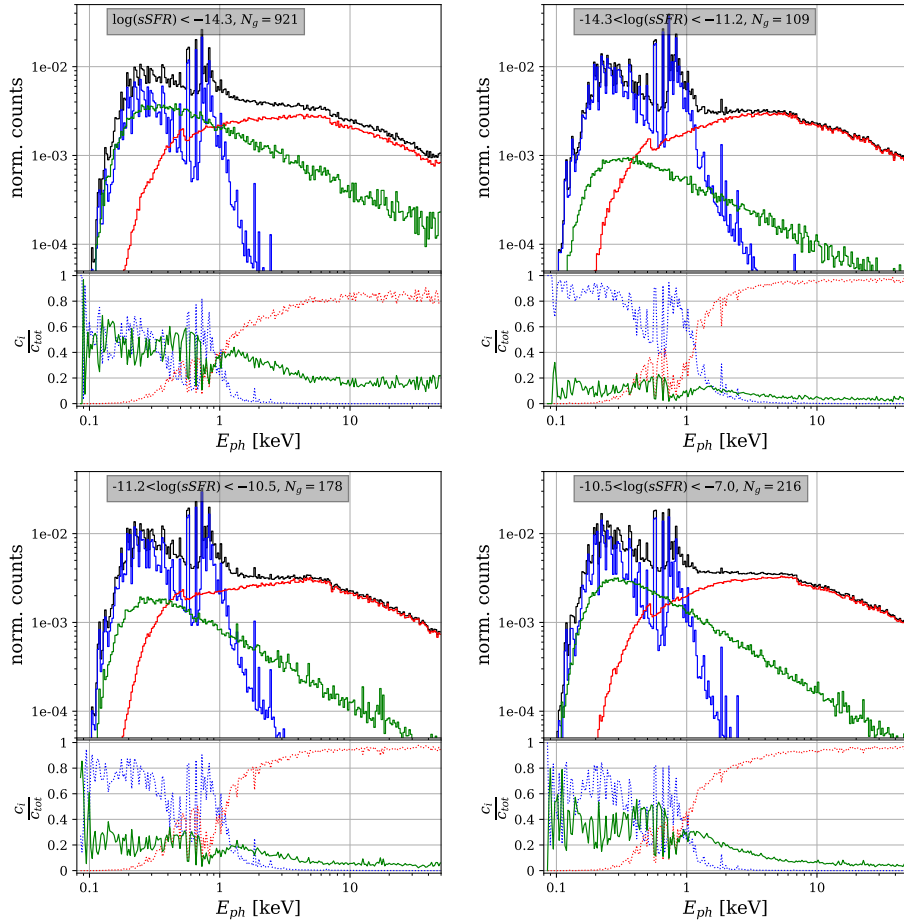


Figure A.2: Similar to figure 4.13 with color bar depicting XRB emission strength. We see a diagonal color gradient which is expected from the scaling relations.



**Figure A.3:** Virial temperature distribution for each of the stellar mass splits from figure 4.14 indicated by different colors.



**Figure A.4:** Similar to figure 4.5 for sSFR bins.

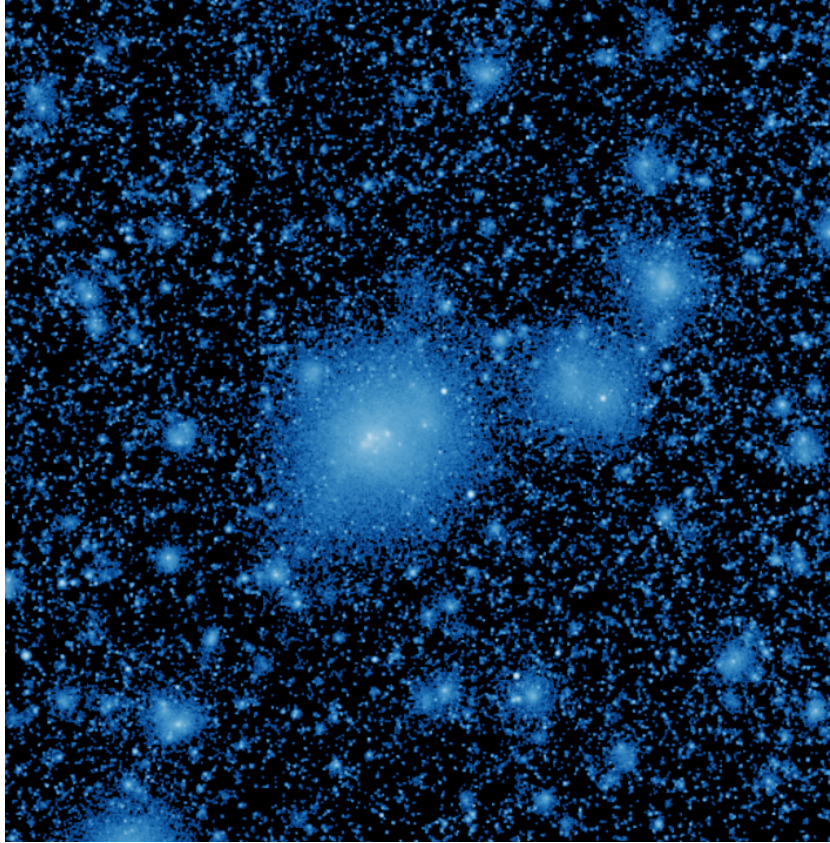


**Figure A.5:** Zoomed image of a portion of the lightcone in 0.1-50 keV band.

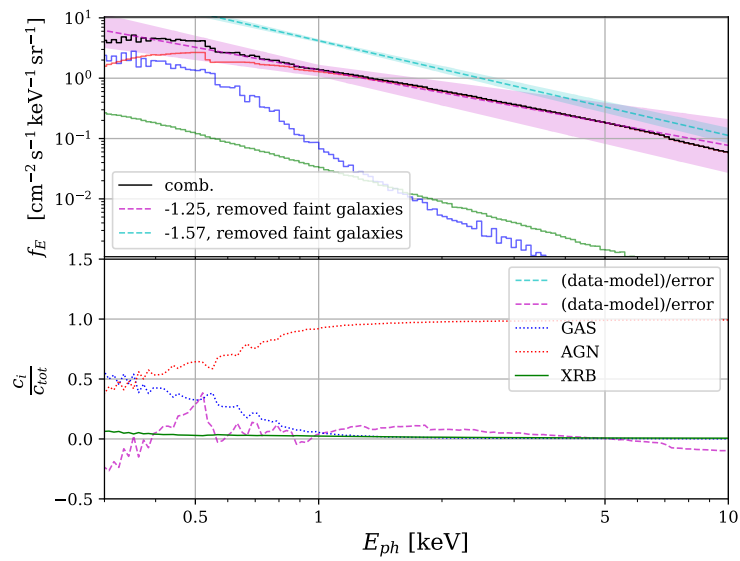


**Figure A.6:** Same as figure 4.20 but as photon flux per bin normalized by bin width.



# Appendix B

## Acknowledgement

At this point, I want to express my sincerest gratitude and thankfulness towards my supervisors, PD Dr. Klaus Dolag and Dr. Veronica Biffi, for providing me with excellent and sincere advice and encouragement during our discussions, for always listening to my concerns when I had doubts, as well as for being available should problems arise, even in the very unusual times, during which this thesis was created.

I am also deeply thankful to be given the opportunity to continue a scientific career in this wonderful group and I am looking forward to what the next years and projects may have in store.

I also wanted to thank the entire CAST group for being an awesome and welcoming group with amazing people, who make working here a real pleasure, with extensive scientific as well as casual discussions on all kinds of subjects.

Ich möchte außerdem meinen Freunden danken, denen ich endlich "exakte" und "völlig aussagekräftige" Vorhersagen für ihre Zukunft geben kann, bedingt durch die relative Position von, hauptsächlich, Mars zu anderen, zufällig ausgewählten Himmelskörpern.

Mein größter Dank geht an meine Familie, die mich immer unterstützt und mir in all meinen Lebensabschnitten immer Rückhalt, Fürsorge und Liebe gegeben hat.



# Selbständigkeitserklärung

Ich versichere hiermit, die vorliegende Arbeit mit dem Titel

**Contribution from Stellar Binaries to the X-ray Emission of Simulated Galaxies**

selbständig verfasst zu haben und keine anderen als die angegebenen Quellen und Hilfsmittel verwendet zu haben.

Stephan Vladutescu-Zopp

München, den 15. April 2021